

**Late Ordovician Glaciation:
Modelling Experiments of a Paradox**


By

Pascale Francine Poussart
B.Sc., McGill University, 1996


A Thesis Submitted in Partial Fulfilment of the
Requirements for the Degree of

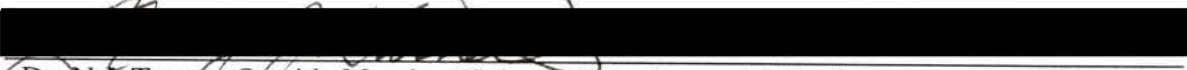
MASTER OF SCIENCE
In the School of Earth and Ocean Sciences


We accept this thesis as conforming
To the required standard


Dr. A.J. Weaver, Supervisor (School of Earth and Ocean Sciences)


Dr. C.R. Barnes, Co-Supervisor (School of Earth and Ocean Sciences)


Dr. A. Fanning, Departmental Member (School of Earth and Ocean Sciences)


Dr. N.J. Turner, Outside Member (School of Environmental Studies)


Dr. G.K.C. Clarke, External Examiner (Department of Earth and Ocean Sciences,
University of British Columbia)

© Pascale Poussart, 1998

University of Victoria

All rights reserved. This thesis may not be reproduced in whole or in
part, by photocopy or other means, without the permission of the author.

Supervisor: Dr. Andrew J. Weaver

ABSTRACT

The analysis of the geological, chemical and paleontological records of the Ordovician System has unearthed an apparent paradox, which consists of the occurrence of the Late Ordovician glaciation centred on the South Pole, simultaneous with high atmospheric CO₂ concentrations (10 to 18x pil). The purpose of this thesis is to investigate this paradox through a series of modelling sensitivity experiments and to combine results with analytical data provided by the geological record.


Results from the modelling experiments show that it is possible to maintain a significant permanent snow cover in the southern high latitudes of Gondwana ($14.5 \times 10^6 \text{km}^2$) given 10x CO₂ concentrations, WFCS forcing, -4.5% solar luminosity, a length of day of 21.5 hours and an albedo jump of 0.3. In addition, the CSO experiment with 10x CO₂, a decreased solar luminosity and shortened length of day and an albedo jump of 0.1 also sustained a permanent snow cover ($0.54 \times 10^6 \text{km}^2$), although less extensive than for the WFCS experiment with the higher albedo. Summer temperatures may be a more critical parameter for glacial inception than the supply of moisture. Model results showed that whereas high latitude winter temperatures were always cold enough to ensure precipitation to fall as snow, summer temperatures were in some instances, such as for the HSO, warm enough so as to prevent the development of a permanent snow cover. Results from all sensitivity experiments consistently reveal the presence of a permanent sea ice cover extending from the North Pole to 60°-70°N. The presence of this extensive sea ice cover appears to have played a critical role in the dramatic cooling of the globally averaged ocean temperature (~2.4°C).

The global-mean SAT increased by ~2.74°C and ocean temperature by ~0.35°C between the 10x and 18x experiments. The coupled model reveals a strong sensitivity to changes in the albedo jump. The global-mean SAT and ocean temperature cooled by ~5.9°C and ~0.8°C respectively between the aj01 and aj03 experiments. Concurrent to a


weakening of the thermohaline circulation is a decrease in the Southern Hemisphere heat transport with an increase in the albedo jump. A marked increase in the intensity of the seasonal cycle is apparent in the HSO experiment relative to the CSO experiment, as one would expect from the influence of the higher obliquity. The annual average precipitation rates produced in the present study show a small increase at polar latitudes for the HSO relative to the CSO configuration. However, during the winter months where precipitation mostly falls as snow, high latitude precipitation is largest in the CSO scenario.

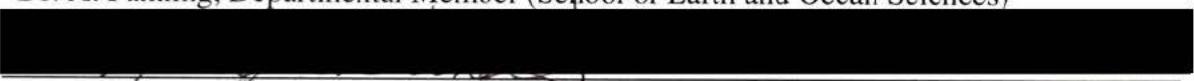
The geographic configuration of the Late Ordovician resulted in a ~42% increase in the global ocean poleward heat transport in the Southern Hemisphere relative to present-day modelling experiments, a latitudinal redistribution of the ocean heat transport and a significant asymmetry relative to the equator. These findings outline the need to include ocean heat transport values derived from OGCM experiments in future modelling studies, which rely on prescribed heat transports. The coupled model was able to produce a permanent snow cover on Gondwana, which included 60% of all the glacial deposits found on the supercontinent. Hence, within the context of the coupled model, no paradox exists.

Examiners:


Dr. A.J. Weaver, Supervisor (School of Earth and Ocean Sciences)


Dr. C.R. Barnes, Co-Supervisor (School of Earth and Ocean Sciences)


Dr. A. Fanning, Departmental Member (School of Earth and Ocean Sciences)


Dr. N.J. Turner, Outside Member (School of Environmental Studies)



Dr. G.K.C. Clarke, External Examiner (Department of Earth and Ocean Sciences, University of British Columbia)

Table of Contents

| | |
|--|-------------|
| ABSTRACT | ii |
| Table of Contents | iv |
| List of Tables | vii |
| List of Figures | viii |
| Acknowledgements | x |
| 1. Late Ordovician glaciation | 1 |
| 1.1 INTRODUCTION..... | 1 |
| 1.2 PALEOGEOGRAPHIC SETTING OF THE ORDOVICIAN PERIOD..... | 3 |
| 1.3 GEOLOGICAL EVIDENCE FOR GLACIATION..... | 7 |
| 1.3.1 <i>Glacial deposits</i> | 7 |
| 1.3.2 <i>Evaporites</i> | 9 |
| 1.3.3 <i>Carbonates</i> | 10 |
| 1.3.4 <i>Oolitic ironstones</i> | 10 |
| 1.4 LATE ORDOVICIAN MASS EXTINCTION..... | 11 |
| 1.4.1 <i>Modes of extinction</i> | 11 |
| 1.4.2 <i>Initial phase of extinctions</i> | 12 |
| 1.4.3 <i>Final phase of extinctions</i> | 14 |
| 1.4.4 <i>Patterns of recovery</i> | 15 |
| 1.4.5 <i>Causes of extinction: Links to glaciation</i> | 16 |
| 1.4.5.1 <i>Sea level changes</i> | 16 |
| 1.4.5.2 <i>Paleoceanographic changes</i> | 17 |
| 1.4.5.3 <i>Climatic changes</i> | 19 |
| 1.4.5.4 <i>Changes in continental distribution</i> | 19 |
| 1.4.5.5 <i>Asteroid impact hypothesis</i> | 20 |
| 1.5 CHRONOLOGY..... | 21 |
| 1.6 TIMING..... | 22 |
| 1.6.1 <i>Evidence from glacio-marine deposits</i> | 23 |
| 1.6.2 <i>Evidence from geochemical isotopic excursions</i> | 23 |
| 1.6.2.1 <i>Oxygen isotopic data</i> | 23 |
| 1.6.2.2 <i>Carbon isotopic data</i> | 25 |
| 1.6.2.3 <i>Strontium isotopic data</i> | 26 |

| | |
|--|-----------|
| 1.6.3 Evidence from eustatic sea level changes..... | 27 |
| 1.6.4 Cautionary notes..... | 29 |
| 1.7 EXTENT..... | 29 |
| 1.8 REVIEWING THE PARADOX: GLACIATION VS. HIGH ATMOSPHERIC CO ₂ | 30 |
| 1.8.1 Evidence for high atmospheric CO ₂ levels..... | 30 |
| 1.8.2 Previous climate modelling experiments..... | 32 |
| 1.8.2.1 A geography problem..... | 32 |
| 1.8.2.2 The faint sun theory..... | 33 |
| 2. Methodology..... | 35 |
| 2.1 MODEL DESCRIPTION..... | 35 |
| 2.1.1 Ocean model..... | 35 |
| 2.1.2 Atmosphere model..... | 38 |
| 2.1.2.1 Thermodynamic components..... | 39 |
| 2.1.2.2 Hydrological components..... | 41 |
| 2.1.3 Ice model..... | 44 |
| 2.2 BOUNDARY AND INITIAL CONDITIONS..... | 48 |
| 2.2.1 Land-sea distribution..... | 49 |
| 2.2.2 Earth's rotation rate..... | 50 |
| 2.2.3 Orbital parameters..... | 51 |
| 2.2.4 Atmospheric CO ₂ | 57 |
| 2.2.5 Solar luminosity..... | 57 |
| 2.2.6 Topography..... | 57 |
| 2.2.7 Wind fields..... | 58 |
| 2.2.8 Changes in albedo..... | 59 |
| 2.2.9 Initial conditions..... | 60 |
| 3. Late Ordovician modelling results..... | 61 |
| 3.1 MODEL SENSITIVITY TO ATMOSPHERIC CO ₂ | 61 |
| 3.1.1 Temperature response..... | 62 |
| 3.1.2 Hydrological response..... | 68 |
| 3.1.3 Meridional overturning response..... | 70 |
| 3.1.4 Glacial response..... | 72 |
| 3.2 MODEL SENSITIVITY TO ALBEDO JUMP..... | 73 |
| 3.2.1 Temperature response..... | 73 |

| | | |
|-----------|--|------------|
| 3.2.2 | <i>Meridional overturning response</i> | 75 |
| 3.2.3 | <i>Glacial response</i> | 76 |
| 3.3 | MODEL SENSITIVITY TO ORBITAL PARAMETERS..... | 78 |
| 3.3.1 | <i>Temperature response</i> | 79 |
| 3.3.2 | <i>Meridional overturning response</i> | 81 |
| 3.3.3 | <i>Glacial response</i> | 83 |
| 4. | Discussion of results | 85 |
| 4.1 | PALEOCEANOGRAPHY OF THE ORDOVICIAN..... | 85 |
| 4.1.1 | <i>Wind-driven circulation</i> | 85 |
| 4.1.2 | <i>Thermohaline circulation</i> | 88 |
| 4.1.3 | <i>Global heat transport patterns</i> | 90 |
| 4.2 | POTENTIAL FOR GLACIATION..... | 95 |
| 4.2.1 | <i>Role of atmospheric CO₂ forcing</i> | 95 |
| 4.2.2 | <i>Role of the change in albedo jump</i> | 97 |
| 4.2.3 | <i>Role of orbital parameters</i> | 99 |
| 4.2.3.1 | <i>HSO vs. CSO</i> | 99 |
| 4.2.3.2 | <i>WFCS vs. CFWS</i> | 101 |
| 4.2.4 | <i>Northern Hemisphere glaciation</i> | 104 |
| 4.2.5 | <i>Comparison of glacial response with other modelling experiments</i> | 105 |
| 4.2.6 | <i>Glacial chronology</i> | 105 |
| 4.3 | FUTURE STUDIES..... | 108 |
| 4.3.1 | <i>Effects of changes in cloud cover</i> | 108 |
| 4.3.2 | <i>Effects of extensive equatorial epicontinental seas</i> | 109 |
| 4.3.3 | <i>Effects of oceanic gateways</i> | 109 |
| 5. | Conclusions | 110 |
| | References | 115 |
| | Appendix A | 130 |
| | GLOSSARY..... | 130 |

List of Tables

| | |
|--|-----|
| Table 1.1 Ordovician time scale | 2 |
| Table 2.1 Atmospheric model parameters | 44 |
| Table 2.2 Ice model parameters | 48 |
| Table 2.3 Boundary and initial conditions for modelling experiments..... | 49 |
| Table 2.4 Orbital parameters used in modelling experiments | 53 |
| Table 3.1 Climate sensitivity parameters..... | 64 |
| Table 3.2 Late Ordovician modelling results | 65 |
| Table 4.1 Climatic indicators for glacial inception on South Pole..... | 104 |

List of Figures

| | |
|--|----|
| Figure 1.1 Late Ordovician (Ashgill) reconstruction (~440 Ma) | 3 |
| Figure 1.2 Paleogeography of Gondwana regions during Hirnantian glaciation | 8 |
| Figure 1.3 The $\delta^{18}\text{O}$ trend across the Ordovician/Silurian transition | 25 |
| Figure 1.4 RCO_2 levels as a function of time according to GEOCARB II modelling experiments | 32 |
| Figure 2.1 Land-sea distribution for Late Ordovician modelling experiments | 50 |
| Figure 2.2 a) Sketch of the orbital configurations used in the modelling experiments | 55 |
| Figure 2.2 b) Daily average solar insolation incident on a unit horizontal surface at the top of the atmosphere as a function of latitude and time of year | 56 |
| Figure 2.3 Annually averaged wind stress field for 10x CO_2 experiments | 59 |
| Figure 2.4 Latitudinal profile of the coalbedo for an albedo jump of 0.1 , 0.2 and 0.3 | 60 |
| Figure 3.1 Annual mean surface air temperature difference (18x – 10x CO_2) | 62 |
| Figure 3.2 Latitude vs. time distribution of the difference in zonal mean surface air temperature between the 18x and 10x experiments | 63 |
| Figure 3.3 Modelled January and July SST and SAT for 10x experiment | 66 |
| Figure 3.4 Modelled January and July SST and SAT for 18x experiment | 67 |
| Figure 3.5 Modelled hydrological response to CO_2 | 69 |
| Figure 3.6 Modelled overturning response to CO_2 | 71 |
| Figure 3.7 Latitude vs. time distribution of the difference in zonal mean surface air temperature response to changes in albedo jump..... | 73 |
| Figure 3.8 Modelled sea surface temperature response to changes in albedo jump | 74 |
| Figure 3.9 Modelled overturning streamfunction and heat transport response to changes in albedo jump | 76 |
| Figure 3.10 January averaged snow thicknesses for albedo jumps of 0.1, 0.2 and 0.3 | 77 |
| Figure 3.11 Annually averaged ice concentration for albedo jumps of 0.1, 0.2 and 0.3 | 78 |
| Figure 3.12 Annually averaged solar insolation difference at the top of the atmosphere between the HSO and CSO | 79 |
| Figure 3.13 Annual mean surface air temperature for HSO and CSO experiments..... | 80 |

| | |
|---|-----|
| Figure 3.14 Latitude vs. time distribution of the difference in zonal mean surface air temperature between the HSO and CSO experiments | 81 |
| Figure 3.15 Modelled overturning response to changes in orbital forcing..... | 82 |
| Figure 3.16 Annual mean ice concentration for CSO and HSO experiments..... | 84 |
| Figure 4.1 Annual mean surface velocities obtained from Ordovician control experiment. ... | 86 |
| Figure 4.2 Equatorial vertical velocities in Ordovician control experiment at 50 m..... | 87 |
| Figure 4.3 Global planetary heat transport with ocean and atmosphere components..... | 91 |
| Figure 4.4 Global ocean poleward heat transport | 92 |
| Figure 4.5 Global poleward heat transport comparison between present-day run and Ordovician control run | 93 |
| Figure 4.6 Annual spatially averaged temperature over the South Pole (70°-90°S), as a function of time of year for CO ₂ sensitivity experiments..... | 96 |
| Figure 4.7 Annual spatially averaged temperature over the South Pole (70°-90°S), as a function of time of year for albedo jump sensitivity experiments | 98 |
| Figure 4.8 Annual spatially averaged temperature over the South Pole (70°-90°S), as a function of time of year for CSO and HSO sensitivity experiments .. | 101 |
| Figure 4.9 Annual spatially averaged temperature over the South Pole (70°-90°S), as a function of time of year for CFWS and WFCS sensitivity experiments | 103 |
| Figure 4.10 Variations of the obliquity, eccentricity, longitude of the perihelion and precession parameter over the past 1 m.y. | 107 |

Acknowledgements

I wish to thank Thomas Crowley and Steven Baum for providing the land-sea mask and Mark Gibbs for the wind fields used in the experiments. I am grateful to them as well as Michael Eby for discussions and suggestions linked to this work. This research was supported by an FCAR Fellowship awarded to Pascale Poussart and by NSERC, CSHD, AES/CICS and Steacie operating grants, as well as an IBM SUR grant awarded to Dr. Andrew Weaver. All numerical computations were conducted locally on a suite of IBM RS6000s including two SP2s. Infrastructure support from the University of Victoria is gratefully acknowledged.

Finally, I wish to thank Nicole and Denis Poussart for their great support and inspiration.

1. Late Ordovician glaciation

1.1 Introduction

The Late Ordovician continental glaciation at ~440 million years ago (Ma), centred on the north African portion of Gondwana, is now a well-documented event by the work of *Beuf et al.* [1971], *Hambrey and Harland* [1981] and others. It is the third most important glacial period in the Phanerozoic (last 545 million years or m.y.) after the late Paleozoic and the late Cenozoic glaciations and was the first major glacial event to affect the Paleozoic biotas. It is of particular interest because its timing and duration are still debated. In fact, its glacial maximum was pronounced (Hirnantian Stage, 0.5 - 1 m.y.) [*Sheehan and Coorough*, 1990; *Barnes*, 1992] while the age of its glacial deposits spans probably 35 m.y. (Table 1.1). This stands in contrast with glacial patterns of the late Paleozoic which extend over 65 m.y. [*Frakes et al.*, 1992]. The Late Ordovician glaciation also coincided with the second greatest mass extinction event in all of the Phanerozoic, after that of the Permo-Triassic [*Sepkoski*, 1995a].

Analysis of the geological, chemical and paleontological records of the Ordovician System has given rise to an apparent paradox, which stems from the occurrence of the Late Ordovician glaciation simultaneous with high atmospheric CO₂ concentrations. Geochemical modelling experiments suggest that Late Ordovician atmospheric CO₂ levels were 8 to 20 times (x) greater than pre-industrial levels i.e. prior to 1850 (p_{il} = 280 ppm) [*Berner*, 1994]. The purpose of this thesis is to investigate this paradox through a series of modelling sensitivity experiments and to combine results with analytical data provided by the paleontological and geological record. Particular emphasis is given on questioning the ocean's role in influencing the Late Ordovician climate.

Table 1.1 Ordovician time scale. Adapted from *Harland et al.* [1989].

| <i>Period</i> | <i>Epoch</i> | <i>Age</i> | <i>Ma</i> |
|-------------------|--------------|---------------|-----------|
| <i>Silurian</i> | Llandovery | Rhuddanian | 439 |
| <i>Ordovician</i> | Ashgill | Hirnantian | 443 |
| | | Rawtheyan | |
| | | Cautleyan | |
| | | Pusgillian | |
| | Caradoc | Onnian | |
| | | Actonian | |
| | | Marshbrookian | |
| | | Longvillian | |
| | | Soudleyan | |
| | | Harnagian | |
| | | Costonian | 464 |
| | Llandeilo | Late | 469 |
| | | Middle | |
| | | Early | |
| | Llanvirn | Late | |
| | | Early | |
| | Arenig | Late | |
| Early | | | |
| Tremadoc | | | |
| <i>Cambrian</i> | | Dolgellian | |

1.2 Paleogeographic setting of the Ordovician Period

The Ordovician represents one of the oldest time periods for which accurate plate tectonic reconstruction can be produced (Figure 1.1). The reconstruction of the Ordovician paleogeography (510 - 439 Ma) requires the fusion of data derived from several fields of geology. Paleomagnetism is the primary source of information for continental positioning. While paleomagnetic data provides quantitative evidence for both paleolatitude and north-south orientation of paleocontinents [Bambach *et al.*, 1980], it cannot be used for the determination of paleolongitude. Hence, the complementary analysis of paleobiogeographic, paleoclimatic and tectonic data allows for the compilation of a detailed reconstruction.

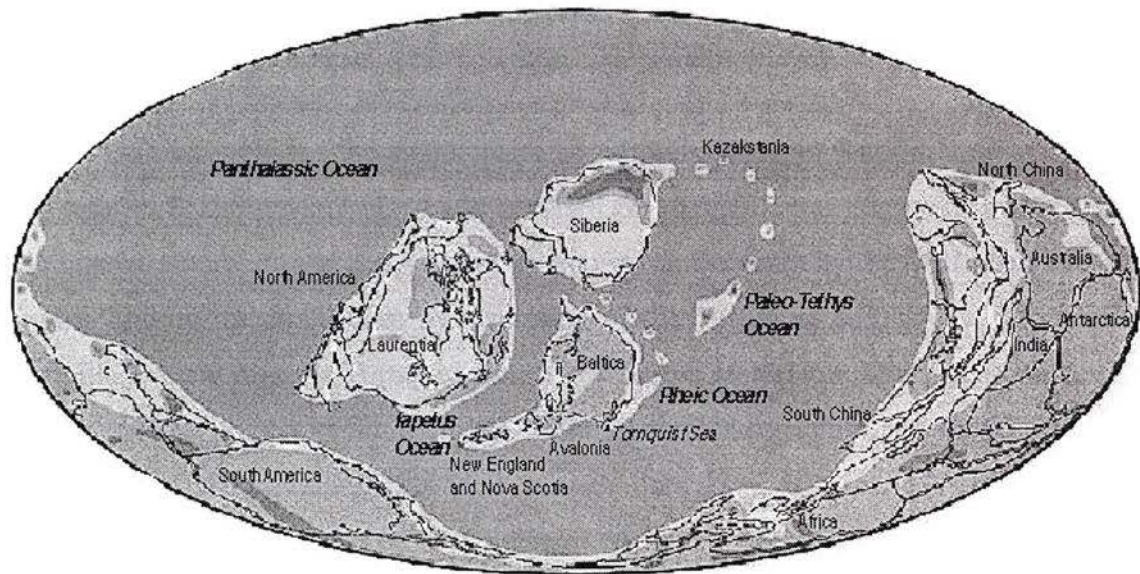


Figure 1.1 Late Ordovician (Ashgill) reconstruction (~440 Ma) (Scotese, 1998, personal communication). Black contours: modern landmass; dark grey: ancient landmass; light grey: epicontinental seas.

During the Ordovician, the major paleocontinents were Gondwana, Baltica, Avalonia, Laurentia and Siberia/Kazakhstania [Scotese *et al.*, 1979; Ziegler *et al.*, 1979;

Bambach et al., 1980; *Smith et al.*, 1981; *Scotese and McKerrow*, 1990; *Scotese and McKerrow*, 1991; *Scotese*, 1997]. The supercontinent Gondwana consisted mostly of regions known today as Yucatan, Florida and Piedmont of southeastern USA, South America, Africa, south-central Europe (which included Iberia, France, parts of West Germany and the Bohemian massif) [*Young*, 1990], Turkey, Central Iran and Afghanistan, Greater India, Antarctica, New Zealand, North China (Sino-Korea) and South China (the Yangtze platform), Qiangtang and Lhasa, Indochina, Burma-Malaya and Australia. Although the geographical position of the major continental plates forming Gondwana is fairly well constrained, the locations of numerous small continental blocks that bordered Gondwana are less unequivocal [*Scotese and McKerrow*, 1990]. West Gondwana shows evidence of a southward movement during the Ordovician and crossed the South Pole in the Caradoc. Glacial deposits of Ashgill age suggest that an ice cap covered the whole of North Africa from Morocco to Arabia [*Scotese and McKerrow*, 1990].

Baltica included the major parts of northern Europe: Russia west of the Ural Mountains, Scandinavia, Poland and northern Germany. It was confined on the west by the Iapetus suture, on the east by the Ural suture, on the south by the Variscan/Hercynian suture, and on the south-west by the suture of the Törnquist Sea, which closed in the Ashgill, and laid near the Törnquist Line [*Scotese and McKerrow*, 1990]. The distribution of modern-day reefs is generally restricted to the tropics and subtropics (within 30° north and south of the equator), in waters warmer than 21°C [*Frakes*, 1979]. Hence, the presence of reefs and warm water carbonates on Baltica during the end of the Ordovician suggests that the continent had slowly moved northward, into equatorial latitudes [*Webby*, 1984].

During the Early Ordovician (late Tremadoc), the Avalonian Island Arc (Ardennes of Belgium and northern France, England, Wales, southeastern Ireland, the Avalon Peninsula of eastern Newfoundland, parts of coastal New Brunswick, Nova Scotia and coastal New England) rifted away from northwestern Gondwana [*Scotese and McKerrow*, 1990; *Mac Niocaill et al.*, 1997]. This is supported by the presence of Cambrian and Early Ordovician shallow water faunas similar to those of western

Gondwana. By the Middle Ordovician, the shallower benthic faunas of eastern Avalonia began to lose their affinities with Gondwana and, by the late Caradoc, these faunas gained similarities with Baltic faunas [Cocks and Fortey, 1990]. This suggests that the Törnquist Sea, which separated these two continents, had by that time sufficiently narrowed to allow cratonic benthos to travel across it (less than 1000 km wide) [Fortey and Cocks, 1986]. The faunal connection between Avalonia and Baltica occurred significantly earlier than the Hirnantian Stage, when the analogous faunas became identical across the Iapetus Ocean, between Laurentia and Baltica [Cocks and Fortey, 1990]. Avalonia probably collided with Baltica in the early Ashgill, with the final closure of the Törnquist Sea [Scotese and McKerrow, 1990]. The positioning of the southwest portion of Avalonia appears less certain. Tillites belonging to the Boston Bay Group have not yet been dated but could potentially be of late Ashgill age. In this case, a relocation of Avalonia to higher latitudes would be indicated [Scotese and McKerrow, 1990].

Laurentia was composed of modern North America (except for parts of its marginal orogenic belts), northwest Ireland, the North Slope of Alaska, Greenland, Scotland and the Chukotsk Peninsula of former northeastern U.S.S.R. During the Early Ordovician, carbonates were abundant on the cratons of Laurentia, Siberia and the Indo-Australian region of Gondwana whereas clastic rocks were dominant on Baltica and the North African margin of Gondwana. The equatorial location of Laurentia during the Ordovician is further supported by evidence from climatically correlated deep-water faunas [Scotese and McKerrow, 1990].

Siberia was a separate continent. It included Mongolia, as well as land east of the Urals to the Verkhoyanski Mountains. Its southern margin crossed Asia north of present Kazakhstan and was bounded by the South Mongolian arc. Its orientation was 180° from its present alignment and it occupied the Northern Hemisphere arid belt [Boucot *et al.*, 1995]. Kazakhstania was a triangular shaped continent centred on what is now Kazakhstan. Until recently, it was believed that Kazakhstania was a separate and independently moving continent [Scotese *et al.*, 1979]. However, recent evidence has showed that it rather consisted of an amalgamation of volcanic arcs and far-travelled

terrane that extended eastward from the Siberian plate [*Scotese and McKerrow, 1991*]. Its southwestern margin extended down between the Urals and southwestern Siberia and its northeastern margin extended up between the Altai and the Tien Shan Mountains. The Aral Sea area was then located on its eastern margin. Throughout the Cambrian to the Early Carboniferous, Siberia and Kazakhstan moved northwards [*Scotese and McKerrow, 1990*]. Evidence from Ordovician bauxite found in Kazakhstan suggests that the continent was located in the Northern Hemisphere, within tropical to subtropical latitudes [*Boucot et al., 1995*]. During the Caradoc, shallow, epicontinental seas covered most continents, especially in tropical regions [*Algeo and Wilkinson, 1991*] following the *gracilis* transgression. This sea level rise was the largest in the Phanerozoic relative to the cratonic area submerged [*Ross and Ross, 1992*].

During the Ordovician, three major ocean basins (Figure 1.1) separated the paleocontinents described above. The Panthalassic Ocean spanned the globe from pole to pole and was as wide at the equator as the present-day Pacific Ocean. While the majority of continents were residing in the Southern Hemisphere, Panthalassa had a unique configuration as it extended over most of the northern half of the globe.

The Paleo-Tethys Ocean separated the northern and western margins of Gondwana from the southern margin of Baltica and the southwestern margin of Siberia/Kazakhstan. Its southern margin was a site of major convergent plate boundary and widespread back-arc formation [*Scotese and McKerrow, 1991; Scotese, 1997*] while its northern margin was defined by Avalonia, Baltica and Kazakhstan.

The Iapetus Ocean originated during the latest Precambrian (600-545 Ma) with the rifting of the southern margin of Baltica from the eastern margin of Laurentia [*Bond et al., 1984*]. It expanded throughout the Cambrian and was widest during Late Cambrian/Early Ordovician time [*Mac Niocaill et al., 1997*]. Throughout the remainder of the Ordovician, subduction below eastern Laurentia led to the narrowing of the Iapetus and resulted in the eventual collision of the Avalonia-Baltica block with Laurentia during the Middle Devonian [*Cocks and Fortey, 1990; McKerrow and Scotese, 1990*]. *Mac Niocaill et al. [1997]* used paleomagnetic and faunal evidence to argue that

the final closure of the Iapetus occurred in the Silurian although strike-slip motion may have persisted well into the Devonian. Recent paleogeographic models [Dalziel *et al.*, 1994] have challenged this traditional reconstruction and have suggested a more dynamic evolution of the Iapetus Ocean. These models describe a complex series of Laurentia-Gondwana collisions throughout the Paleozoic. In addition, Dalziel *et al.* [1994] explained the Taconic Orogeny as a continent-continent collision between North and South America, coinciding with the Famatinian Orogeny. This explanation contrasts with the more traditional view that the orogeny was an arc-continent collision associated with the subduction of the Iapetus underneath Laurentia. However, Mac Niocaill *et al.* [1997] have argued that although both the traditional and alternative reconstructions appear plausible relative to the paleomagnetic evidence, the traditional view is preferred since it is also supported by faunal data.

A series of island arcs was present off the eastern margin of Laurentia during the Early Ordovician. Scotese and McKerrow [1990] argued that these arcs began colliding with the northeastern edge of Laurentia during the Early Ordovician. The final collision resulted in the Caradoc Taconian Orogeny in New England. Upon their creation, several of these arcs were located at a great distance from the coast of Laurentia [Scotese and McKerrow, 1990]. The presence of micro-continents in the middle of the Iapetus and their influence on the ocean circulation may have altered the climate on either regional or global scales.

1.3 Geological evidence for glaciation

1.3.1 Glacial deposits

Glacial evidence on the African continent has been found in West Africa (west and southwest in Morocco, Mauritania and Sierra Leone), South Africa and in several sites in and around the western Sahara (Algeria, Libya and Mali). The deposits represent complex continental, marine and lacustrine glacial environments as well as glacial erosional landforms of Ashgill age [Beuf *et al.*, 1971; Hambrey and Harland, 1981]

(Figure 1.2). In the central Sahara, the Tamadjert Formation of Ashgill age covers a broad band across northwestern Africa and includes subglacial valleys up to 40 km long and 300 m deep. A total of four distinct tillites and striated pavements displaying a generally northward flow have been identified [Frakes, 1979]. Glacial evidence from a thin tillite has also been found in the north central Arabian Peninsula [Young, 1981]. In Europe, several basins appear to have collected Upper Ordovician glacio-marine diamictites (northeastern Scotland, western Ireland, East Germany, Normandy, Spain and the Iberian Peninsula) [Brenchley *et al.*, 1991]. In eastern Canada, the distribution of Late Ordovician glacio-marine deposits is confined to Nova Scotia and eastern Newfoundland, whereas in the latter, tillites have also been recognised [Hambrey, 1985].

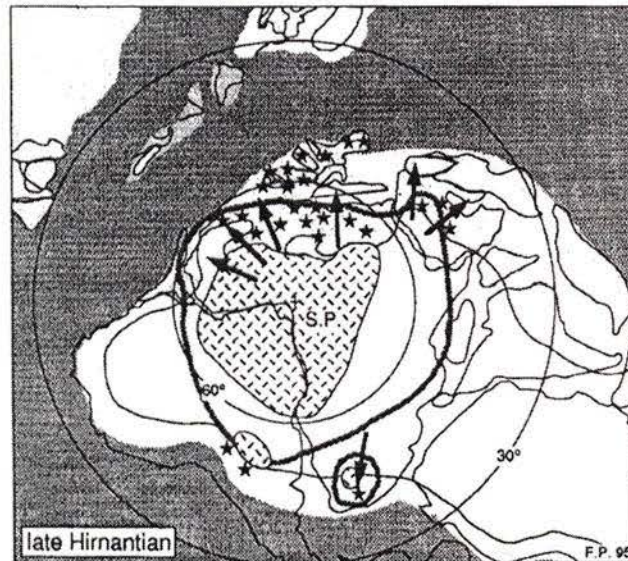


Figure 1.2 Paleogeography of Gondwana regions during Hirnantian glaciation. Largest extension of the south polar ice cap (heavy dotted line), direction of moving of the ice sheet (arrows), from Beuf *et al.* [1971] and Vaslet [1990] and glacio-marine diamictites occurrences (black stars). Heavy stippling: deep oceanic domain; light stippling: shelf and slope areas; white: emerged land; crossed hatching: ice cap. From Paris *et al.* [1995].

Relative to the timing of glaciation on other continents, the Early Paleozoic glaciation in South America appears to have been delayed until Early Silurian time. For example, the Iapo Formation in the Paraná Basin, southern Brazil is considered of glacial origin and may just be of Ordovician age. However, it post-dates 450 Ma and pre-dates Early Devonian strata so it is more likely of Silurian age [Caputo and Crowell, 1985].

The Cancaniri Formation of Bolivia, northern Argentina and southern Peru, also has deposits of glacial origin but these are unlikely of Ashgill age. The Vila Maria Formation at the base of the Paraná Basin, central Brazil contains diamictite beds interpreted as glacial in origin and of Silurian age [Caputo and Crowell, 1985].

1.3.2 Evaporites

Evaporites are sediments formed by the evaporation of salt water, usually seawater. The present-day distribution of evaporites is mostly confined to the subtropical belt of high evaporation-low precipitation. Based on the assumptions that ancient deposits were formed in similar environments and that few ancient evaporites have been completely dissolved, the spatial and temporal distributions of evaporites provide insights into the history of aridity on the globe [Frakes, 1979]. Estimating precipitation/evaporation patterns during the Ordovician is difficult if not impossible because the terrestrial realm was devoid of land plants and evaporites were sparsely distributed. However, Zharkov [1981] attempted to compile evaporite distribution and abundance curves for the Paleozoic. Cambrian rates of evaporites accumulation were moderate while rates increased abruptly in the mid-Devonian [Zharkov, 1981]. During Ordovician and Silurian times, the amount of evaporites was only about 2.1% by volume of total evaporites, whereas this time interval represents about 17% of Paleozoic time. Evaporite deposition peaked during the Ashgill (Late Ordovician) and coincided with glacial maxima and eustatically low sea level stands. This supports the idea that a cold Earth is a dry Earth [Frakes, 1979]. The eustatic regression which accompanied the glaciation would have generated restricted hypersaline areas in intracratonic basins [Hardie, 1996]. Ronov *et al.* [1984] plotted evaporite data on paleogeographic reconstructions and observed a distinct contraction of evaporites towards equatorial latitudes during the glacial interval, reaching a maximum between the late Caradoc to early Llandovery (20° contraction in Asia which included Siberia, Kazakhstania and China). Laurentia and Siberia were sites of pervasive evaporite deposition. In particular, Siberia had large intracratonic basins and an extensive west coast configuration, which were contributing to arid conditions.

1.3.3 Carbonates

Ronov [1980] compiled modes of carbonate distribution throughout the Phanerozoic. Results suggest that ~34% of the sediments deposited on the continents during the Ordovician were of carbonate origin and that the carbonate accumulation rate was low compared to that of the Cambrian and Devonian. The data available for determining global distribution patterns of carbonates is too coarse for estimating accumulation rates on the epoch timescale. However, the curves for the Ashgill-Llandovery interval do represent a minimum within the Early Paleozoic.

Deposition of carbonate sediments was restricted to latitudes equatorward of ~35° throughout most of the Ordovician and Silurian. One exception to this is found during the pre-Caradoc and the post-Wenlock, where evidence of carbonate deposition spreads to ~50°S on the Asian continents. Thus, data from the carbonate record, although sparse, reveal a latitudinally restricted distribution coincident with the glaciation.

1.3.4 Oolitic ironstones

Oolitic ironstones are small round or ovate accretionary bodies made up of concentric layers of iron carbonate. They commonly aggregate around a nucleus such as a shell fragment, an algal pellet or a quartz-sand grain in shallow, wave-agitated water. Until recently, the climatic factors believed necessary for the production of oolitic ironstones included a warm climate, deep weathering, dispersed continents and high stand of global sea level. *Van Houten* [1985] analysed the relative distribution of Ordovician and Jurassic oolitic ironstones and argued for the need of a revision of these climatic conditions. The latitudinal distribution of Ordovician ironstones is divided between two major belts: between 0° and ~25°S (Baltica, Laurentia and Siberia) and between ~45°S and 85°S (northwestern margin of assembled Gondwana and Armorica which included northwestern France, Brittany and Normandy). This distribution shows that most of the Ordovician ironstones were deposited during high stands of sea level, with an absence of land plants to foster chemical weathering, and in high southern latitudes that supported an ice cap by the Late Ordovician. Although there was a

significant drop during the Late Ordovician to the Early Silurian, high rates of ironstones production were reinstated during the Silurian [*Van Houten and Hong-Fei, 1990*]. Weathering due to high atmospheric CO₂ concentrations, as much as 10x present-day concentrations, may have acted as an alternative climatic control and explain the accumulation of ironstones in high latitudes [*Van Houten, 1985*].

1.4 Late Ordovician mass extinction

1.4.1 Modes of extinction

The Hirnantian Stage, which terminated the Ordovician Period, coincided with the second greatest mass extinction event in all of the Phanerozoic, after that of the Permian-Triassic (250 Ma) [*Raup and Sepkoski, 1982; Sepkoski, 1995a*]. This extinction had profound effects on benthic, pelagic and planktonic groups, including graptolites, conodonts, acritarchs and chitinozoa, and also greatly affected the reef community complex [*Brenchley and Cocks, 1982; Webby, 1984; Brenchley et al., 1995*]. However, the more cosmopolitan and commonly more eurytopic taxa remained mostly unaffected by this event, as is commonly the case in most extinctions [*Boucot, 1990*]. Throughout the Ashgill, familial and generic diversity of the trilobites and cystoids remained fairly stable while the conodonts, graptolites and possibly the brachiopods all indicate dramatic declines of diversity. The extinction did not severely affect the major groups at the level of order or above, but families, genera and species were badly affected. An estimated 26% of the families became extinct during the Late Ashgill bio-event and genera diversity declined by about 60% [*Sepkoski, 1981; Sepkoski, 1995a; Sepkoski, 1995b*].

This extinction event did not occur abruptly, at least with respect to brachiopods and trilobites [*Brenchley and Newall, 1980*]. In fact, it appears to have occurred in two main steps, with some possible minor ones between them, spanning several million years. Paleontological data shows declining diversity signatures between Middle Ordovician and Early Silurian times. For most benthic and pelagic Ordovician faunas, maximum generic diversity was achieved during the Caradoc and began to decrease in the early

Ashgill, possibly as a result of rapid plate movement and subsequent reduction in provincialism. For example, as Baltica and Avalonia travelled from high southern latitudes towards Laurentia, the brachiopods, trilobites and graptolites of these northward moving continents began to gain similar characteristics as those of Laurentia [Stanley, 1986]. Although this may suggest that these continents were converging at the time, the relative gain in similarities within the various faunas may be an artefact of the transition between high latitude to equatorial climate conditions.

1.4.2 Initial phase of extinctions

The initial phase of extinctions slightly lagged behind the onset of the regression at the Rawtheyan-Hirnantian boundary. This episode took place at the *pacificus-extraordinarius* zonal boundary. It is characterised by the sudden reduction in diversity of most groups [Brenchley, 1989], the terminal mass extinction of 3 graptolite families, 21 genera, and many species [Koren, 1991; Melchin and Mitchell, 1991], a severe reduction of cystoids, and a 40% loss of genera for trilobites [Owen *et al.*, 1991]. The *pacificus* event can most probably be linked to the Ashgill glacial maximum.

Assessment of the graptolite faunal changes simultaneous to the Late Ordovician glaciation is not straightforward because a significant sea level drop associated with the glaciation drained most of the cratonic platforms, creating hiatuses in the record. The carbonate sequence of Anticosti Island, Québec remains a unique site where continuous sedimentation was recorded [Barnes, 1988b]. The habitats in which the richest graptolite faunas are found consist of oxygen-poor, nitrogen-compound rich waters. Modern-day analogues to these habitats are found about the oxygen minimum zone in the eastern tropical Pacific, the Indian Ocean, the central California upwelling system and a small portion of the west African upwelling system [Berry and Wilde, 1990]. These locations are mostly confined within 0-30°N latitude and are characterised by warm waters.

Faunal changes among graptolites appear to be closely linked to sea level changes. Increases in sea level may have led to the transgression of oxygen-poor, nitrogen-compound rich waters over shelves and shelf margins whereas regressions,

which seem to coincide with graptolite extinction pulses, may have caused the draining of these habitats [Berry and Wilde, 1990]. Graptolites retained a steady evolutionary pace during the Ashgill. The late Caradoc-early Ashgill Biozone assemblages had a high diversity, with 15-20 species [Barnes, 1986]. Koren [1991] estimated that sometime during the Rawtheyan Stage, most likely during the *P. pacificus* Zone, a significant radiation event occurred and graptolites reached their maximum diversity.

The most important evolutionary crisis for graptolites, which translated into the terminal mass extinction of Ashgill families, genera and many species, occurred at the end of the *P. pacificus* Biozone or at the base of the *Climacograptus extraordinarius* Zone [Koren, 1991; Barnes et al., 1995]. The fauna was reduced to three or four species. Berry and Wilde [1990] argued that the rapid eustatic fall in sea level observed during the Hirnantian, enhanced the thermal gradients in surface waters of the Southern Hemisphere oceans. This could have triggered the creation of oxygen-laden deep waters adjacent to the ice sheet on the South Pole thereby preventing the creation of oxygen-poor, nitrogen-compound rich waters which graptolites appear to have preferred. The timing of this event seems to be simultaneous to the glacial maximum. Within the *Glyptograptus* (*G.*) *persculptus* Biozone, a modest radiation event took place as well as during the *acuminatus* Biozone [Koren, 1991]. Despite these radiation events, only half of the diversity levels prior to the *pacificus* event were reached by the end of the Hirnantian Stage [Barnes, 1986].

Brachiopods experienced only moderate decreases in both abundance and diversity during this first episode of extinction. Consequently, the shelly faunas of the Hirnantian were mostly composed of the residual brachiopods, commonly referred to the *Hirnantia* fauna [Rong and Harper, 1988]. This fauna has been the focus of considerable attention as it is used for determining the Ordovician-Silurian boundary in shelf facies. The *Hirnantia* faunas are typically represented by the following group of taxa: *Dalmanella*, *Hirnantia*, *Kinnella*, *Paromalomena*, *Eostropheodonta/Aphanomena*, *Cliftonia*, *Plectothyrella* and *Hindella* [Rong and Harper, 1988].

The majority of Hirnantian brachiopod faunas were characterised by cosmopolitan genera (commonly less than ten) and low diversity species [Owen *et al.*, 1991]. Species typical to *Hirnantia* fauna were ecologically eurytopic and may have been tolerant to both shallow and deep marine environments. The geographical distribution of the *Hirnantia* fauna was apparently constrained to subtropical and temperate regions, and followed a marked latitudinal provincialism. Its occurrence is best known in the Yangtze region of China, where it originated in the *mirus* Zone, spread rapidly and came to an abrupt extinction at the base of the *G. persculptus* Zone [Rong, 1984; Wang *et al.*, 1993b]. The *Hirnantia* fauna has also been recognised in the following areas: Europe, Kazakhstan, Siberia, China, Southeast Asia, North Africa, North and South America [Rong, 1984; Rong and Harper, 1988; Brenchley, 1989; Owen *et al.*, 1991; Owen and Robertson, 1995].

1.4.3 Final phase of extinctions

The second and final phase of extinctions coincided with the beginning of a rapid transgression at the end of the Hirnantian Stage. It is defined by an extinction of both benthic and pelagic faunas at the base of the graptolite *persculptus* Zone [Brenchley and Newall, 1984; Cocks, 1988; Sheehan, 1988; Brenchley, 1989; McLaren and Goodfellow, 1990; Wang *et al.*, 1993a; Wang *et al.*, 1993b; Sheehan *et al.*, 1996]. Several trilobite families, which had persisted through the initial phase of extinction, were almost entirely annihilated. The trilobites most affected by the second phase of extinction were those of oceanic, pelagic origin [Chatterton and Speyer, 1989]. Similarities arising from patterns of extinction between trilobites and graptolites suggest a link to variations in oceanic environments.

Brenchley and Newall [1984] have identified a slight decline in diversity of the *Hirnantia* fauna at the Rawtheyan-Hirnantian boundary and a more drastic decline during the Hirnantian, more specifically at the base of the *G. persculptus* Zone. The main phase of extinction for conodonts occurred in the upper *persculptus* Zone. It appears to have slightly lagged behind the graptolite extinction event [Barnes *et al.*, 1995]. Conodont

faunal diversity fell dramatically, from ~75-100 species in the lower-middle Ashgill to ~20 species in the lower Llandovery [Sweet, 1988]. The analysis of conodonts at the boundary section of Anticosti Island (Ellis Bay Formation) reveals that while 38 species are present in the uppermost Ashgill strata, only 21 species are apparent in the strata of lowest Silurian age, 16 of which have not been observed in older strata [McCracken and Barnes, 1981; Barnes, 1988b; Barnes and Bergstrom, 1988; Sweet, 1988]. The surviving species are predominantly coniform taxa. Prior to the extinction event, conodonts were partitioned into two distinct faunal realms: Mid-Continent and North Atlantic [Barnes and Bergstrom, 1988]. It appears that during the Ashgill, the northward movement of Baltica towards Laurentia, which eventually caused the Iapetus Ocean to come to a close, enabled some Mid-Continent taxa to infiltrate into European Ashgill faunas. The radiation event which took place above the upper *G. persculptus* Zone, involved species which mostly belonged to the low latitude warm-water Mid-Continent Realm. Species from the cold-water North Atlantic Realm became almost entirely extinct during the upper Ashgill bioevent [Barnes and Bergstrom, 1988].

1.4.4 Patterns of recovery

While patterns of extinctions have been studied in great detail, the faunal recovery at the beginning of the Silurian has not yet received significant attention. Sheehan *et al.* [1996] studied these patterns of recovery on the North American continent and argued that the Early Silurian represented a time of ecological instability. Diversity levels rose for a short time interval (several million years) while communities turned over frequently before stability became fully restored during late Llandovery time. Familial and generic diversity slowly returned back to the levels existing prior to the extinction. Since the Ordovician was a time of plate dispersal, faunal provincialism was widespread. However, more cosmopolitan faunas are characteristic of the subsequent Silurian due to the ecological filtering which occurred during the extinction events [Sheehan, 1988].

1.4.5 Causes of extinction: Links to glaciation

A unique cause for the extinction events is unknown and is most likely non-existent. However, it appears that the driving force behind the extinctions was the climate change, which resulted in the growth and decay of the Gondwana ice caps, and subsequent change in ocean temperatures and circulation. This scenario of extinction includes eustatic sea level changes and subsequent reduction of habitat [Berry and Boucot, 1973; Stanley, 1986; Sheehan, 1988; Sheehan *et al.*, 1996], paleoceanographic changes [Wilde and Berry, 1984; Wilde, 1991], global cooling [Stanley, 1984], possible asteroid impact [Orth *et al.*, 1986; Goodfellow *et al.*, 1992; Wang *et al.*, 1993a; Wang *et al.*, 1993b], and any of the above combinations. These mechanisms are discussed in the following sections.

1.4.5.1 Sea level changes

Until recently, the glacial maximum of the late Ashgill was often referred to as the cause of the extinction events. However, it now appears unlikely that glaciation initiated the observed extinction because many taxa survived well into the glacial period [Boucot, 1990; Sepkoski, 1995b]. Changes in sea level affect species-diversity through the species-area effect. Hence, the larger the habitable area, the greater is the species diversity [Brenchley *et al.*, 1995]. The significantly lower sea level stands during the Hirnantian drained and exposed vast regions, which consisted of shallow marine environments during the Rawtheyan [Sheehan, 1988; Sheehan *et al.*, 1996]. Karst surfaces have been observed in North America and Greenland, confirming that carbonate platforms were exposed for some time during the Hirnantian Stage [Kobluk, 1984; Brenchley *et al.*, 1995]. However, the extinction capability of such a mechanism has been criticised based on the fact that large numbers of modern species survive on small areas of the sea floor [Stanley, 1986]. In addition, evidence from several bathymetric records (Norway, Prague Basin and Wales) shows relatively slow initial fall in sea level and a maximum fall in the middle of the Hirnantian when the continental shelves and platforms would have been exposed [Brenchley *et al.*, 1995].

Links between patterns of extinction and changes in sea level have been summarised by *Barnes et al.* [1995] and *Sheehan et al.* [1996]. The initial pulse of extinction apparently took place prior to the peak glaciation as sea level began to decrease eustatically, draining epicontinental seas (increasing albedo of the exposed continents which is defined as the ratio of the reflected over the incoming solar radiation) and consequently enhancing the climatic gradient. The second and final pulse of extinction occurred when the glaciation ended abruptly, sea level rose to nearly preglaciation levels and epicontinental seas covered extensive parts of the continents again, decreasing the climatic gradient [*Sheehan et al.*, 1996]. At this time, most members of the widely distributed *Hirnantia* fauna became extinct, perhaps as a result of the warming at the end of the glaciation which eliminated their favoured habitat [*Sheehan and Coorough*, 1990].

1.4.5.2 Paleooceanographic changes

The abrupt extinctions of planktonic faunas and deeper-water elements of the benthos at the Rawtheyan-Hirnantian and the Hirnantian-Rhuddanian boundaries have implied important changes in oceanic temperatures and circulation [*Berry and Wilde*, 1990; *Finney and Xu*, 1990]. Oceanic environments may have deteriorated at rates beyond the tolerance levels of the species affected.

Given a long period of environmental stability, such as the uniformly warm 'greenhouse' climates of the Late Cambrian and the Early/Middle Ordovician [*Fischer*, 1981] it is possible that anoxic waters (where consumption of oxygen by organisms exceeds the rate of oxygen supply) developed below the wind-aerated surface waters and led to large-scale euxinification. The presence of widespread, laminated organic-rich black shales during that time gives further support to a deep-sea anoxic event and for enhanced productivity with increased carbon burial. Black shales are rich in organic carbon and iron sulphide. They often contain a wealth of well-preserved pelagic graptolites and are generally devoid of benthic fossils. Black shales also suggest that during the time of their formation, ocean circulation was sluggish or even inhibited by the presence of fresh, brackish surface waters. Evidence from the British Isles collected by

Leggett et al. [1981] shows that after an abrupt disappearance from the stratigraphic record in the Ashgill, simultaneous to an eustatic regression, widespread black shales appeared again at the base of the Llandovery.

The *gracilis* transgression, which began in early Caradoc, caused the flooding of extensive continental areas. In regions of net evaporation, these newly created epicontinental seas became ideal sites for the creation of warm saline bottom waters. *Brass et al.* [1982] developed a simple convection model driven by turbulent buoyant plumes for studying the mechanisms responsible in the production of warm saline bottom waters. According to their model, the creation of large flooded continental areas simultaneous to times of increased seafloor spreading and continental breakup and located in net evaporation zones would be conducive for generating warm saline bottom waters. *Railsback et al.* [1990] presented morphological and oxygen isotope data from brachiopods of the Trenton Group in New York (Caradoc Series), which suggest that Early Ordovician oceans had a stable, although weak, stratification, and were characterised by warm and saline deep waters in low to mid-latitudes (10-40°N and S). *Berger and Thierstein* [1979], *Leggett* [1981], *Wilde and Berry* [1984], *Jeppsson* [1990], *Wilde* [1991], *Wilde et al.* [1991] and *Holmden et al.* [1998] have discussed the climatic and biotic consequences of transferring from a stable ocean to one with strong circulation of cold bottom waters.

Wilde and Berry [1984] focused on the effect of climatically induced oceanic overturn. They argued that the disruption of this stable stratification could occur when high-latitude water, which forms at about 5°C, has a similar density as middle-latitude higher salinity water. Hence, during climatic cooling episodes (or warming episodes), the site of oceanic deep-water formation would shift from middle to high latitudes (or from high to middle latitudes). If the climate shifted into a sudden 'icehouse' for example, cold and dense water would sink at the poles and spread towards lower latitudes. Initiation of vertical motion at the boundary between warmer saline bottom water and overlying cooler fresh, high-latitude water could create an instability sufficiently large to make the body of water overturn. This would result in widespread upwelling, bringing bottom waters, rich in nutrients and metal cations to the surface.

With rapid vertical advection of these materials, they may enhance productivity or in some extreme situations prove to be toxic to some near-surface biota and hence, induce mass mortality. *Wilde and Berry* [1984] also argued that a shift from cold to warm climates could induce a second phase of overturn. This is supported by *Leggett et al.* [1981].

1.4.5.3 Climatic changes

For a climatic change to be the dominant cause of extinction, it must occur rapidly. In addition, the change must not only displace climatic belts but also shift them quickly or eliminate some entirely [*Stanley, 1984; Stanley, 1986*]. *Brenchley et al.* [1995] have noted that the magnitude of the shift during the Late Ordovician appears too large to be solely an outcome of the glacial "ice volume" effect, and that a change in seawater temperature of at least 8°C is more likely. Because the data originated from tropical areas, the implication is that tropical seawater temperatures fell considerably. Hence, a global ocean cooling could have displaced climatic belts and potentially caused the observed extinctions if the migration of the biota was hindered by the geographic configuration of the continents [*Lewin, 1984; Stanley, 1984*].

1.4.5.4 Changes in continental distribution

During the Late Ordovician, rapid changes in global climatic conditions have been explained as a result of unusually fast rates of plate movement [*Piper, 1987*]. *Wilde et al.* [1991] argued that from the absence of meridional continental barriers, Northern Hemisphere currents in the Panthalassic Ocean would have been zonal, with west or east flow, as well as low levels of nutrients in surface waters. In the Southern Hemisphere however, the continental masses would have forced meridional surface flows, transporting warm surface waters from low to high latitudes and cold, deep polar waters toward equatorial latitudes. The Iapetus Ocean, which lay between Laurentia, Siberia and Baltica-Avalonia, closed near the Middle Devonian. While Baltica and part of the Avalonian Island Arc travelled northward and induced the closure of the Iapetus Ocean, a substantial reduction of provincialism of benthic and planktonic faunas followed

[Stanley, 1986]. However, the short timescales involved in the two phases of extinction are not compatible with tectonic processes.

1.4.5.5 Asteroid impact hypothesis

The *asteroid impact hypothesis*, put forth by Luis Alvarez in 1980, suggests that throughout Earth's history, asteroids have struck the earth repeatedly, producing impact craters and ejecting dust-sized material into the stratosphere [Alvarez *et al.*, 1980]. This dust blanket would inhibit sunlight from reaching the earth, suppress photosynthesis and potentially induce a collapse of most food chains, resulting in a mass extinction. For the K-T boundary, the hypothesis that the impact of an extraterrestrial body triggered the terminal Cretaceous extinction is now well accepted. It is supported by the anomalous detection of high Iridium (Ir) concentrations (an element found in high concentrations in most solar system material) and the discovery of the Chicxulub crater on the Yucatan plate [Swisher *et al.*, 1992].

For the Late Ordovician case, the extent and apparent global synchronicity of extinction events suggest that the cause may have been a sudden or catastrophic event. However, efforts to locate an Ir layer in support of a bolide impact, at the stratigraphic level of the Hirnantian extinctions, have been largely unsuccessful [Wilde *et al.*, 1986]. Orth *et al.* [1986] examined the shallow-marine carbonate sequence of Anticosti Island, Québec for geochemical evidence of an impact. They argued that the origin of the observed Ir anomaly was not extraterrestrial based on the lack of evidence for a chondritic suite of siderophile elements and also on the absence of shocked quartz or spherules. Wang *et al.* [1993b] conducted geochemical analysis on Ordovician-Silurian boundary sections of graptolitic shales and mudstones in the Yangtze Basin on the South China Plate. They also found elevated values of Ir as well as high concentrations of other siderophile elements in the extinction horizon at the base of graptolite *persculptus* Zone. However, they concluded that the signal was an artefact of low sedimentation rates and reduced water conditions. In spite of the lack of evidence, Goodfellow *et al.* [1992] argued that an extraterrestrial source could not be ruled out because sampling intervals are often too coarse to adequately detect a thin layer characteristic of an impact.

Furthermore, they maintained that a catastrophic event such as a bolide impact should still be considered as a plausible cause of global extinction in that it may have provided a critical forcing on a biota, which was already under severe stress as a result of glaciation.

1.5 Chronology

Dating continental glacial deposits is particularly difficult because they are generally devoid of fossils [Flint, 1971]. Biostratigraphy is used to date fossiliferous beds located above and below the deposits and provide an estimate of a time frame under which glacial deposition took place [Brenchley and Newall, 1984; Brenchley et al., 1991]. Of all the glacial deposits found on the African continent, only those in Morocco in the central Anti-Atlas region have been precisely dated. The deposits are intercalated with an upper Ashgill, *Hirnantia* fauna [Destombes and Willefert, 1988; Paris et al., 1995].

Dating glacio-marine diamictites relies on two basic approaches: biostratigraphy and event-stratigraphy. Biostratigraphy may provide precise dating information of the uppermost Ashgill stratigraphic level (Hirnantian), since the unique *Hirnantia* fauna distinguishes the deposits. This technique has been applied widely throughout Europe, China, North America, Asia and the former U.S.S.R [Rong, 1984] as well as in South America [Benedetto, 1986]. It has been an effective method for identifying rocks of Hirnantian age. Event-stratigraphy is an approach used when faunal evidence is insufficient [Brenchley, 1989]. This technique is based on the principle that the growth and decay of an ice-sheet exert global effects on sea levels and on the isotopic composition of seawater. Within the Ordovician, there were several transgressions with at least one with a well-documented eustatic signal [McKerrow, 1979; Brenchley and Newall, 1984; Ross and Ross, 1992].

The Late Ordovician glacial period emerged after the uniformly warm 'greenhouse' climates of the Late Cambrian and the Early/Middle Ordovician [Fischer, 1981; Fischer, 1982; Fischer, 1986; Frakes et al., 1992]. Frakes et al. [1992] compiled data from the literature and argued that evidence from continental glacial deposits and

glacio-marine sediments, suggest that glacial inception probably began during the Caradoc (464 – 443 Ma) and reached its maximum during the Ashgill, more specifically during the Hirnantian Stage (~440 Ma). The major ice-sheet then covered at least North-Central and West Africa, which was centred near the South Pole.

Event stratigraphy conducted in Northwest Africa suggests three to four major growth phases of the continental ice cap from the late Caradoc through the Ashgill [Barnes, 1986]. These results are based on three separate horizons of till in the Saharan and South African sequences and have a limited precision. These pulses correlate well with the four regressive sequences observed in the tropical carbonate belt of Anticosti Island, Québec [Barnes *et al.*, 1995] whereas for the clastic sequence in the Oslo region, Norway, only two major regressive phases are apparent [Petryk, 1981]. Attempts to correlate the evolution of the Pleistocene ice caps with the cyclic changes in the $^{18}\text{O}/^{16}\text{O}$ isotopic record have been successful based on Milankovitch's theory of orbital parameters as forcing for the cyclical occurrence of ice ages [Milankovitch, 1938; Hays *et al.*, 1976]. Brenchley [1988] suggested that a similarly caused periodicity might have driven the observed sea-level oscillations and the creation of the three tills during the Hirnantian.

Whereas the ice sheet probably began to retreat during the Llandovery (~438 Ma) and had disappeared completely by the end of the Wenlock (421 Ma), smaller glacial centres developed in southern Africa and southern Brazil, apparently following the motion of Gondwana over the South Pole [Caputo and Crowell, 1985; Caputo, 1998]. Glacial deposits found in the Andean belt and in northern Brazil may reflect a motion reversal of the pole. Oxygen isotopic data does indicate three glacial phases within the Llandovery, likely reflecting the waning phases of the terminal Ordovician glaciation [Veizer *et al.*, in press].

1.6 Timing

Recent efforts have aimed to resolve the timing of the Late Ordovician glaciation because it is an important factor for determining the mechanisms responsible for its

inception and duration. Presently, no official consensus has been reached. Different authors propose strikingly different scenarios, using the evidence that best supports their theses. In the following sections, we review some of the approaches used to estimate the duration of the glaciation in order to provide a comprehensive outline of some of the remaining unresolved questions.

1.6.1 Evidence from glacio-marine deposits

The initiation of an icecap and its effect on sedimentation remain unclear. According to *Crowell* [1978], marine deposits associated with the initiation of a glaciation have few glacial imprints but may coincide with the time of maximum deposition, when sea levels begin to fall eustatically [*Brenchley et al.*, 1994]. However, the glacio-marine deposits from the Sahara appear contemporaneous to the melting of the ice cap [*Legrand*, 1995]. Although the dating of glacio-marine deposits remains problematic, evidence from North Africa suggests that marine conditions returned to normal during the late Hirnantian [*Legrand*, 1995].

1.6.2 Evidence from geochemical isotopic excursions

The stratigraphic record of the Ordovician-Silurian boundary reveals significant isotopic excursions (O, C, and Sr). The interpretation of these events has given rise to several potential time frames regarding the Late Ordovician glaciation. The oxygen, carbon and strontium isotopic records are reviewed in this section.

1.6.2.1 Oxygen isotopic data

Oxygen isotope curves contain historical evidence of past glacial and interglacial times. For example, increases in $\delta^{18}\text{O}$ may reflect the crystallisation of a substantial fraction of the ocean water mass as glacial ice, which is very light in $\delta^{18}\text{O}$ [*Holser et al.*, 1995]. The oxygen isotopic record from sections in the Siljan area and from the Boda Limestone carbonate mudmounds of central Sweden provides evidence for a short 'icehouse' period at the end of the Ordovician [*Marshall and Middleton*, 1990; *Middleton*

et al., 1991]. The $\delta^{18}\text{O}$ values were derived from brachiopods and marine cements. The isotopic measurements show approximately constant values of $\delta^{18}\text{O}$ throughout the pre-Hirnantian period ($\sim -4\text{‰}$ where ‰ represents parts per thousand), a significant enrichment in $\delta^{18}\text{O}$ ($\sim -2\text{‰}$) during the Hirnantian and an abrupt fall to $\sim -4\text{‰}$ at the end of the stage.

A recent high-resolution isotopic study, conducted over 2000 calcitic and phosphatic shells (mostly brachiopods with some conodonts and belemnites), has revealed more detailed features of the $\delta^{18}\text{O}$ curve (Figure 1.3) [Veizer *et al.*, 1997a; Veizer *et al.*, 1997b; Veizer *et al.*, in press].

The terminal Ordovician $\delta^{18}\text{O}$ peak of -2‰ (within the *acuminatus* Biozone) is a global signal and has been observed in China, the Baltic region, Canada and Argentina [Brenchley *et al.*, 1995]. There are three major $\delta^{18}\text{O}$ oscillations, subsequent to the Late Ordovician, which become apparent with this high-resolution study. The three positive excursions are believed to indicate global cooling trends and also coincide with glacial sediments. They occur at the Rhuddanian-Aeronian boundary, the Aeronian-Telychian boundary and at the base of the Wenlock age. This new evidence suggests that although glacial maximum may have occurred during the Hirnantian, the glaciation may not have been confined to this stage. In fact, it may have lasted until the beginning of the Wenlock.

Based on oxygen and carbon isotopic data, as well as bathymetric evidence, Brenchley *et al.* [1995] argued for a short-lived Ordovician glaciation. However, the oxygen isotopic data used in their assessment is limited to the narrow Ordovician-Silurian boundary interval. As reviewed above, recent evidence, which extends beyond this boundary, argues for a longer glaciation.

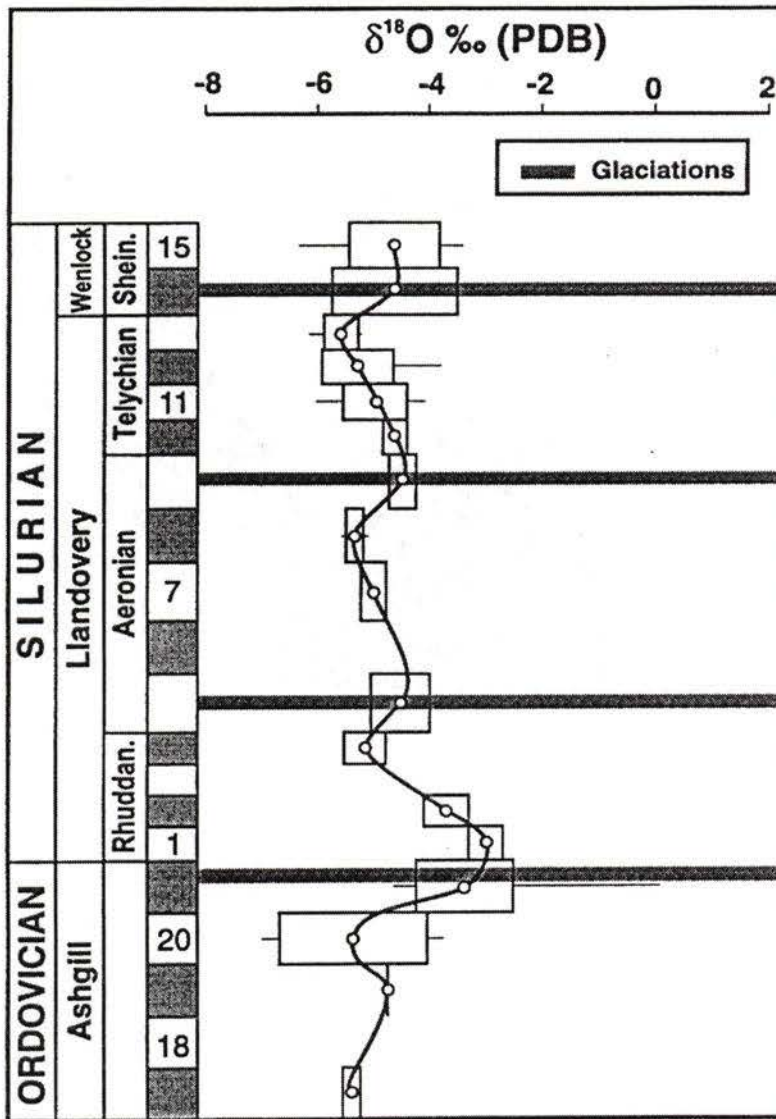


Figure 1.3 The $\delta^{18}\text{O}$ trend across the Ordovician/Silurian transition [Veizer *et al.*, in press]. Glacial episodes after Grahn and Caputo [1992].

1.6.2.2 Carbon isotopic data

The carbon isotope compilation provided by Brenchley *et al.* [1995] reveals a distinct positive shift at the end of the Ordovician, which suggests a significant change in the mode of carbon cycling. This global signal shows an increase of heavier carbon (^{13}C) towards a $\delta^{13}\text{C}$ maximum. It has been observed in the Siljan area, central Sweden [Marshall and Middleton, 1990; Middleton *et al.*, 1991], in a core section from Latvia (Brenchley *et al.*, 1992), in Wisconsin, USA [Yapp and Poths, 1992], on Anticosti Island,

Québec [Long, 1993], in the central Mackenzie Mountains, Northwest Territories [Wang *et al.*, 1993b], in Midwest USA, Anticosti Island and Baltic States [Brenchley *et al.*, 1994; Brenchley *et al.*, 1995] and in the Yangtze Sea, South China [Wang *et al.*, 1997]. In general, the $\delta^{13}\text{C}$ values in the pre-Hirnantian strata remain fairly constant around +1‰, but increase abruptly to maximum values of ~+5 to +7‰ at the base of the Hirnantian. These values remain high throughout the lower Hirnantian and decrease rapidly to ~+2‰ in the middle section of the stage.

The large positive shift at the beginning of the Hirnantian is one of the greatest recorded in the Phanerozoic. Variations observed in $\delta^{13}\text{C}$ curves reflect changes in the balance between organic and inorganic oceanic carbon reservoirs. Because ^{12}C is lighter and easier to handle metabolically, it is preferentially taken-up by organic matter. The residual dissolved inorganic carbon available for incorporation into shallow-water skeletal carbonates may become isotopically heavier (increasingly positive) for two reasons: either when rates of organic carbon burial in sediments are high or when rates of biological productivity increase and stimulate carbon cycling.

The widespread distribution of the carbon isotopic shift in the latest Ordovician suggests that it was of global significance and that it may have had a common origin. Wang *et al.* [1993b] proposed that a decrease in $p\text{CO}_2$ in the ocean and atmosphere, together with a greater organic carbon burial rate during the Hirnantian, may have caused the positive carbon isotopic shift. Higher than usual organic carbon burial rates may be expected during glacial times. However, it is difficult if not impossible at this point to determine which of these mechanisms is more likely. In addition, direct evidence for either enhanced sedimentation rates of carbon or for high productivity during the Hirnantian have not yet been found [Brenchley *et al.*, 1995].

1.6.2.3 Strontium isotopic data

The strontium isotope record provides an estimate of rates of oceanic crust production over geologic time. It is especially useful when the record has only some partially preserved original crust, as is the case for the Ordovician. River inflow,

especially for those transporting erosional debris from old metamorphic and igneous rocks, tends to preferentially carry heavy $^{87}\text{Sr}/^{86}\text{Sr}$ while exchange of Sr with young basalts in the vicinity of sea-water hydrothermal vents beneath mid-ocean ridges contributes light $^{87}\text{Sr}/^{86}\text{Sr}$ [Holser *et al.*, 1995]. The Strontium isotope curve shows a moderate decrease from Tremadoc to Llandeilo, from 0.7091 to 0.7087, an abrupt excursion to 0.7078 during the late Llandeilo-early Caradoc, little variation during the Caradoc and the Ashgill and a constant rise to 0.7087 through the Silurian [Holser *et al.*, 1995; Veizer *et al.*, 1997a; Qing *et al.*, 1998; Ruppel *et al.*, 1998; Veizer *et al.*, in press]. The gradual decrease in the Sr isotope ratio during the Early Ordovician may be an outcome of a global decline in the topographic relief and in weathering rates characteristic of the waning phases of Pan-African orogenies [Qing *et al.*, 1998]. In addition, the *gracilis* transgression, which caused flooding of vast cratonic areas, may have inhibited the radiogenic riverine Sr flux to the oceans. The abrupt excursion close to the Llandeilo/Caradoc boundary supports the idea of increased oceanic input of Sr and suggests a possible superplume event [Barnes *et al.*, 1995]. A mantle superplume is defined by its intensity; it is thought to be about an order of magnitude larger than normal plume activity and expands over several thousands of kilometres. A superplume appears to originate at the core-mantle boundary and then rises through the mantle until it reaches the lithosphere. The occurrence of a superplume event during the Ordovician may have played a conditioning role for the setting of an unstable climate during the Late Ordovician. The later gradual increase in the Sr isotope curve during the Silurian may reflect several events: the Taconic Orogeny which peaked during the Caradoc, the increased mechanical erosion of continental Sr and frost-shattering effects concurrent to the Late Ordovician glaciation [Armstrong, 1971], the possibly enhanced chemical weathering of continental rocks due to high atmospheric CO_2 levels or the Early Silurian Salinian Orogeny [Cawood *et al.*, 1994].

1.6.3 Evidence from eustatic sea level changes

Vail [1977], Leggett *et al.* [1981], Johnson *et al.* [1981], Brenchley and Newall [1980], Fortey [1984], and Ross and Ross [1992] have discussed Ordovician eustasy.

Brenchley [1994] compiled a series of Late Ordovician bathymetric curves and extracted from them two common aspects. First, the section of the record of Caradoc age shows a long-term rise in sea level beginning in early Caradoc. This is often referred to as the *gracilis* transgression and is the largest in the Phanerozoic in terms of cratonic area submerged [*Ross and Ross*, 1992]. Second, the section of the curves representing the Ashgill Series shows a short-term fall in sea-level at the base of the Hirnantian [*Brenchley and Newall*, 1980] and a subsequent rise in sea-level in the upper part of the Hirnantian, which is below or within the *G. persculptus* Zone [*Ross and Ross*, 1992]. Since these eustatic signals appear synchronous, *Brenchley et al.* [1994] used them for correlation and argued for a short-lived glaciation.

Alternatively, bathymetric evidence showing a rapid regression at the Caradoc-Ashgill boundary and supporting the idea of a longer glaciation, have been reported by *Fortey* [1984], *Barnes* [1986; 1988b] and *Ross et al.* [1992]. *Barnes et al.* [1995] have argued that the glacial period linked to these eustatic changes spanned the entire Ashgill Series and that three to four glacial oscillations took place during the Hirnantian Stage. Evidence from the carbonate sedimentary record of Anticosti Island supports the idea of four regressive phases during the Hirnantian glaciation [*Barnes*, 1988a]. *Berry and Boucot* [1973] have also argued that sea level decreased glacio-eustatically several times during the Hirnantian glaciation. They suggested that the shallowing of marine waters across the Late Ordovician platforms was closely linked to the 'locking' up of oceanic waters during glaciation. There are two main regressive sequences evident in the clastic sequence in the Oslo region, Norway [*Brenchley and Newall*, 1980; *Brenchley and Cocks*, 1982]. Estimates of the changes in sea level within the Hirnantian Stage vary from 50-100 m [*Brenchley and Newall*, 1984], to less than 20 m [*Xu*, 1984], to 32-36 m [*Long*, 1993]. *Crowley and Baum* [1991] estimated a change in sea level of ~60 m (sea level equivalent) or ~45 m (with isostatic readjustment) based on the extent of Gondwanan glacial deposits which appears to be on the same order of magnitude as the present East Antarctic ice sheet. Substantial evidence exists for a widespread carbonate deposition event during the latest Rawtheyan Stage, immediately before the initial Hirnantian regression [*Spjeldnaes*, 1981]. This horizon suggests a temporary climatic

excursion to warmer conditions before the glaciation. Furthermore, the widespread Caradocian transgression may in part be the result of a superplume event [Barnes *et al.*, 1995].

1.6.4 Cautionary notes

As the timing issue is clearly unresolved, a few cautionary notes need to be mentioned. If the glaciation did turn out to be less than 1 m.y. (i.e. restricted to the Hirnantian; 0.5 m.y.) [Harland *et al.*, 1989], then Berner's geochemical modelling estimates for atmospheric CO₂ levels (8x – 20x pil) (Section 1.8.1) would not apply as the model has a timestep of 10 m.y. [Berner, 1991; Berner, 1994]. In addition, Yapp and Poth's estimate [1992] of CO₂ levels (16x pdl) based on the analysis of goethite may not coincide with the Late Ordovician glaciation (Section 1.8.1). Hence, the existence of the paradox investigated in this thesis, which is the occurrence of a widespread glaciation simultaneous with very high CO₂ levels, is in itself debatable. If the glaciation was of short duration, CO₂ levels may have been low during that time. Based on the isotopic and eustatic evidence, I choose to assume for this study that the glaciation, although it may have peaked during the Hirnantian, was initiated during the late Caradoc and persisted through the Llandovery. Hence, even if CO₂ levels were indeed especially low for a short period of time simultaneous to the glacial maxima, the climatic conditions that led to the glacial inception may have included CO₂ concentrations 10-18x pre-industrial levels.

1.7 Extent

The spatial distribution of Late Ordovician glacial deposits on the Gondwana continent suggests that land-based ice spread outwards to at least 40°S. The floating ice may have extended a further 10° equatorwards [Brenchley and Newall, 1984]. There is no direct evidence of a contemporary ice cap in the Ordovician Northern Hemisphere [Brenchley, 1988] partly since no cratonic areas were located in the northern high latitudes. The precise size of the ice sheet during glacial maxima is not known.

However, *Beuf et al.* [1971] and later *Hambrey* [1985] estimated an area from the present outcrops found in Algeria, Mali, Morocco, Mauritania, Guinea and Sierra Leone of $6-8 \times 10^6 \text{ km}^2$. *Crowley and Baum* [1991], accounting for some erosion, revised this estimate to $11.8 \times 10^6 \text{ km}^2$. This is comparable with the estimated area of the Laurentide ice sheet at glacial maxima during the Pleistocene ($11.6 \times 10^6 \text{ km}^2$) and with the present area of the East Antarctic ice sheet ($10.4 \times 10^6 \text{ km}^2$) [*Denton et al.*, 1971; *Paterson*, 1972]. The magnitude of sea level fluctuations evident in the carbonate siliciclastic sequences on Anticosti Island (Québec), imply a maximum ice volume of $\sim 12-14 \times 10^6 \text{ km}^3$ [*Long*, 1993]. In comparison, modern continental ice has a volume of $33.0 \times 10^6 \text{ km}^3$ [*Hartmann*, 1994]. Analysis of chitinozoan assemblages from glacio-marine deposits also suggests that the Late Ordovician glacial maxima occurred over a fairly short time interval (i.e. about 2 m.y.) [*Paris et al.*, 1995].

1.8 Reviewing the paradox: glaciation vs. high atmospheric CO₂

The analysis of the geological, chemical and paleontological records of the Ordovician Period has given rise to an apparent paradox stemming from the occurrence of the Late Ordovician glaciation, one of the three most important glacial periods in the Phanerozoic (last 570 m.y.) simultaneous with high atmospheric CO₂ concentrations. The purpose of this thesis is to address this paradox by investigating the ocean's role in the climate of the Late Ordovician through modelling experiments. In this section, we provide a background review of this paradox as well as previous attempts to resolve it.

1.8.1 Evidence for high atmospheric CO₂ levels

Carbon dioxide molecules are transparent to short-wave solar radiation but are strong absorbers of infrared radiation reradiated by the earth at longer wavelengths. The analysis of goethites from an ironstone in the Upper Ordovician Neda Formation (Wisconsin, USA) has yielded an atmospheric $p\text{CO}_2$ value for the Late Ordovician of about 16x present-day levels ($\text{pdl} \cong 350 \text{ ppm}$) [*Yapp and Poths*, 1992]. The high CO₂ levels derived from goethites may in part reflect the elevated sea levels which resulted

from the increased rates of seafloor spreading and volcanism (source of atmospheric CO₂) and followed the breakup of the presumed Late Precambrian supercontinent Rodinia [Hoffman, 1991]. In addition, Early Paleozoic CO₂ levels may have been higher because land plants had not yet evolved (sink of atmospheric CO₂).

These results appear to be in general agreement with the geochemical modelling experiments conducted by *Berner and Lasaga* [1989] and *Berner* [1990; 1991; 1994] for the entire Phanerozoic. The processes considered in this model include sedimentary burial of organic matter and carbonates, continental weathering of silicates, carbonates and organic matter, and volcanic and metamorphic degassing of CO₂. The model predicted atmospheric *p*CO₂ levels about 14 ± 6 x present atmospheric levels (Berner's estimate of *p*dI = 300 ppm) (Figure 1.4). These results must be interpreted with caution since some of the assumptions used may be incorrect if applied to the Late Ordovician context. The assumptions are that all carbon is lumped together (the ocean-atmosphere are combined into one reservoir), and that the calculation of CO₂ levels in the atmosphere is made as a succession of steady states, with a time step of 10 m.y.

High atmospheric CO₂ levels have traditionally been associated with warm, ice-free climates. As previously mentioned, the stable isotope record and eustatic sea-level curves both suggest that glacial inception may have been initiated during the Caradoc but reached its maximum during the Ashgill, more specifically during the Hirnantian Stage [Brenchley *et al.*, 1995]. Hence, if the Late Ordovician glaciation was indeed short-lived, then the timescales considered in Berner's modelling experiments are inadequate. However, because of the uncertainties inherent within these estimates, I have opted for investigating the climate derived under the potentially higher CO₂ levels.

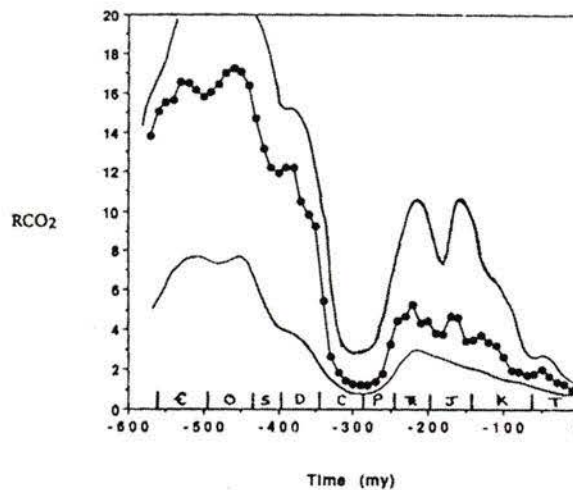


Figure 1.4 RCO_2 levels as a function of time according to GEOCARB II modelling experiments where RCO_2 is the mass of atmospheric CO_2 at time t divided by that at “present” (≈ 300 ppm). Upper and lower curves indicate rough error estimates. From *Berner* [1994].

1.8.2 Previous climate modelling experiments

1.8.2.1 A geography problem

This paradox has been addressed through several climate modelling experiments. Originally, it was believed that the land-sea distribution of the Late Ordovician played a determinant role in initiating glaciation [*Crowley et al.*, 1987; *Crowley and Baum*, 1991; *Crowley et al.*, 1993a; *Crowley et al.*, 1993b; *Zimmer*, 1994].

Caputo and Crowell [1985] studied the displacement of glacial centres across Gondwana during the Paleozoic. They noticed that the intensity of the glaciation appeared to wane when Gondwana moved northward and its edge was no longer over the South Pole. This may in part be due to the large heat capacity of the ocean, which tends to suppress the magnitude of the warming on adjacent land areas. A stronger seasonal cycle would also be expected if the pole was located in the middle of the supercontinent Gondwana (i.e. very cold temperatures during the winter and relatively warm temperatures during the summer). This would most likely inhibit the formation of a permanent ice cover [*Hyde et al.*, 1990]. *Crowley et al.* [1987] showed through Energy Balance Model (EBM) experiments that the unique geographic configuration of

Gondwana (with a coastal location for the South Pole) could have allowed for permanent snow cover with higher CO₂ levels. However, the parameterisation of snow and sea ice in these models was simplistic. Subsequent experiments, which included non-linear ice-albedo feedbacks, gave further support to the geographic positioning hypothesis [Hyde *et al.*, 1990; Crowley and Baum, 1991]. A problem with this hypothesis resides in the fact that the long time scales involved in tectonic processes are incompatible with a short-lived Hirnantian glaciation. Hence, the particular geographic configuration of Gondwana may have only partly been responsible for the growth and decay of the Gondwana ice cap.

1.8.2.2 The faint sun theory

When the CO₂-glaciation paradox was first noticed, it was thought that perhaps a decrease in intensity of solar luminosity could account for the glaciation. Evolutionary models of the sun suggest that solar luminosity has increased throughout geologic time [Newman and Rood, 1977; Endal and Sofia, 1981; Bahcall, 1988]. A 3.5-5.0% decrease (relative to present-day forcing) in solar luminosity has been postulated for the Ordovician. However, as discussed in Section 3.1, the subsequent net change in radiative forcing ($\Delta F = \Delta \text{CO}_2 + \Delta \text{Solar}$) is always positive when increased CO₂ levels are considered. Hence, additional climatic processes need to be included in modelling experiments in order to yield an environment susceptible to glaciation.

Recently, Crowley and Baum [1995] attempted to reconcile this paradox using the GENESIS atmosphere general circulation model (AGCM) with a specified mixed layer slab ocean of constant depth [Thompson and Pollard, 1994]. As opposed to Energy Balance Models, which are limited to the prediction of the spatial distribution of surface temperatures without incorporating the hydrologic cycle and the snow balance, the GENESIS model includes a representation of the hydrologic cycle. Crowley and Baum [1995] conducted four experiments which included CO₂ levels 14x pil, solar luminosity reduced by 4.5% and an orbital configuration prescribed for minimum summer insolation receipt (Cold Summer Orbit: CSO). Their research focused on the effects of different combinations of ocean heat transport (1x vs. 1.5x symmetrized present day heat

transport) and topography (300-500 m) on high-latitude snow cover over the supercontinent Gondwana. The results of their experiments showed that for the slightly elevated topography case (500 m), permanent snow cover was observed where the geological record indicated the Ordovician ice sheet was present. Global runoff rates were 10-30% less than present. This result is especially relevant for the CO₂-runoff and weathering parameterisations in geochemical models.

Gibbs [1996] examined the sensitivity of the Late Ordovician climate to variations in atmospheric CO₂ using the GENESIS atmosphere general circulation model. A 4.5% lower solar luminosity was used in all experiments. Results from the 8x CO₂ experiment showed that snow rapidly accumulated and spread towards equatorial latitudes (run-away icehouse) whereas for the 10x experiment, a significant snow cover survived through the summer yet no runaway icehouse occurred. In addition, the spatial distribution of snow appeared consistent with the distribution of glacial deposits. There was no permanent snow cover in the 18x experiment. These results suggest a strong sensitivity to small changes in CO₂ and support a short-lived episode of increased organic-carbon burial giving rise to an abrupt drawdown of atmospheric CO₂.

Although substantial improvements have been made to solve the CO₂-glaciation paradox, much research remains to be done in order to complete our understanding of the Late Ordovician climate. As an extension to previous EBM studies, I conduct sensitivity experiments with an EBM which includes a moisture balance in addition to an energy balance [*Fanning and Weaver, 1996*]. Furthermore, the EBM used in this thesis is coupled to an OGCM. Whereas previous studies required prescribed ocean heat transports, the coupling of the present model eliminates this requirement. The sensitivity of the coupled ocean-atmosphere-sea-ice model to changes in CO₂, albedo and orbital forcing within the Late Ordovician context is assessed in this study. In addition, the ocean's role in the glaciation is discussed through the analysis of modelled poleward heat transport results.

2. Methodology

2.1 Model description

The model used in this study is the coupled version of three models representing the following three components of the climate system: the ocean, atmosphere and cryosphere. A description of each component of the coupled model is provided in the following sections: Section 2.1.1 (ocean model), Section 2.1.2 (atmosphere model) and Section 2.1.3 (ice model). The boundary and initial conditions used in the experiments are explained in Section 2.2.

2.1.1 Ocean model

The ocean model used in this study is the Geophysical Fluid Dynamics Laboratory (GFDL) Modular Ocean Model (MOM2) [Pacanowski, 1995]. This three-dimensional model stems from the earlier work of Bryan [1969]. It includes a finite difference version of the primitive equations based on a Boussinesq, hydrostatic fluid under the rigid-lid approximation. For simplicity, these equations are given below in Cartesian coordinates rather than spherical coordinates used in the model.

The conservation of momentum equations are as follows:

$$\frac{Du}{Dt} = fv - \frac{1}{\rho_o} \frac{\partial P}{\partial x} + A_H \nabla_H^2 u + A_V \nabla_V^2 v, \quad (2.1.1.1)$$

$$\frac{Dv}{Dt} = -fu - \frac{1}{\rho_o} \frac{\partial P}{\partial y} + A_H \nabla_H^2 v + A_V \nabla_V^2 v, \quad (2.1.1.2)$$

where D/Dt is the material derivative, u and v are the zonal and meridional velocities, f is the Coriolis parameter, ρ_o is a representative density for seawater and P is the pressure. The horizontal and vertical eddy viscosities are given by A_H and A_V whereas $\nabla_H^2 = \partial^2/\partial x^2 + \partial^2/\partial y^2$ and $\nabla_V^2 = \partial^2/\partial z^2$ are the horizontal and vertical Laplacian operators respectively.

The continuity equation, under the Boussinesq approximation is:

$$\frac{\partial u}{\partial x} + \frac{\partial v}{\partial y} + \frac{\partial w}{\partial z} = 0. \quad (2.1.1.3)$$

The hydrostatic fluid assumption is generally correct to 1 part to 10^6 . It may break down within convective plumes for which $u \sim w$. The hydrostatic balance is described as:

$$\frac{-1}{\rho} \frac{\partial P}{\partial z} + g = 0, \quad (2.1.1.4)$$

where ρ is the density of seawater given in 2.1.1.7 and g is the acceleration due to gravity.

The rigid lid approximation is made by requiring that the vertical velocity at the surface be zero. The purpose of this approximation is to permit the use of longer time steps. On the one hand, this is possible since surface gravity waves, which have rapid propagation speeds, are inhibited. On the other hand, Rossby waves for which the restoring force is the variation of the Coriolis force with latitude, are somewhat affected by this approximation. However, it is believed that it does not introduce significant errors, at least not when the model has achieved its final, quasi-steady state mode.

The equation for the conservation of heat is the following:

$$\frac{DT}{Dt} = \kappa_H (\nabla_H^2 T) + \frac{\partial}{\partial z} \kappa_V \frac{\partial T}{\partial z} + C + \text{surface sources/sinks}, \quad (2.1.1.5)$$

where T is the temperature, κ_H and κ_V are the lateral and vertical diffusivities and C represents convection. The equation for the conservation of salt, represented as S , is:

$$\frac{DS}{Dt} = \kappa_H (\nabla_H^2 S) + \frac{\partial}{\partial z} \kappa_V \frac{\partial S}{\partial z} + C + \text{surface sources/sinks}. \quad (2.1.1.6)$$

The heat and fresh-water fluxes are directly added in equations 2.1.1.5 and 2.1.1.6 at the surface via the sources/sink terms. The equation of state for seawater has a non-linear form [UNESCO, 1981]:

$$\rho = \rho(S, T, P). \quad (2.1.1.7)$$

The ocean's surface is driven by both a wind stress field, which is applied as a body force over the depth of the first grid box, and a surface buoyancy force. Hence, the surface boundary conditions are as follows:

$$\begin{aligned} w = \frac{\partial T}{\partial z} = \frac{\partial S}{\partial z} = 0 \quad \text{at } z = 0 \\ \rho_o A_v \frac{\partial u}{\partial z} = \tau_s^x \quad ; \quad \rho_o A_v \frac{\partial v}{\partial z} = \tau_s^y \end{aligned} \quad (2.1.1.8)$$

where w is the vertical velocity, τ_s^x and τ_s^y are the zonal and meridional surface wind stresses respectively.

The freshwater flux over the ocean's surface is given by:

$$Q_s = \begin{cases} S^*(E - P - R) & ; \text{if ice free} \\ (S^* - S_i)B - S^*(P + R - E) & ; \text{otherwise} \end{cases} \quad (2.1.1.9)$$

where S^* and S_i are representative salinities for the ocean and the ice, E is the evaporation, P is the precipitation, R is the runoff and B is the freshwater flux from ice formation or melt:

$$B = \frac{\rho_i}{\rho_o} \frac{\Delta H_i}{\Delta t}, \quad (2.1.1.10)$$

where H_i is the ice thickness.

A no-flux condition on both heat and salt tracers is prescribed at the lower boundary of the ocean model so that:

$$\underline{u} \cdot \underline{n} = \frac{\partial T}{\partial z} = \frac{\partial S}{\partial z} = 0 \quad \text{at } z = -H, \quad (2.1.1.11)$$

where \underline{n} is a unit vector normal to the bottom.

Furthermore, a quadratic bottom friction is applied as a body force over the depth of the last grid box [Weaver and Hughes, 1996]. Flow is also inhibited through all lateral boundaries. A cyclic boundary condition is used at the eastern and western boundaries of the model domain.

2.1.2 Atmosphere model

The atmospheric component of the climate system plays an elaborate and crucial role in the global energy balance. The atmospheric Energy Moisture Balance Model (EMBM) used in the experiments was developed by *Fanning and Weaver* [1996] through substantial improvement of earlier models [Budyko, 1969; Sellers, 1969; North, 1975]. It includes the basic thermodynamic and hydrological components of the climate system. It relies on the vertical integration of the energy-moisture equations where advection has been parameterised by an eddy-diffusive approximation. This approximation is realistic for the time scales (annual and longer) and spatial scales (>1000 km) which are investigated in the present study, since atmospheric transport due to advection takes place over much shorter time scales [Lorenz, 1979]. The model also assumes that for the time scales considered, there is no heat or water storage on land. This eliminates the need for computing latent, sensible and radiative heat fluxes over land. Through latent, sensible and radiative heat transfers between the ocean and the atmosphere, this model may be

coupled to an ocean model to investigate the ocean's role in past climates. A summary of the atmospheric parameters used in the model is given in Table 2.1.

2.1.2.1 Thermodynamic components

The atmospheric energy balance can be written as follows:

$$\rho_a H_a C_{\rho a} \frac{\partial T_a}{\partial t} = Q_T + (1 - C_o) Q_{SW} - Q_{PLW} + Q_{ULW} + Q_{SH} + Q_{LH}, \quad (2.1.2.1a)$$

where ρ_a is a constant air density, H_a is the constant scale height depth of the atmosphere, $C_{\rho a}$ the specific heat capacity of the atmosphere and T_a the surface air temperature. The rate of change of temperature in the atmosphere is dependent on the following fluxes: the eddy-diffusive horizontal heat transport (Q_T), the net incoming solar radiation (Q_{SW}), the net planetary emission of longwave radiation to space (Q_{PLW}), the net upward longwave flux from the surface (Q_{ULW}) and finally the sensible (Q_{SH}) and latent heat fluxes (Q_{LH}). C_o is the solar scattering coefficient. As estimated by *Ramanathan* [1987], approximately 30% of the incident short-wave radiative flux is reflected and scattered by water vapour, dust, ozone and clouds.

Because we assume no heat or moisture storage over land, rewriting 2.1.2.1a gives:

$$\rho_a H_a C_{\rho a} \frac{\partial T_a}{\partial t} = Q_T + Q_{SW} - Q_{PLW} + Q_{LH}, \quad (2.1.2.1b)$$

over land. The parameterisation for the eddy-diffusive horizontal heat transport is given by:

$$Q_T = \rho_a H_a C_{\rho a} \nu \left[\frac{\partial^2 T_a}{\partial x^2} + \frac{\partial^2 T_a}{\partial y^2} \right], \quad (2.1.2.2)$$

where x and y represent longitude and latitude respectively and ν is a latitudinally dependent heat diffusion coefficient.

The net incoming solar radiation is given as:

$$Q_{SW} = \frac{S_0}{4} I(1 - \alpha), \quad (2.1.2.3)$$

where S_0 is the solar constant, I is the annual distribution of incoming solar radiation entering the top of the atmosphere [Berger, 1978], α is the latitudinally dependent albedo. The planetary albedo parameter is also sensitive to the albedo contrast between snow and sea ice covered areas with neighbouring snow- and ice-free areas. This parameter allows the incorporation of ice-albedo feedbacks in the model.

The net planetary longwave flux to space may be calculated as follows:

$$Q_{PLW} = \varepsilon_p \sigma T_a^4, \quad (2.1.2.4a)$$

where ε_p is the planetary emissivity and σ is the Stefan-Boltzmann constant. However, this expression fails to consider the water vapour feedback on the longwave flux. Hence, we chose an alternative parameterisation [Thompson and Warren, 1982]:

$$Q_{PLW} = a_0 + a_1 T_a + a_2 T_a^2 + a_3 T_a^3 - F_{CO_2}, \quad (2.1.2.4b)$$

where $a_N = b_{0N} + b_{1N}r + b_{2N}r^2$, $N = 0, 1, 2, 3$, r is the relative humidity, b_{MN} are empirically derived constants (see Thompson and Warren [1982], Table 3) and F_{CO_2} is the radiative forcing by atmospheric CO_2 [IPCC, 1996].

Greenhouse gases present in the atmosphere strongly absorb longwave radiation emitted by the ocean. This energy is then re-emitted both upwards and downwards, giving rise to a longwave flux at the base of the atmosphere. This is done assuming the atmosphere emits as a grey body. These interactions translate into the following radiative flux:

$$Q_{ULW} = \begin{cases} \varepsilon_o \sigma T_o^4 - \varepsilon_a \sigma T_a^4 & ; \text{if ice free} \\ \varepsilon_i \sigma T_i^4 - \varepsilon_a \sigma T_a^4 & ; \text{otherwise} \end{cases} \quad (2.1.2.5)$$

where T_o and T_i are the sea and ice surface temperatures and ε_o , ε_i , ε_a are the emissivity values for the ocean, ice and atmosphere respectively.

The sensible heat flux is estimated through a traditional bulk parameterisation:

$$Q_{SH} = \begin{cases} \rho_a C_H C_{\rho a} U (T_o - T_a) & ; \text{if ice free} \\ \rho_a C_H C_{\rho a} U (T_i - T_a) & ; \text{otherwise} \end{cases} \quad (2.1.2.6)$$

where C_H is the Stanton number and U is the surface scalar wind speed.

The latent heat flux into the atmosphere is given by:

$$Q_{LH} = \rho_o L_v P, \quad (2.1.2.7)$$

where ρ_o is the density of the ocean surface, L_v is the latent heat of vaporisation and P is the precipitation.

2.1.2.2 Hydrological components

The atmospheric moisture balance is described as follows:

$$\rho_a H_q \frac{\partial q_a}{\partial t} = \rho_a H_q \kappa \left[\frac{\partial^2 q_a}{\partial x^2} + \frac{\partial^2 q_a}{\partial y^2} \right] + \rho_o (E - P), \quad (2.1.2.8)$$

where H_q is a constant scale height depth for the specific humidity, q_a at the standard level, P is the precipitation, E is the evaporation and κ is an eddy diffusive horizontal redistribution term which is derived from integrating the steady state, zonally averaged form of (2.1.2.8) and fitting to present-day observations of $E-P$. This approximation of the hydrological cycle substitutes the horizontal advection terms by an eddy-diffusive term and integrates over the depth of the atmosphere. The first term on the right-hand side is very similar to that of the heat transport parameterisation (Equation 2.1.2.2). This

appears to be a realistic approximation for large-scale atmospheric and stationary-eddy motions. However, this approximation breaks down at the Intertropical Convergence Zone (ITCZ). Hence, diffusive transport holds and is a viable parameterisation for latitudes poleward of approximately 20° .

A calculation of the evaporation (or sublimation over ice) is obtained from its traditional bulk formula:

$$E = \begin{cases} \frac{\rho_a C_E U}{\rho_a} (q_s(T_o) - q_a) & ; \text{if ice free} \\ \frac{\rho_a C_E U}{\rho_i} (q_s(T_i) - q_a) & ; \text{otherwise} \end{cases} \quad (2.1.2.9)$$

where C_E is the dimensionless Dalton number, $q_s(T_o)$ and $q_s(T_i)$ are the saturation specific humidities at T_o and T_i respectively. Saturation specific humidities are obtained from the following empirical formula [Bolton, 1980] and from the Clausius-Clapeyron equation:

$$q_s(T) = \begin{cases} 3.802 \times 10^{-3} \exp\left(\frac{17.67T_o}{T_o + 243.5}\right) & ; \text{if ice free} \\ 3.802 \times 10^{-3} \exp\left(\frac{22.38T_i}{T_i + 271.8}\right) & ; \text{otherwise} \end{cases} \quad (2.1.2.10)$$

The parameterisation for precipitation is as follows:

$$P = \frac{\rho_a H_q}{\rho_o \Delta t} (q_a - 0.85q_s(T_o)), \text{ if } r \geq 85\% \text{ and } 0 \text{ otherwise,} \quad (2.1.2.11)$$

where Δt is the atmospheric time step, $q_s(T_o)$ is the saturation specific humidity at T_o , r is the relative humidity. This forces precipitation to occur when the relative humidity is greater than 85%. When the atmospheric temperature falls below -10.0°C , precipitation is assumed to fall as snow. Over land, snowfall is redistributed in order to cover the entire grid cell whereas over sea ice, a fractional area is permitted. The presence of snow affects the energy balance by increasing the albedo of the surface and altering the

downward shortwave radiation calculation. When atmospheric temperatures rise above -10.0°C , the melt rate linearly increases from 0 cm/day to 5 cm/day at 0.0°C .

The advantages stemming from the usage of this EMBM are mainly its simplicity and computational efficiency. Coupling experiments between this model and MOM2 ocean general circulation model provide an adequate simulation of the present day climate without requiring the explicit use of flux adjustments [Weaver and Hughes, 1996]. However, the simple parameterisation of the diffusive moisture transport causes global precipitation rates to be too low compared to present-day observations. Precipitation patterns also fail to reproduce the belt of high precipitation associated with the Intertropical Convergence Zone.

Although this model highly simplifies the complexities of the atmosphere system, it is found to be a useful tool for process-oriented coupled ocean-atmosphere studies such as the one conducted in this thesis. A critical assessment of this model is given in *Fanning and Weaver* [1996].

Table 2.1 Atmospheric model parameters after *Fanning and Weaver* [1996]

| Parameter | Description | Value |
|--------------|-------------------------------|--|
| a | Radius of the Earth | 6371 km |
| $(1-\alpha)$ | Coalbedo | Figure 2d [<i>Fanning and Weaver, 1996</i>] |
| ρ_a | Surface air density | 1.25 kg/m ³ |
| ρ_o | Sea surface density | 1024 kg/m ³ |
| C_E | Dalton number | Figure 3 [<i>Fanning and Weaver, 1996</i>] |
| C_H | Stanton number | 0.94 C_E |
| C_o | Solar absorption coefficient | 0.3 |
| C_{pa} | Heat capacity of dry air | 10 ³ J/(kgK) |
| ϵ_A | Atmospheric emissivity | Figure 2a [<i>Fanning and Weaver, 1996</i>] |
| ϵ_P | Planetary emissivity | Figure 2b [<i>Fanning and Weaver, 1996</i>] |
| ϵ_O | Oceanic emissivity | 0.96 |
| H_a | Atmospheric scale depth | 8400 m |
| H_q | Specific humidity scale depth | 1800 m |
| κ | Eddy diffusivity for moisture | Figure 1 [<i>Fanning and Weaver, 1996</i>] |
| L_v | Latent heat of evaporation | 2.5 x 10 ⁶ J/kg |
| ν | eddy diffusivity for heat | Figure 1 [<i>Fanning and Weaver, 1996</i>] |
| S_o | Solar constant | 1360 or 1306 W/m ² |
| τ | Model time step | 0.5 days |
| σ | Stefan-Boltzmann constant | 5.67 x 10 ⁻⁸ W/(m ² K ⁴) |

2.1.3 Ice model

Although sea ice exerts a strong influence on the climate system, it remained largely unexplored in global climate models until recently [*Hibler and Flato, 1992*]. On small spatial scales, the sea ice interface affects heat and salt exchanges between the ocean and atmosphere. The presence of sea ice decreases the heat transfer between the ocean and the atmosphere, and hinders the ocean's capacity to moderate climate via local

seasonal heat storage and lateral heat transport. Sea ice also plays an important role in precipitation patterns and atmosphere circulation.

When ice is created from seawater, salt is rejected from the crystal structure. This results in the formation of brine, which adds salt to the water immediately under the ice and hence increases its density. Brine rejection is included in the model used in this study and plays an important role in the creation of the cold, saline water, with the required density to sink to the bottom in polar latitudes. On a global scale, the large spatial extent and high albedo of sea ice makes it a primary actor in the ice-albedo feedback.

Here, we use a simplified thermodynamic model based on the original work of *Semtner* [1976] and *Hibler* [1979]. This model calculates three quantities: Ice thickness (H_{tot}), areal distribution (A_i) and ice surface temperature (T_i). These quantities are explained below. A list of the ice model parameters is provided in Table 2.2.

In this model, the growth and decay of sea ice is derived from the energy fluxes computed at the upper and lower boundaries and is calculated as follows:

$$\frac{\partial H_{tot}}{\partial t} = \frac{\partial H_{top}}{\partial t} + \frac{\partial H_{bot}}{\partial t}. \quad (2.1.3.1)$$

The surface melt is given by the following:

$$\frac{\partial H_{top}}{\partial t} = \frac{1}{\rho_{surf} L_f} (Q_{cond} - Q_{top}) + E - P, \quad (2.1.3.2)$$

where ρ_{surf} is the density of the surface (ice or snow), L_f is the latent heat of fusion of ice, Q_{cond} is the conductive flux, Q_{top} is the heat flux coming from the atmosphere into the slab of ice and into the open water surface (both defined as positive downward and described below), E is the sublimation over ice or snow and P is precipitation as snow.

The conductive heat flux (Q_{cond}) is described as follows:

$$Q_{cond} = \frac{k_{eff}}{h_i + h_{snow}} (T_i - T_f), \quad (2.1.3.3)$$

where k_{eff} is the effective thermal conductivity of the surface component, h_i and h_{snow} are the ice and snow thicknesses respectively, T_i is the ice surface temperature and T_f is the freezing point temperature of salt water. If snow is present, k_{eff} may be modified to account for the insulating effect of the snow:

$$\frac{k_{eff}}{h_i + h_{snow}} = \frac{k_i k_{snow}}{h_i k_{snow} + k_i h_{snow}}, \quad (2.1.3.4)$$

where k_i and k_{snow} are the ice and snow conductivity respectively.

The heat flux from the atmosphere (Q_{top}) is computed for both the areal fraction of the grid cell covered by ice and the remaining open water area:

$$Q_{top} = A_i Q_{ii} + (1 - A_i) Q_{io}, \quad (2.1.3.5)$$

where Q_{ii} is described in Equation 2.1.3.6 and Q_{io} in 2.1.3.7.

The heat flux from the atmosphere into the slab of ice is given by:

$$Q_{ii} = Q_{ULW} + Q_{SH} + \rho_i L_s E - (1 - C_o) Q_{SW}, \quad (2.1.3.6)$$

where Q_{ULW} is given by equation (2.1.2.5), Q_{SH} by (2.1.2.6), L_s is the latent heat of sublimation and Q_{SW} is described in (2.1.2.3). The heat flux over an open water surface is calculated from:

$$Q_{io} = Q_{ULW} + Q_{SH} + \rho_o L_v E - (1 - C_o) Q_{SW}. \quad (2.1.3.7)$$

Hence, a balance of fluxes dictates surface melt. Surface fluxes, due to longwave and shortwave radiation forcing as well as sensible and latent heat exchanges, are balanced by the conduction of heat through the ice and the heat absorbed due to ice melt.

The basal ice melt is computed as follows:

$$\frac{\partial H_{bot}}{\partial t} = \frac{1}{\rho_i L_f} (Q_{bot} - Q_{cond}), \quad (2.1.3.8)$$

where ρ_i is the density of the ice and Q_{bot} is the heat flux from the ocean which is obtained by relaxing the ocean surface temperature back to freezing (T_f):

$$Q_{bot} = \frac{1}{\gamma} (T_f - T_o) \frac{\rho_o \Delta z C_{po}}{\Delta t} \quad (2.1.3.9)$$

where γ is a relaxation time scale of 10 days, T_f is defined by [UNESCO, 1983]:

$$T_f = -.0575S_0 + 1.710523 \times 10^{-3} S_0^{1.5} - 2.154996 \times 10^{-4} S_0^2, \quad (2.1.3.10)$$

Δz is the depth of the first ocean layer, C_{po} is the heat capacity of seawater, Δt is the model time step and S_0 is the sea surface salinity.

Ice areal distribution varies according to growth rates over ice covered and open water areas [Hibler, 1979]:

$$\frac{\partial A_i}{\partial t} = \begin{cases} (1 - A_i)(Q_{bot} - Q_{to})/H_o, & \text{if } Q_{to} < Q_{bot} \\ 0, & \text{otherwise} \end{cases} + \begin{cases} (A_i/2H_i) \frac{\partial H_i}{\partial t}, & \text{if } Q_t > Q_{bot} \\ 0, & \text{otherwise} \end{cases} \quad (2.1.3.11)$$

The first term is a simple parameterisation of the freezing effect. The fraction of open water ($1 - A_i$) is allowed to decay exponentially with a time constant of $(Q_{bot} - Q_{to})/H_o$. The second term of 2.1.3.11 describes the melting. The amount of melting is obtained by assuming that the ice has a uniform thickness distribution between 0 and $2h/A$, and that all of the ice melts uniformly. Setting the maximum areal fraction to 0.99 roughly parameterises leads. Snow saturation effects are also taken into account in this model. When snow accumulates and becomes heavy enough, the snow/ice interface gets displaced below the water line. The interface is given as follows:

$$z = h_i - \frac{\rho_{snow} h_{snow} + \rho_i h_i}{\rho_o}, \quad (2.1.3.12)$$

where ρ_{snow} is the density of snow and ρ_o is the ocean's density. This implies that when snow is present, approximately 90% of the ice is below the water line and $z = 0.1h_i$. If $z < 0$, then snow is converted to ice:

$$dh_{snow} = \frac{\rho_i}{\rho_{snow}} z \quad \text{and} \quad dh_i = -z. \quad (2.1.3.13)$$

This process will only occur if h_s is greater than approximately 1/3 of the ice thickness.

Table 2.2 Ice model parameters

| Parameter | Description | Value |
|-----------------|--------------------------------|------------------------------|
| ε_i | Ice emissivity | 0.96 |
| k_i | Ice conductivity | 2.17 gcm/s ³ K |
| L_f | Latent heat of fusion of ice | 3.34 x 10 ⁵ J/kg |
| L_s | Latent heat of ablation of ice | 2.835 x 10 ⁶ J/kg |
| ρ_i | Representative ice density | 913 kg/m ³ |

2.2 Boundary and initial conditions

Boundary and initial conditions for the experiments conducted in this study are summarised in Table 2.3 and are described below.

Table 2.3 Boundary and initial conditions for modelling experiments

| | |
|-----------------------------------|---|
| Land-sea distribution | <i>Late Ordovician</i> [Scotese and Golonka, 1992]; see Fig. 1.1/2.1 |
| Length of day (LOD) | <i>21.5 and 24 hours/day</i> [Berger et al., 1989] |
| Orbital parameters | <i>CSO, HSO, WFCS, CFWS*</i> |
| Atmospheric CO₂ | <i>1x, 10x, 14x, 18x pil (pil = 280 ppm)</i> |
| Solar luminosity | <i>Present day, -4.5%</i> [Endal and Sofia, 1981] |
| Topography | <i>None</i> |
| Wind fields | <i>Monthly averaged wind stress fields from GENESIS experiments</i> [Gibbs, 1996] |
| Albedo jump | <i>0.1, 0.2, 0.3</i> |

* Orbital parameters: Cold summer orbit (CSO), Hot summer orbit (HSO), Warm fall cool spring orbit (WFCS) and Cool fall warm spring orbit (CFWS).

2.2.1 Land-sea distribution

The land-sea distribution used in this study is derived from the one used by Crowley and Baum [1995]. Since there was no reconstruction available for the Late Ordovician, Crowley and Baum modified Scotese and Golonka's reconstruction of the Silurian (Wenlock epoch, 433 Ma)[Scotese and Golonka, 1992] by rotating the landmasses 5° to the north. Gondwana's position was then tangential to the South Pole. For this study, a linear interpolation was conducted on the original mask to correspond to the model's 3.75° zonal resolution and 1.8555° meridional resolution (Figure 2.1). From lack of geological evidence, a flat-bottom topography was used, with constant depth of 5.3625 km (the ocean model has 19 levels in the vertical).

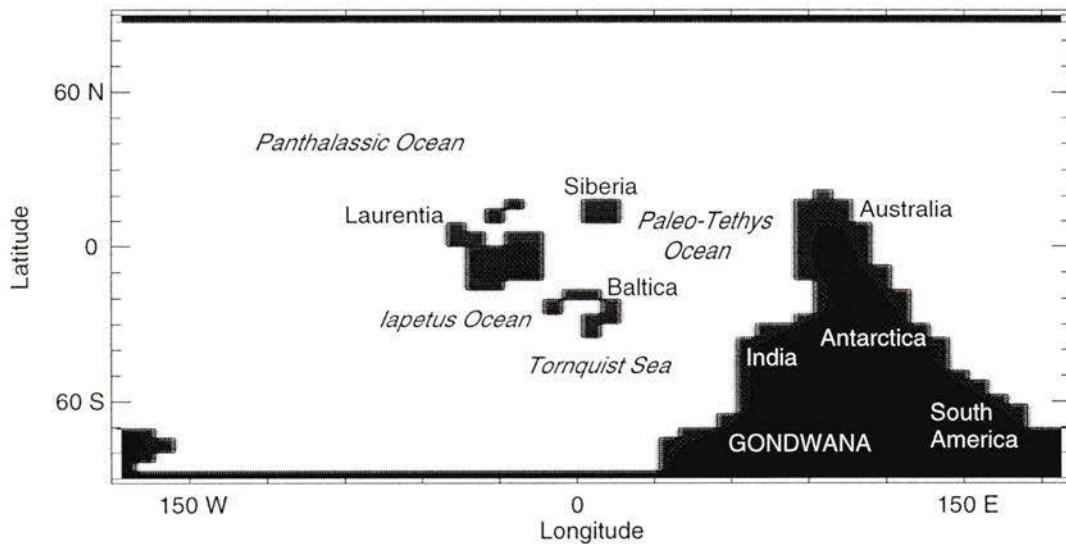


Figure 2.1 Land-sea distribution for Late Ordovician modelling experiments

2.2.2 Earth's rotation rate

Estimates of the rotational deceleration of the earth have been obtained from the paleontological analysis of stromatolites [Scrutton, 1978] and from tidal rhythmites (tidalites) [Sonett *et al.*, 1988; Sonett *et al.*, 1996; Williams *et al.*, 1997]. Tidal stresses due to the moon and sun induce deformations of the earth. Because of the delay in the earth's non-elastic response to the attraction of these two bodies, the tidal bulge is misaligned with the earth-moon axis [Berger *et al.*, 1989]. The transfer of angular momentum to the moon's orbit causes the major axis of the moon's orbit to increase at the expense of the earth's rotation rate. This has resulted in an appreciable increase in the length of day (LOD) through geologic time [Sonett *et al.*, 1988].

Jenkins *et al.* [1993] investigated the climatic influence of the LOD parameter through modelling experiments, using the NCAR Community Climate Model (CCM). For fast rotation rates, they found a larger equator-to-pole temperature gradient, which was apparently due to a less efficient meridional heat transport. In the present study, the

Early Silurian LOD estimate of 21.5 hours is used [Berger *et al.*, 1989]. To account for the decrease in the LOD, the rate of the earth's rotation (Ω) was increased from 7.29×10^{-5} radian/sec to 8.12×10^{-5} radian/sec. In addition, the wind stress field poleward of 10°N and 10°S is scaled as explained in Section 2.2.7.

2.2.3 Orbital parameters

The latitudinal and seasonal distributions of the solar energy received at the top of the atmosphere vary according to the solar constant, the eccentricity of the earth's orbit, the tilt of the earth's axis of rotation relative to the plane of its orbit (obliquity) and the position of the equinoxes in their precessional cycle (longitude of the perihelion). The variability of the solar constant through geologic time is addressed in Section 2.2.5. The influence of the remaining three orbital parameters are discussed below.

The eccentricity does not play a significant role in the total annual distribution of insolation. In fact, from a circular orbit (eccentricity = 0) to the most eccentric orbit (eccentricity = 0.06), the total annual insolation undergoes only a 0.18% change [Hartmann, 1994]. However, the ellipticity acts to change the temporal distribution of the total amount of radiation incident at the top of the atmosphere during an annual cycle. This produces changes of $\pm 3.5\%$ with the maximum coinciding with the perihelion. The time variation of the eccentricity has two dominant periodicities of about 100 KY and 400 KY years (1 KY = 1000 years). The most important term in the series expansion for eccentricity occurs at ~ 413 KY [Berger, 1976].

The obliquity (or tilt) dominates the climatic forcing at high latitudes and strongly influences the annual cycle of climate. Obliquity values range from 22.0° to 24.5° and vary within a 41 KY - period. An increase in obliquity enhances both the magnitude of the seasonal variation of insolation at high latitudes and the annual averaged insolation received at high latitudes. In addition, an increase in the obliquity leads to an increase in the summertime insolation at high latitudes (up to a 15% change) and a decrease in the wintertime insolation in midlatitudes. In short, the obliquity determines the annual mean equator-to-pole insolation gradient.

Precession refers to the wobbling of the earth's axis of rotation due to the gravitational pull that the sun and moon exert on the earth's equatorial bulge. This 'precession of the equinoxes' causes the four cardinal points (defined as the points on the earth's orbit at which seasons are initiated) to gradually shift around the orbital path. The precession cycle has an oscillation of ~22 KY. The magnitude of the precessional effect increases with increasing eccentricity. It is therefore convenient to use the precession parameter ($e \sin \Lambda$), which combines the climatic influence of the two parameters, to describe the insolation changes at high latitudes. The longitude of the perihelion is defined as the angle Λ , between the line from earth to the sun at vernal equinox (in Northern Hemisphere) and the line from the sun to perihelion. The precession parameter has little effects on the insolation at the poles and becomes increasingly large at the equator. In addition, the precession parameter, which is modulated by the eccentricity, divides the precession frequency into two dominant periods, ~19 KY and ~23 KY.

The three orbital parameters combined can induce changes in seasonal insolation by as much as 30% in high latitudes. Climatic extremes are achieved when the winter solstice ($\Lambda=90^\circ$) or the summer solstice ($\Lambda=270^\circ$) take place at the perihelion. Since the aim of this study is to assess the potential for a glaciation on Gondwana, the following discussion focuses on orbital configurations, which most affect the Southern Hemisphere. The reverse of the argument presented here would apply for reproducing climatic extremes in the Northern Hemisphere.

It was first pointed out by *Köppen* [1924] and later supported by Milandovitch's *Theory of Ice Ages* that a decrease in summer insolation in polar latitudes plays a critical role in the creation of ice sheets. The reasoning for this stems from the idea that winter temperatures are presumably always cold enough for precipitation to fall as snow. However, a high insolation input during the summer season can prevent the development of permanent glaciers by initiating a too vigorous melt season. A reduction in the summertime insolation would therefore support summer temperatures cool enough to sustain a positive annual snow budget. In addition, the persistence of snow throughout

the year would establish a positive-feedback cooling through ice/albedo effects and would promote a further expansion of the snow cover.

An investigation of the sensitivity of the coupled climate model to orbital parameters is conducted through a series of modelling experiments using two extreme and two intermediate configurations. These experiments are referred to in the text as the “hot summer orbit” (HSO), the “cold summer orbit” (CSO), the “warm fall-cool spring orbit” (WFCS) and the “cool fall-warm spring orbit” (CFWS). The orbital parameters used in each experiment are listed in Table 2.4 and a sketch of these configurations is provided in Figure 2.2a.

Table 2.4 Orbital parameters used in modelling experiments

| <i>Orbital parameters</i> | <i>Obliquity</i> | <i>Eccentricity</i> | <i>Longitude of perihelion</i> |
|---------------------------|------------------|---------------------|--------------------------------|
| Present | 23.47 | 0.0167 | 282 |
| HSO (SH) | 24.5 | 0.06 | 270 |
| CSO (SH) | 22.0 | 0.06 | 90 |
| WFCS (SH) | 22.0 | 0.06 | 0 |
| CFWS (SH) | 22.0 | 0.06 | 180 |

The HSO experiment has an obliquity of 24.5° to maximise insolation at high latitudes and a longitude of perihelion of 270° in order for the Southern Hemisphere summer to coincide with the perihelion. As shown in Figure 2.2b, the Southern Hemisphere experiences short and hot summers while winters are long and cold, since they occur when the earth is at its furthest distance from the sun (aphelion). This configuration promotes an intense melt season during the summer and produces winter temperatures too cold to hold the necessary moisture for a high snowfall.

The CSO experiment has an obliquity of 22.0° and a longitude of perihelion of 90° . This configuration minimises insolation input at high latitudes and forces the Southern Hemisphere winter solstice, which is the time when the South Pole is tipped the farthest

away from the sun, to occur at perihelion. This results in long, cool summers and short, mild winters, as indicated in Figure 2.2b. The CSO arrangement is regarded as ideal for glacial inception and maintenance [*Hays et al.*, 1976; *Imbrie and Imbrie*, 1979]. The present-day configuration is quite similar to the HSO configuration of the Southern Hemisphere (or CSO for Northern Hemisphere) (Figure 2.2a).

The WFCS and CFWS configurations are intermediate arrangements of longitude of perihelion, while the obliquity is kept to a minimum of 22.0° to minimise solar insolation receipt at high latitudes. The WFCS experiment has a longitude of perihelion of 0° . For this configuration, the Southern Hemisphere autumnal equinox coincides with the perihelion. This gives rise to a brief, warm fall and a long, cool spring. The CFWS orbit has a longitude of perihelion of 180° . Hence, the Southern Hemisphere vernal equinox coincides with the perihelion. This configuration supports short, warm spring seasons and long, cool fall seasons.

According to calculations conducted by *Berger et al.* [1989], changes in the earth-moon distance, the earth's rotation rate and its moment of inertia during the Phanerozoic could have induced $\sim 10\%$ variations in precessional periods and $\sim 20\%$ variations in obliquity periods. However, the magnitude of the change in forcing is unknown. Hence, the two extreme orbital configurations found for the Pleistocene are used in this study [*Berger*, 1978].

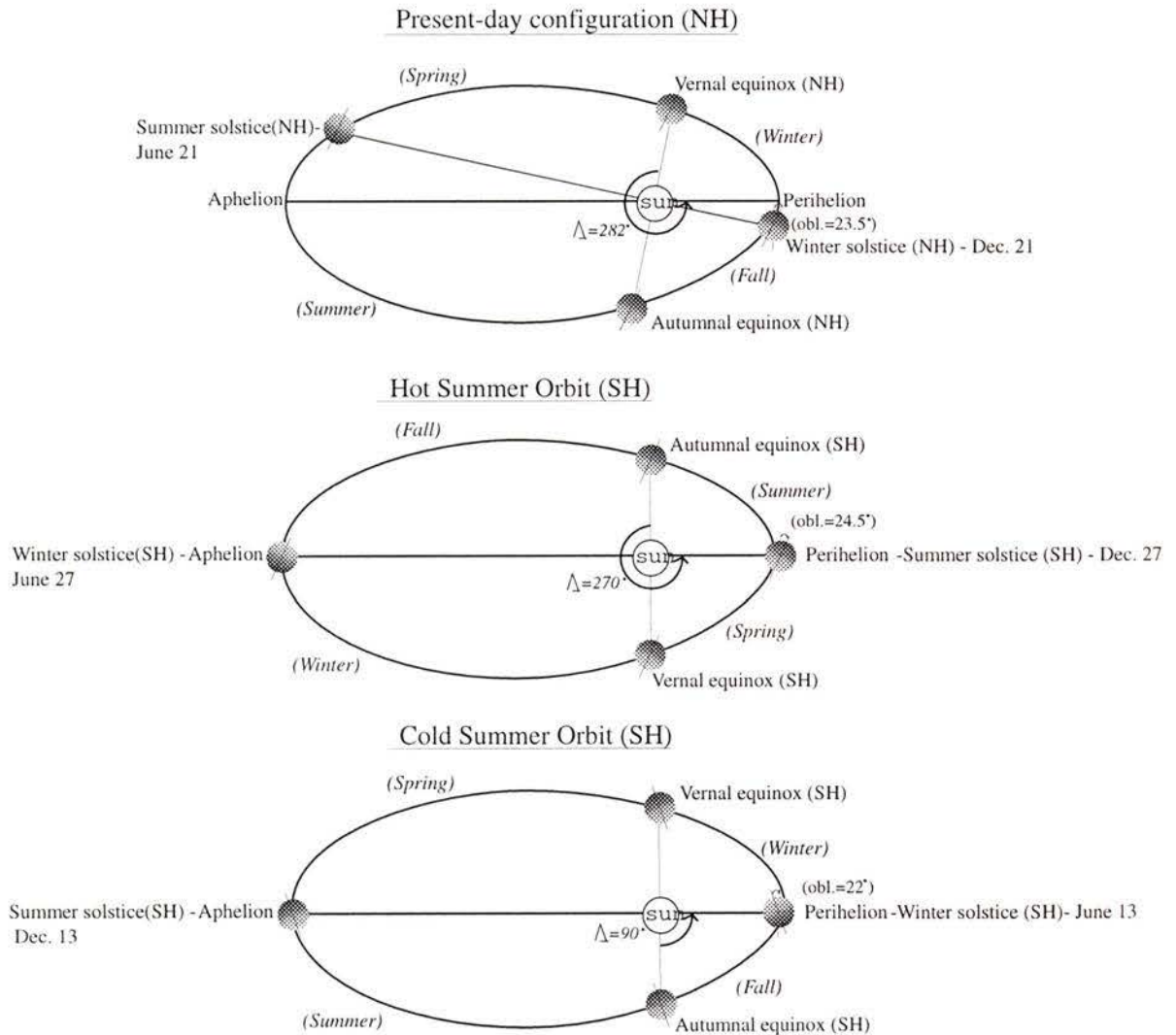


Figure 2.2 a) Sketch of the orbital configurations used in the modelling experiments. Longitude of the perihelion (Λ) is relative to the vernal equinox in the Northern Hemisphere. Eccentricity of orbit is not to scale.

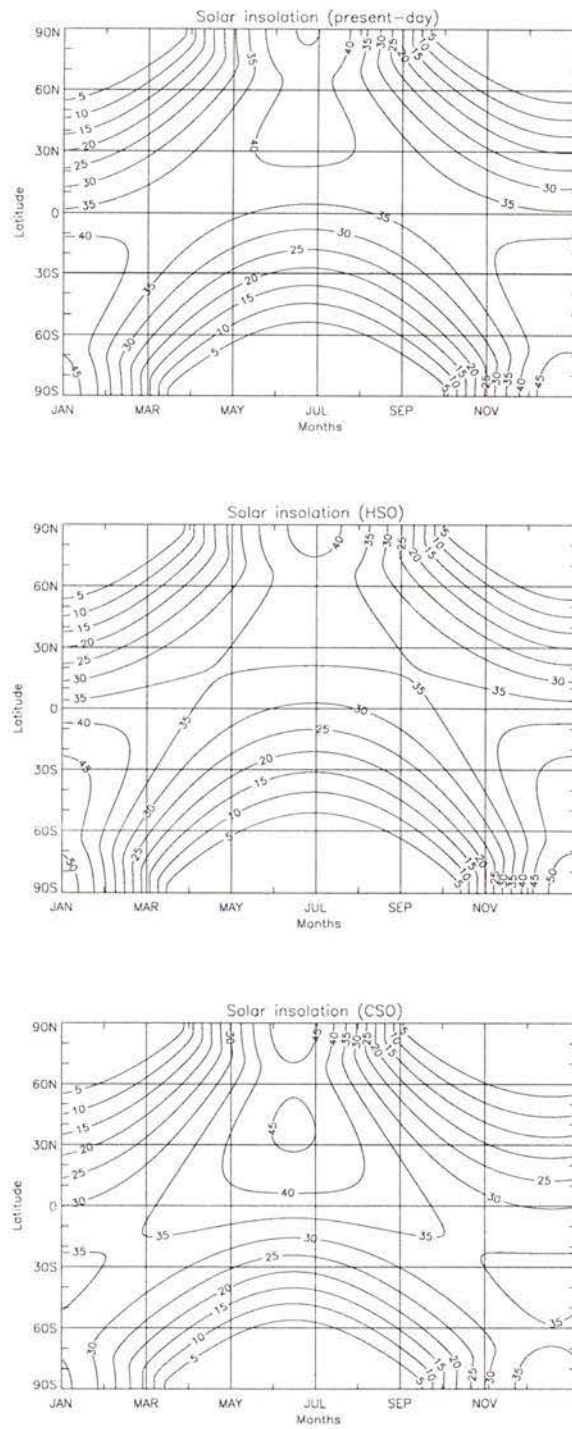


Figure 2.2 b) Daily average solar insolation incident on a unit horizontal surface at the top of the atmosphere as a function of latitude and time of year in 10^6 Jm^{-2} ($1 \times 10^6 \text{ Jm}^{-2}$ for one day $\approx 11.6 \text{ Wm}^{-2}$). Top) Present-day orbital forcing Middle and bottom) HSO and CSO for Southern Hemisphere.

2.2.4 Atmospheric CO₂

Estimates of Late Ordovician atmospheric CO₂ levels were discussed in Section 1.8.1. For this study, experiments are conducted using CO₂ values of 10x, 14x and 18x pre-industrial levels (p_{il} ≅ 280 ppm). These values are representative of the range of CO₂ estimates. The CO₂ radiative forcing is calculated as follows [IPCC, 1996]:

$$F = 5.77 \times 10^3 \ln\left(\frac{CO_2}{350.0}\right). \quad (2.2.4.1)$$

This logarithmic relationship reflects the saturation of different CO₂ absorption bands at higher concentrations and gives a radiative forcing of 4 W/m² for a doubling of CO₂ [Ramanathan *et al.*, 1987] and a climate sensitivity of 0.75°CW⁻¹m² [Weaver *et al.*, 1998].

2.2.5 Solar luminosity

Studies on solar evolution have suggested a 25-40% increase in luminosity over the earth's history [Newman and Rood, 1977; Endal and Sofia, 1981; Bahcall, 1988]. Late Ordovician estimates for solar luminosity imply a 3.5-5.0% decrease. These estimates depend on the definition of the original components of the sun's core [Crowley and Baum, 1991]. Here, I use a 4.5% decrease as suggested by Crowley and Baum [1995] and hence a solar constant value of 1.306 x 10³ Wm⁻². The sensitivity of the coupled model to changes in the solar forcing is addressed in Section 3.1.1.

2.2.6 Topography

There are currently no detailed topographical maps of the Ordovician Period. Hence, a flat topography on the continents is prescribed for the modelling experiments. This is probably a realistic first approximation since during the Middle Ordovician, extensive epicontinental seas were covering parts of Gondwana, Laurentia, Baltica and Siberia. In addition, because river drainage basins are unknown for this time period, I define a river mask in which all precipitation falling on land is equally redistributed to all

coastal land points. As demonstrated for Last Glacial Maximum modelling experiments, the specific location of major fresh-water inputs may, in some instances, play a determinant role in the stability of the ocean's circulation especially during glacial-interglacial events [Weaver *et al.*, 1998]. This issue is not addressed in this thesis as snowmelt derived from the continents is also redistributed to all coastal land points.

2.2.7 Wind fields

For this study, I use monthly averaged wind fields previously generated with the GENESIS AGCM [Gibbs, 1996]. The wind fields were obtained using the following boundary conditions: Late Ordovician paleogeography [Crowley and Baum, 1995], 10x or 18x atmospheric CO₂ levels, CSO, -4.5% solar luminosity and present-day length of day. For a complete description of the global climate model GENESIS, see Thompson and Pollard [1994]. From the geostrophic wind equation, the wind speed fields were scaled everywhere outside 10°N and 10°S to account for a shorter length of day (21.5 hours), as follows:

$$(u_s, v_s) = \frac{f_{pd}}{f_o} (u_u, v_u) = 0.898 (u_u, v_u), \quad (2.2.7.1)$$

where u_s and v_s are the scaled components of the wind speed whereas u_u and v_u are the unscaled components of the wind speed, f_{pd} and f_o are the present-day and Ordovician Coriolis parameter. The annually averaged wind stress field used in the 10x CO₂ experiments is shown in Figure 2.3.

because there is a large difference in albedo between fresh and old snow (0.75-0.95) [Broccoli and Manabe, 1987].

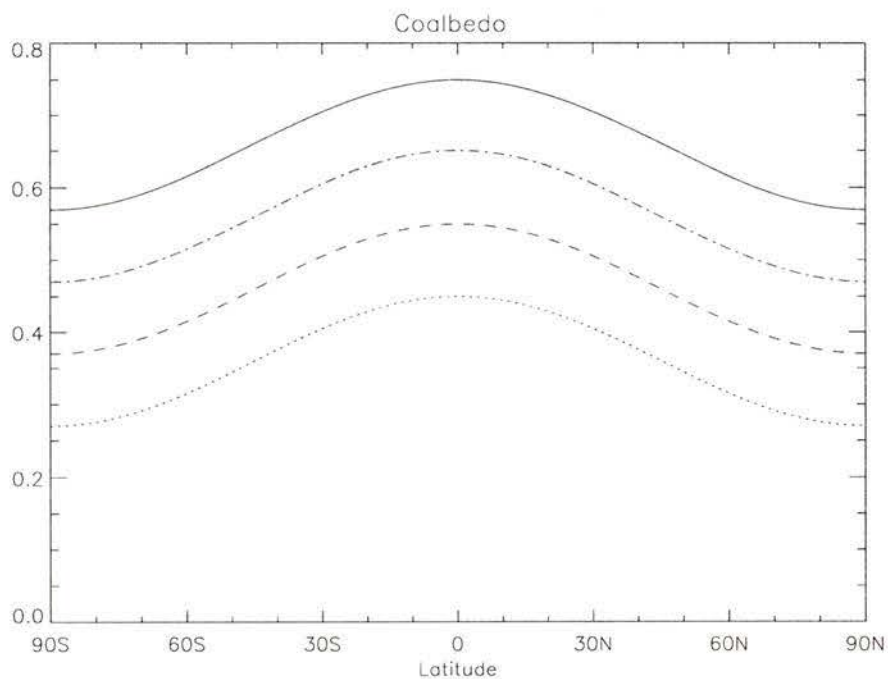


Figure 2.4 Latitudinal profile of the coalbedo [North *et al.*, 1983]. Solid line is the planetary coalbedo used in the model; the other three lines represent the coalbedo of the ice/snow surface for albedo jumps of 0.1 (dash-dotted), 0.2 (dashed) and 0.3 (dotted)

2.2.9 Initial conditions

All experiments are conducted from rest. Initial conditions for the ocean model include a simplified SST distribution from Levitus [1994] and global constant salinity. For the atmosphere model, initial temperature is 0°C everywhere and the atmosphere contains no moisture.

3. Late Ordovician modelling results

The respective roles of atmospheric CO₂ (Section 3.1), the presence of ice sheets via ice-snow albedo feedbacks (Section 3.2) and of orbital parameters (Section 3.3) in the Late Ordovician climate are examined through a series of sensitivity experiments. In addition, a control experiment is conducted with the following boundary conditions: Ordovician geography, 10x CO₂, cool fall-warm spring orbit (CFWS), -4.5% solar luminosity, an albedo jump of 0.1 and a length of day (LOD) of 21.5 hours. The orbital parameters used in this sensitivity describe a mid-point configuration between the HSO and CSO. We argue that this setting provides an appropriate representation of the average orbital forcing that would occur on timescales representative of the Late Ordovician glaciation. Key findings are summarised in Table 3.2. An analysis of the temperature response, effects on the hydrological cycle and on the meridional overturning streamfunction as well as the glacial response is provided for each sensitivity.

3.1 Model sensitivity to atmospheric CO₂

The sensitivity of the coupled model to changes in atmospheric CO₂ levels within the Late Ordovician context is investigated for concentrations 10x, 14x and 18x greater than pre-industrial levels (pil \cong 280 ppm). These values span the range of uncertainty associated with Berner's geochemical estimates [Berner, 1994]. The three sensitivities (control (10x), 14x_cfws_aj01 and 18x_cfws_aj01) are started from rest and integrated 3000 years to reach equilibrium. Because the focus of this section is the sensitivity to atmospheric CO₂, the control run will be referred to as 10x (strictly in this section), whereas the other two experiments will be called 14x and 18x. The boundary conditions for all three runs are the following: Ordovician geography, cool fall-warm spring orbit (CFWS), -4.5% solar luminosity, albedo jump of 0.1 and LOD of 21.5 hours. Results are summarised in Table 3.2 and are contextualised in the following sections.

3.1.1 Temperature response

Figure 3.1 shows the spatial distribution of the annual mean surface air temperature response to changes in atmospheric CO₂ (18x-10x). It is apparent from the figure that atmospheric temperatures are quite sensitive to variations in CO₂ forcing. The minimum warming is found in the Tropics (2.5°C) whereas the maximum warming occurs over the Gondwana landmass (5°C) and in polar latitudes of both hemispheres. The amplification of the CO₂ radiative forcing at high latitudes is due to snow and sea ice albedo feedbacks. The presence of a large zonal belt of increased atmospheric temperatures bordering the south coast of Gondwana is attributed to the contraction of the Southern Hemisphere sea ice cover. Both the insulating effect of sea ice and the albedo feedbacks associated with its reflective surface contribute in the dampening of the CO₂ forcing at low concentrations. A similar response is visible in the Northern Hemisphere along the ice edge. The large temperature increase over Gondwana is connected to snow-albedo-temperature feedbacks.

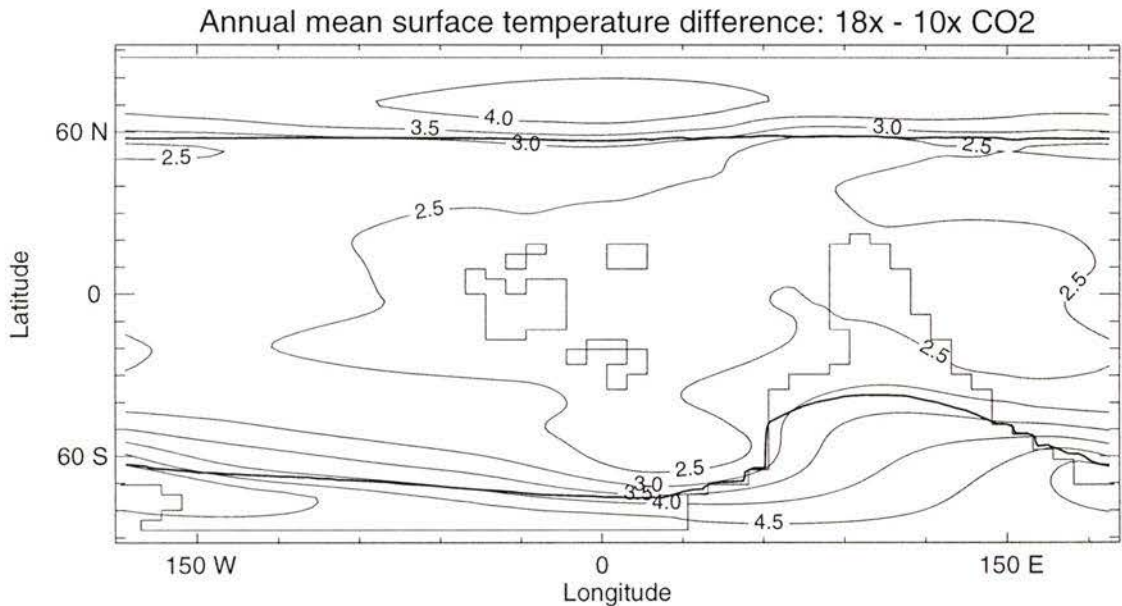


Figure 3.1 Annual mean surface air temperature (°C) difference (18x – 10x CO₂). Contour intervals are 0.5°C. Heavy line over the ocean represents the maximum sea-ice extent whereas over Gondwana, it represents the location of the –10.0°C contour or the snow extent (whichever extends the furthest to low latitudes) for the 10x CO₂ experiment. The ice edge delimits the maximum snow/sea ice covered area present during a one-year period.

The influence of increased atmospheric CO₂ on seasonality is investigated through a latitude vs. time distribution of the difference in atmospheric temperature between the 18x and 10x experiments, and is shown in Figure 3.2. The coupled model's seasonal cycle is driven by changes in solar insolation and by monthly averaged winds. It is apparent from Figure 3.2 that the atmospheric thermal response is accentuated in the polar regions during the winter season when ice albedo feedback difference would be greatest. In the Southern Hemisphere, maximum warming is achieved in mid-August, which represents the end of the austral winter and also when the ice albedo difference is largest.

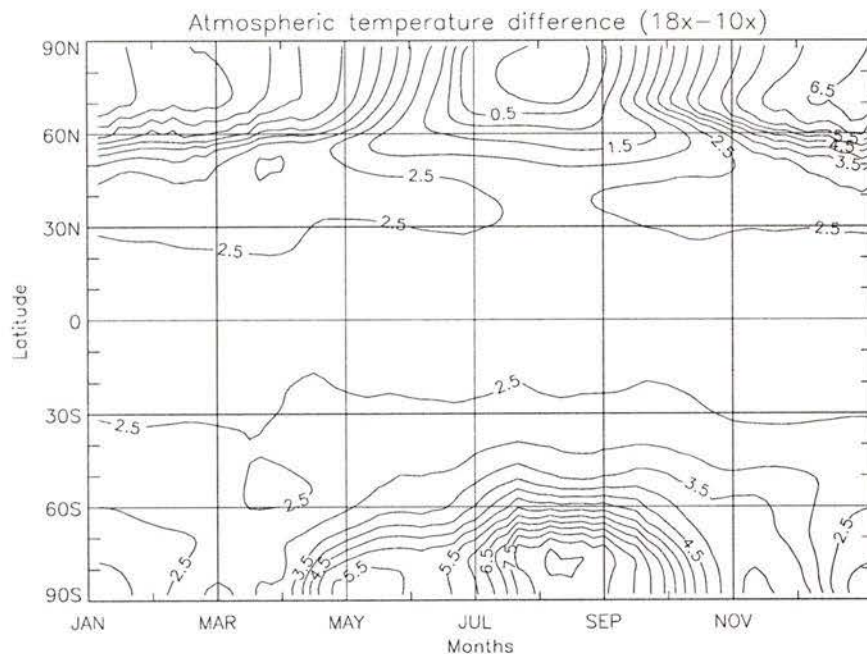


Figure 3.2 Latitude vs. time distribution of the difference in zonal mean surface air temperature (°C) between the 18x and 10x experiments. Contour intervals are 0.5°C.

The annual global mean atmospheric surface temperature increased by 2.74°C between the 10x and 18x experiments, whereas the globally averaged ocean temperature warmed by 0.35°C (Table 3.2). The modelled global ocean temperature is substantially colder than present-day ocean for all experiments. In fact, the globally averaged ocean temperature for the 10x experiment is 1.4°C, which is 2.4°C cooler than the estimate for the present-day ocean calculated by *Levitus and Boyer* [1994]. This is largely due to the presence of an extensive sea ice cover in the northern high latitudes. The highly

reflective surface of sea ice inhibits solar radiation from reaching the ocean's surface, thereby contributing to the global cooling observed.

To assess the climate sensitivity of the coupled model given the boundary conditions characteristic of the Late Ordovician, I conducted an additional experiment (*ordo_geog*) with the following boundary conditions: Ordovician geography, 1x CO₂ concentrations, present-day orbital parameters, solar forcing, albedo jump and LOD. Table 3.1 shows that the negative radiative forcing due to the decreased solar luminosity only partially counteracts the positive forcing due to the CO₂ increase (see Section 2.2.4). The key results of the *ordo_geog* experiment are summarised in Table 3.2.

Table 3.1 Climate sensitivity parameters

| CO ₂ (ppm) relative to pil | ΔForcing (W/m ²) | | Net forcing (W/m ²) | ΔT _a (°C) relative to <i>ordo_geog</i> | Climate sensitivity (°C W ⁻¹ m ²) |
|---|------------------------------|-----------------|--|---|--|
| | ΔCO ₂ | -4.5% <i>sl</i> | | | |
| 280 (1x) | -1.29 | -10.84 | -12.13 | --- | --- |
| 2800 (10x) | 11.99 | -10.84 | 1.15 | 2.10 | 0.158 |
| 3920 (14x) | 13.94 | -10.84 | 3.10 | 3.76 | 0.247 |
| 5040 (18x) | 15.39 | -10.84 | 4.55 | 4.84 | 0.290 |

Table 3.2 Late Ordovician modelling results

| <i>Experiments</i> | <i>Int.</i> | <i>To</i> | <i>Ta</i> | <i>Vi(SH)</i> | <i>Ai(SH)</i> | <i>Ai(NH)</i> | <i>AsG(SH)</i> | <i>A>0.1</i> | <i>A>0.01</i> |
|----------------------|-------------|-----------|-----------|---------------|---------------|---------------|----------------|-----------------|------------------|
| Control (10x) | 3000 | 1.4 | 12.6 | 470 | 0.93 | 20.4 | 0.00 | 0.00 | 0.00 |
| 10x_wfcs_aj01 | 4000 | 1.4 | 12.6 | 2530 | 2.83 | 16.2 | 0.17 | 0.11 | 0.12 |
| 10x_wfcs_aj02 | 2100 | 1.1 | 10.6 | 73000 | 7.26 | 23.9 | 4.13 | 1.45 | 3.88 |
| 10x_wfcs_aj03 | 2100 | 0.6 | 6.7 | 640500 | 17.70 | 59.4 | 14.5 | 13.70 | 14.30 |
| 10x_cso_aj01 | 3000 | 1.4 | 12.6 | 2645 | 2.90 | 17.3 | 0.54 | 0.41 | 0.42 |
| 10x_hso_aj01 | 3000 | 1.4 | 12.3 | 139 | 0.65 | 21.4 | 0.00 | 0.00 | 0.00 |
| 14x_cfws_aj01 | 3000 | 1.7 | 14.3 | 0 | 0.00 | 18.6 | 0.00 | 0.00 | 0.00 |
| 14x_wfcs_aj01 | 4000 | 1.7 | 14.5 | 260 | 0.65 | 14.5 | 0.00 | 0.00 | 0.00 |
| 18x_cfws_aj01 | 3000 | 1.7 | 15.3 | 0 | 0.00 | 16.2 | 0.00 | 0.00 | 0.00 |
| 18x_wfcs_aj01 | 4000 | 1.8 | 15.4 | 210 | 0.39 | 12.3 | 0.00 | 0.00 | 0.00 |
| Ordo_geog | 4000 | 1.2 | 10.5 | 2900 | 1.45 | 45.7 | --- | --- | --- |

The name of each sensitivity experiment has three components: the first refers to the atmospheric CO₂ concentration (relative to 280 ppm) used in the experiment, the second is the orbital configuration (see Table 2.4) and the third represents the magnitude of the albedo jump. Control (10x) is equivalent to 10x_cfws_aj01. *Int.* represents the integration time (years). *T_a* is the annual mean surface air temperature (°C), *T_o* is the depth-averaged global ocean temperature(°C), *V_i(SH)* represents the January mean sea ice volume (km³), *A_{i,s}* are the January averaged sea ice area (SH) and July averaged sea ice area (NH) (x10⁶km²), *A_{s,G}* is the January averaged snow area on Gondwana and *A>0.1m* and *A>0.01m* are snow areas on Gondwana with thickness greater than 0.1 and 0.01m respectively.

January and July sea surface temperatures (SST) and surface atmospheric temperatures (SAT) for the 10x and 18x experiments are shown in Figures 3.3 and 3.4 respectively. SATs over Gondwana remain above freezing during the month of January in all experiments.

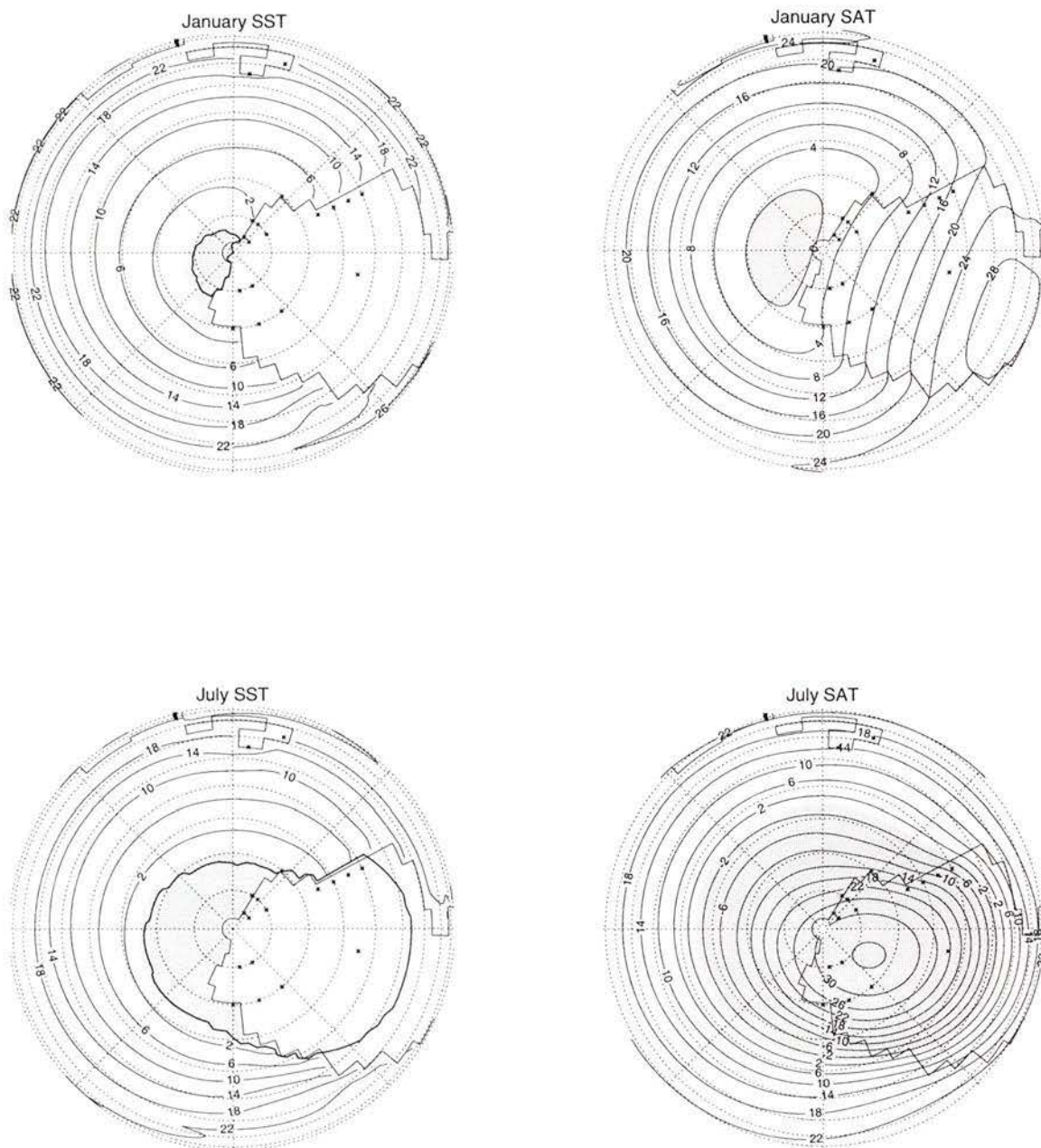


Figure 3.3 Modelled January and July SST and SAT for 10x experiment (south polar orthographic projection). Asterisks represent an approximate distribution of glacial deposits [Paris *et al.*, 1995]. Contour intervals are 4°C. Heavy line over the ocean for SST graphs represents the maximum sea-ice extent whereas over Gondwana, it represents the location of the -10.0°C contour or the snow extent (whichever extends the furthest to low latitudes). The ice edge delimits the maximum snow/sea ice covered area present during the months of January or July.

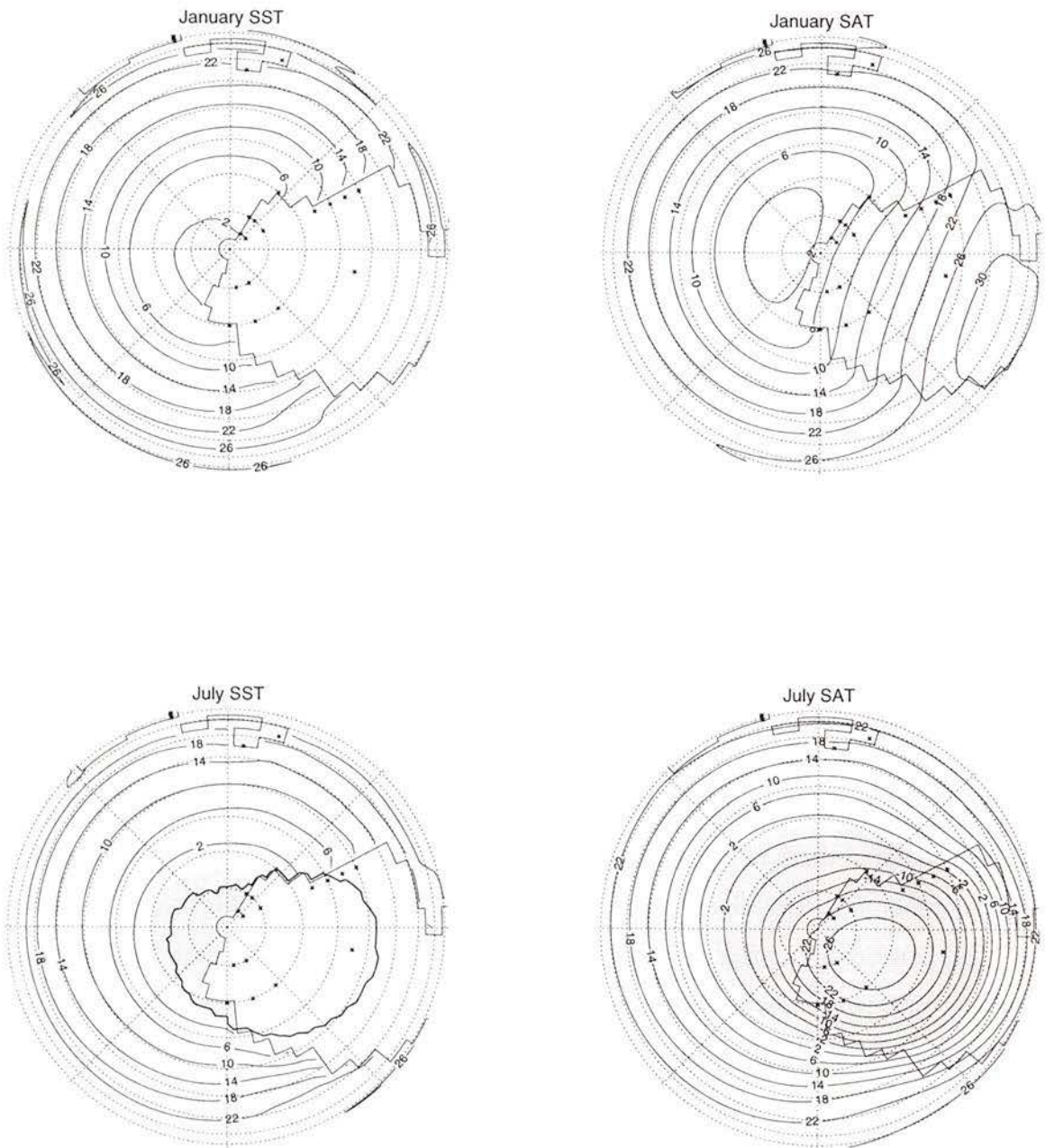


Figure 3.4 Modelled January and July SST and SAT for 18x experiment (south polar orthographic projection). Asterisks represent an approximate distribution of glacial deposits [Paris *et al.*, 1995]. Contour intervals are 4°C. Heavy line over the ocean for SST graphs represents the maximum sea-ice extent whereas over Gondwana, it represents the location of the -10.0°C contour or the snow extent (whichever extends the furthest to low latitudes). The ice edge delimits the maximum snow/sea ice covered area present during the months of January or July.

The spatial distribution of atmospheric freezing temperatures during the month of July covers glacial deposits found on Gondwana, even in the 18x experiment. A large area of very cold temperatures in high southern latitudes is present in the 10x experiment

(down to -34.0°C over the African continent). SSTs cooler than -1.8°C , as depicted by the ice edge, are located in the vicinity of the South Pole and coincide with the majority of glacial deposits. A permanent sea ice cover persists in the 10x scenario but not in the 14x and 18x scenarios (Table 3.2).

3.1.2 Hydrological response

Maximum precipitation rates occur within the equatorial belt (top graph of Figure 3.5). A pronounced precipitation maxima of 1.96 m/yr is predicted over coastal Antarctica at $\sim 40^{\circ}\text{S}$. Precipitation appears negligible over most of central Gondwana for all experiments. The low precipitation over the Gondwanan landmass, due to the simple parameterisation of diffusive moisture transport, is likely to be an underestimate. This precipitation, which falls as snow when atmospheric temperatures are colder than -10.0°C , would play a critical role in the initiation of a continental glaciation. In polar latitudes, precipitation rates are low due to the low moisture content of the polar air.

The intensity of the hydrological cycle shows a 3.4% increase between the 10x and 18x experiments. Increased precipitation in polar latitudes of both hemispheres, as indicated in the middle graph of Figure 3.5, which shows the difference in global annual mean precipitation patterns between the 10x and 18x experiments, is associated with the contraction of the sea ice cover. A decrease in the sea ice extent allows for a strong oceanic feedback. As sea ice no longer insulates the ocean's surface, the warm SSTs can contribute in the warming of the overlying SATs. It is also apparent from the middle graph of Figure 3.5 that precipitation rates in the subtropical convection belts are not considerably affected by the increase in atmospheric CO_2 . In fact, the figure shows a small decrease in precipitation in the proximity of Laurentia and Baltica.

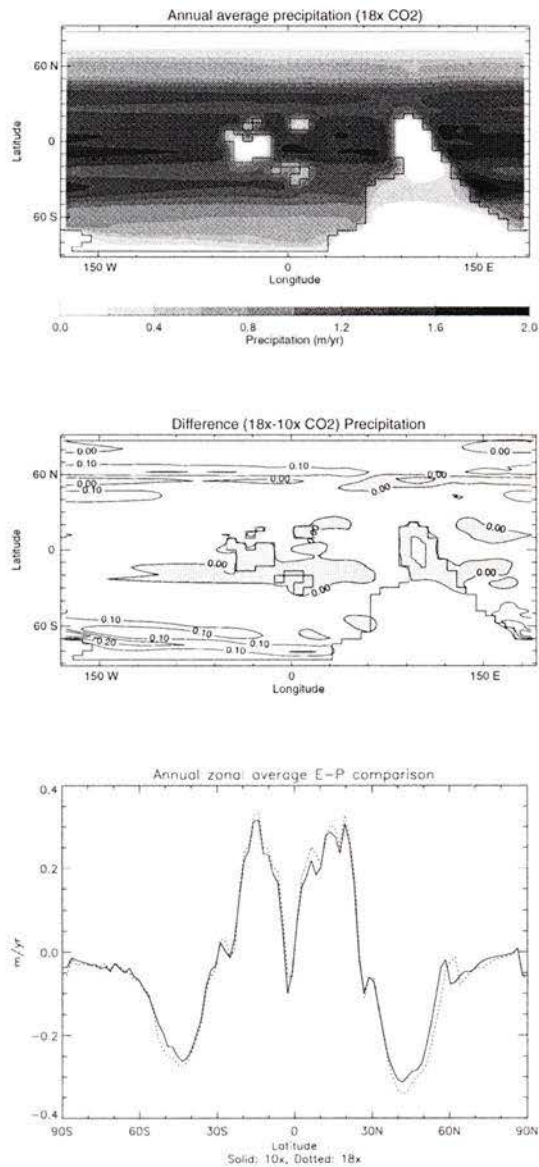


Figure 3.5 Top) Annual average global precipitation patterns (m/yr) for 18x experiment. Contour intervals represent 0.2 m/yr. Middle) Annual mean precipitation (m/yr) difference (18x – 10x CO₂). Shading represents negative values and contour intervals are 0.1m/yr. Bottom) Annual mean zonal average evaporation – precipitation (E-P) comparison (m/yr) between 10x (solid) and 18x (dotted) CO₂.

The bottom graph of Figure 3.5 shows a comparison of the annual mean zonally averaged evaporation – precipitation (E-P) profiles between the 18x and 10x experiments. It is apparent from the figure that the freshwater flux at high latitudes is increased with higher CO₂ levels, especially at mid-latitudes. The freshwater flux for the 18x experiment increased by ~0.01 m/yr (poleward of 45°S) relative to the 10x experiment. As shown in Figure 3.1, the warming of the surface air temperature was ~2°C at equatorial latitudes

and $\sim 2.5^{\circ}\text{C}$ at subtropical latitudes. The E-P graph shows that at equatorial and subtropical latitudes, evaporation rates increased while precipitation rates decreased at these latitudes (middle graph) with increasing CO_2 . This is in agreement with the Clausius-Clapeyron equation which states that the saturation vapour pressure increases exponentially with increasing temperature.

3.1.3 Meridional overturning response

The sensitivity of the meridional overturning streamfunction to increases in CO_2 is apparent in Figure 3.6, which shows the annual mean global overturning streamfunction for the 10x and 18x experiments as well as the difference between the two experiments (18x – 10x). The bottom figure reveals that the increase in atmospheric CO_2 produced a poleward shift of the deep-water formation region. This is due to the retreat of the ice edge with increasing CO_2 . The total amount of deep water exported to the northern Panthalassic ocean above 3,000 m did not change considerably between the 10x and 18x experiments ($\sim 19 \text{ Sv}$ for 10x and $\sim 18 \text{ Sv}$ for 18x).

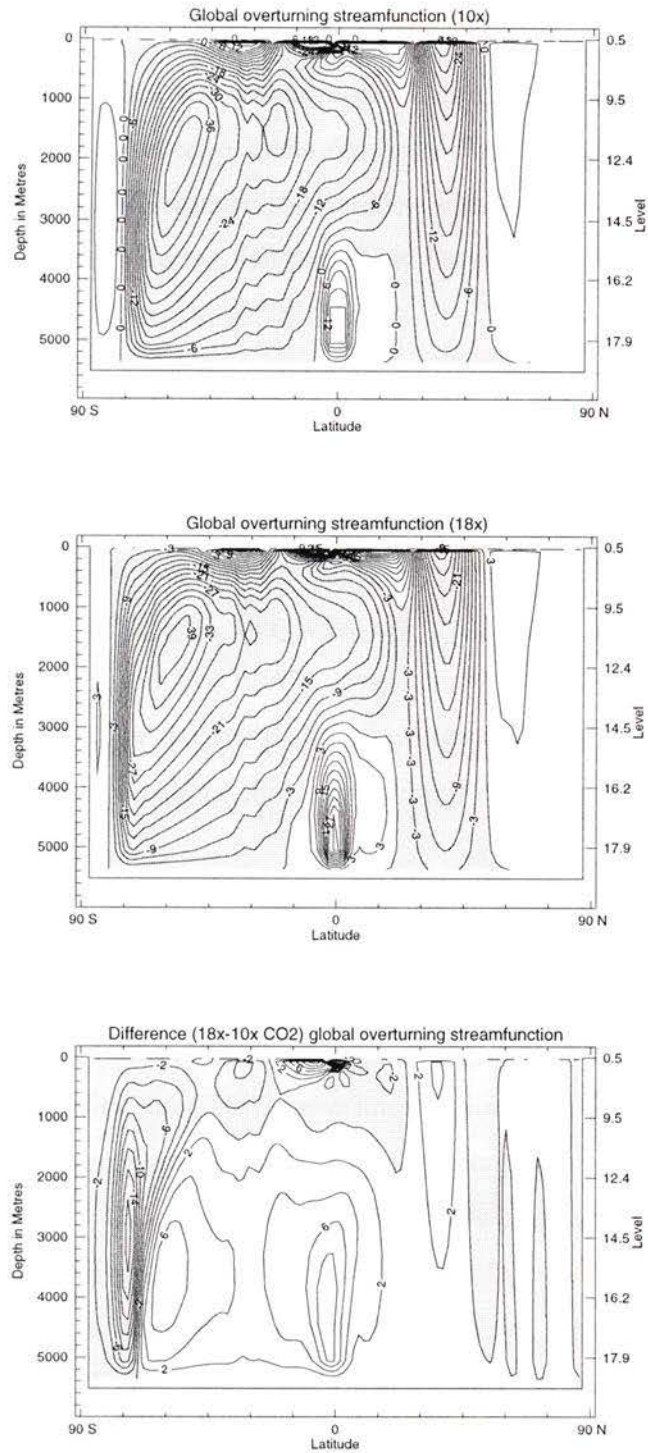


Figure 3.6 Global overturning streamfunction for 10x experiment (top), 18x experiment (middle) and difference (18x-10x CO₂) global overturning streamfunction (bottom) (in Sv; 1 Sv = $10^6 \text{m}^3 \text{s}^{-1}$). Maximum difference of -41 Sv at ocean surface layer north of equator. Contour intervals are 3 Sv for top and middle graphs and 2 Sv for bottom graph. Shading represents regions of negative value.

3.1.4 Glacial response

The glacial response relative to changes in CO₂ concentrations is assessed through the evaluation of the January average snow cover on Gondwana and sea ice extent. The month of January is analysed because it coincides with the end of the austral summer. We assume that snow present during that period has survived through the melt season and is likely to become part of a permanent ice sheet.

January snow cover on Gondwana did not survive for any of the CFWS CO₂ sensitivity experiments conducted in this study (Table 3.2). However, a parallel set of CO₂ sensitivity experiments were performed using identical boundary conditions except for the orbital forcing which was a warm fall-cool spring (WFCS) configuration (Table 3.2: 10x_wfcs_aj01, 14x_wfcs_aj01, 18x_wfcs_aj01). Although a permanent snow cover did not subsist for the 14x and 18x WFCS experiments, the 10x_wfcs_aj01 did have a small area of snow ($0.17 \times 10^6 \text{km}^2$) which survived in the southern latitudes of Gondwana. The respective role of these two orbital configurations on the climate is discussed in Section 4.2.3.

Estimates of Southern Hemisphere sea ice extent represent January averages whereas for the Northern Hemisphere, estimates represent July averages as they coincide with the end of the austral and boreal summer. Sea ice extent shows a strong dependence on atmospheric CO₂ levels. For the CFWS experiments, Southern Hemisphere sea ice only survived for the 10x scenario with a January average area of $0.93 \times 10^6 \text{km}^2$ (Table 3.2). However, for the WFCS CO₂ sensitivity experiments, January sea ice cover in the Southern Hemisphere survived for the 10x ($2.83 \times 10^6 \text{km}^2$), 14x ($0.65 \times 10^6 \text{km}^2$) and 18x ($0.39 \times 10^6 \text{km}^2$) cases. A large Northern Hemisphere sea ice extent is present in all experiments (CFWS and WFCS) and reaches a maximum extent of $23.6 \times 10^6 \text{km}^2$ in the 10x_cfws experiment (Table 3.2). This sea ice cover extends down to $\sim 60^\circ \text{N}$. In comparison, at 21 KY before present, the estimated Antarctic sea ice cover is $\sim 30 \times 10^6 \text{km}^2$ [Cooke and Hays, 1982].

3.2 Model sensitivity to albedo jump

Sensitivity of the coupled model to changes in the albedo jump between snow/ice covered surfaces and bare surfaces is tested for values of 0.1 (standard), 0.2 and 0.3 (Figure 2.4) [North *et al.*, 1983; Graves *et al.*, 1993]. The three experiments were started from rest and integrated at least 2000 years to reach equilibrium (10x_wfcs_aj01, 10x_wfcs_aj02 and 10x_wfcs_aj03). Boundary conditions for these experiments were 10x CO₂ concentrations, WFCS forcing, -4.5% solar luminosity and a LOD of 21.5 hours and will be referred to in the text as aj01, aj02 and aj03.

3.2.1 Temperature response

Results show a strong response of the climate model to changes in the albedo jump. The key findings are summarised in Table 3.2. The annual global mean ocean temperature decreased by 0.8°C and the surface air temperature (SAT) decreased by 5.9°C between the aj01 and aj03 experiments.

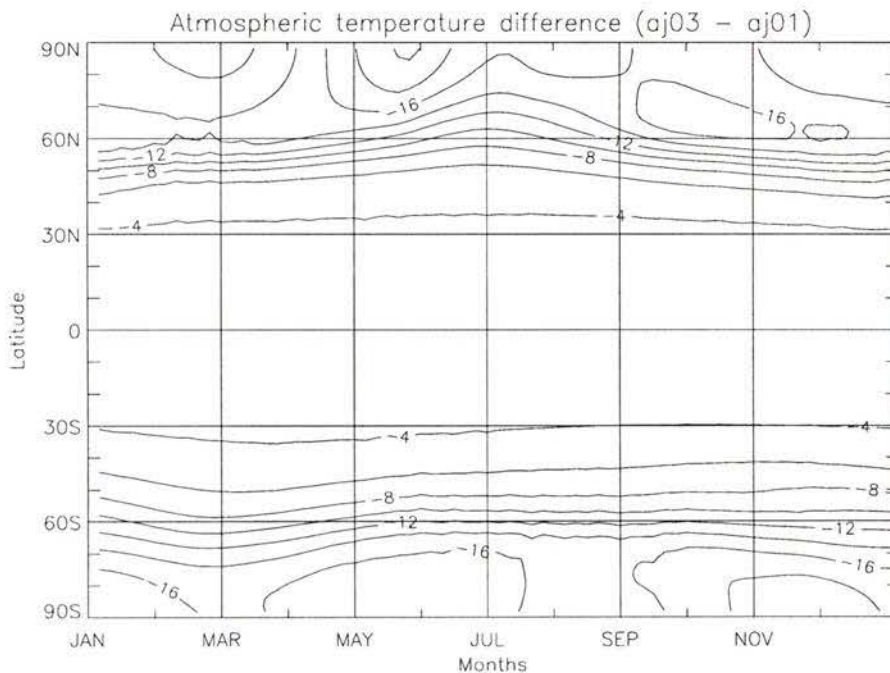


Figure 3.7 Latitude vs. time distribution of the difference in zonal mean surface air temperature (°C) between the aj03 and aj01 experiments. Contour intervals are 2°C.

Figure 3.7 illustrates the seasonal response following the change in the albedo jump from 0.1 to 0.3 through a latitude vs. time plot of the difference in zonal mean SAT between the two experiments. The cooling occurs throughout the year and is enhanced at high latitudes where snow/ice covered surfaces are present. Maximum cooling in the southern high latitudes takes place during the winter months (May-June-July) and summer months (November-December-January) when differences in snow-ice covered areas are the largest and solar insolation reaches its extremes.

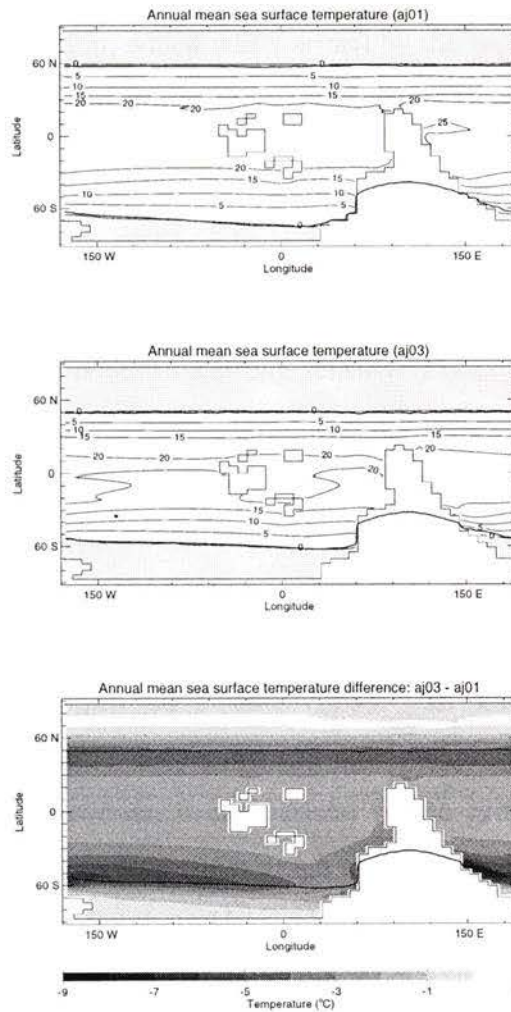


Figure 3.8 Top and middle) Annual mean SST ($^{\circ}\text{C}$) distributions for the aj01 and aj03 experiments respectively. Contour intervals are 5°C . Heavy line over the ocean represents the maximum sea-ice extent whereas over Gondwana, it represents the location of the -10.0°C contour or the snow extent (whichever extends the furthest to low latitudes). The ice edge delimits the maximum snow/sea ice covered area present during a one-year period. Bottom) Annual mean SST ($^{\circ}\text{C}$) difference between the aj03 and aj01 experiments. Heavy line is ice edge for aj03 experiment and contour intervals are 1°C .

Figure 3.8 shows the annual mean sea surface temperature response to changes in the albedo jump (aj01 and aj03). As indicated by the heavy line, the ice edge in the northern high latitudes expanded 10° equatorward between the aj01 and aj03 experiment due to the enhanced snow/ice albedo effect (top and middle figures). The difference in the annual mean sea surface temperature between the aj03 and aj01 experiments (bottom figure) shows a cooling over all latitudes except for the regions where permanent sea ice is present in both experiments (Northern Hemisphere high latitudes). Equatorial and subtropical SSTs cooled by $\sim 2^\circ\text{C}$. The largest cooling is found along the southeastern coast of Gondwana. This region, which was warmed by the western boundary Antarctica current (Figure 4.1) in the aj01 experiment, is permanently covered by sea ice in the aj03 experiment.

3.2.2 Meridional overturning response

The ocean circulation also shows a strong sensitivity to changes in the albedo jump, as depicted in Figure 3.9. The top graphs of Figure 3.9 show the global overturning streamfunction for the aj01 and aj03 experiments whereas the bottom left graph shows the difference in the annual mean meridional overturning streamfunction between the two experiments. The figures reveal an equatorward shift of the location of deep water formation and a weakening of the overturning streamfunction above 2,000 m with a higher albedo jump (between 60°S and 75°S). In addition, the overturning streamfunction shows a marked deepening and strengthening below 2,000 m with an increased albedo jump. However, a comparison of the global ocean heat transport between the two sensitivities (bottom right graph of Figure 3.9) shows a decrease in the poleward heat transport in the Southern Hemisphere and north of 35°N with an increased albedo jump. In the Southern Hemisphere where there exists a meridional land barrier, the overturning is the most dominant mechanism for heat transport. The reduction that occurs there with an increased albedo jump is due to surface waters being significantly cooler with the increased albedo jump (Figure 3.8).

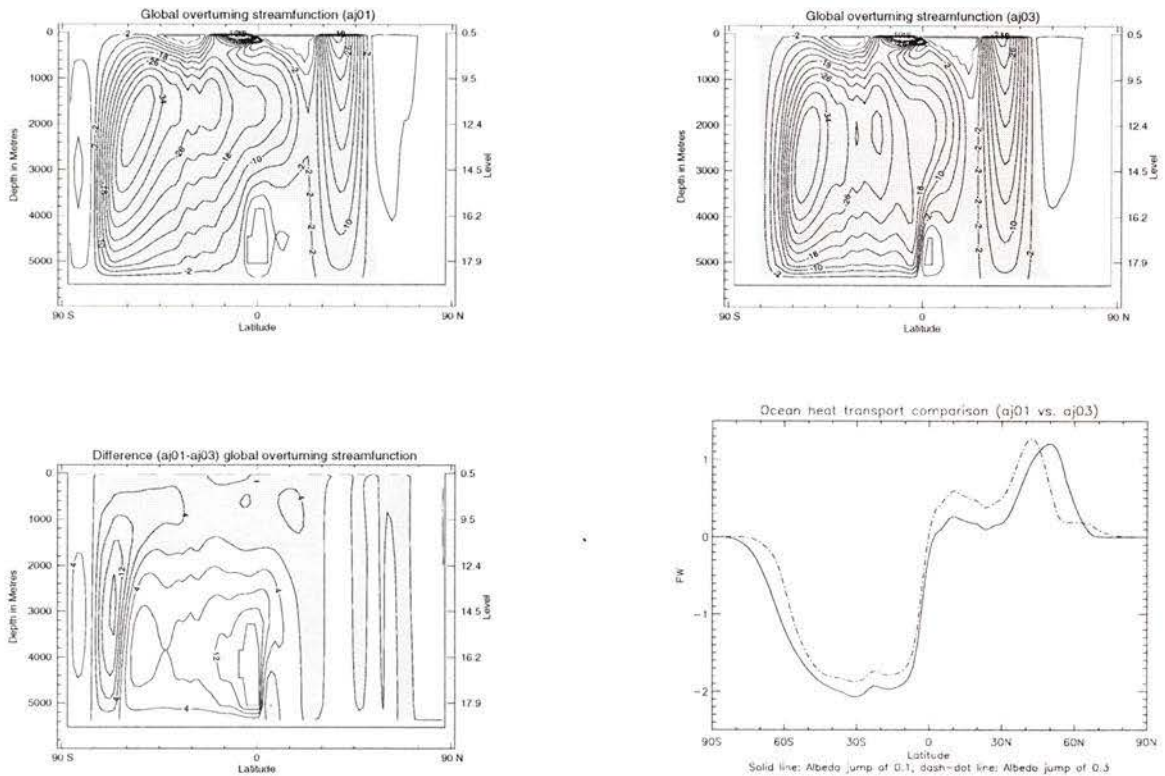


Figure 3.9 Top graphs) Global overturning streamfunction for aj01 (left) and for aj03 (right). Bottom left) Difference in global overturning streamfunction (S_v) between the aj01 and aj03 experiment. Contour intervals are $4 S_v$. Bottom right) Global ocean heat transport comparison in PW ($1 \text{ PW} = 10^{15} \text{ W}$) between aj01 (solid line) and aj03 (dash-dot line).

3.2.3 Glacial response

The sea ice extent adjacent to the South Pole increased from $2.83 \times 10^6 \text{ km}^2$ in the aj01 run to $17.70 \times 10^6 \text{ km}^2$ in the aj03 run, whereas the January average snow cover on Gondwana increased from $0.17 \times 10^6 \text{ km}^2$ to $14.50 \times 10^6 \text{ km}^2$.

Averaged January snow thicknesses for the aj01, aj02 and aj03 experiments are shown in Figure 3.10. For the aj01 experiment, snow cover is very thin and concentrated on the southern edge of Gondwana. For the aj03 experiment, the January snow cover with a thickness greater than 50 m coincides with the majority of the glacial deposits.

The annually averaged sea ice concentrations for the albedo experiments are shown in Figure 3.11. Over land, the 0.9 contour interval represents the area over which snow cover survived 90% of the year. For the aj03 experiment, the area inclusive of all glacial

deposits is snow covered 60% of the year whereas for the aj01 experiment, this area is only fully covered 30% of the year.

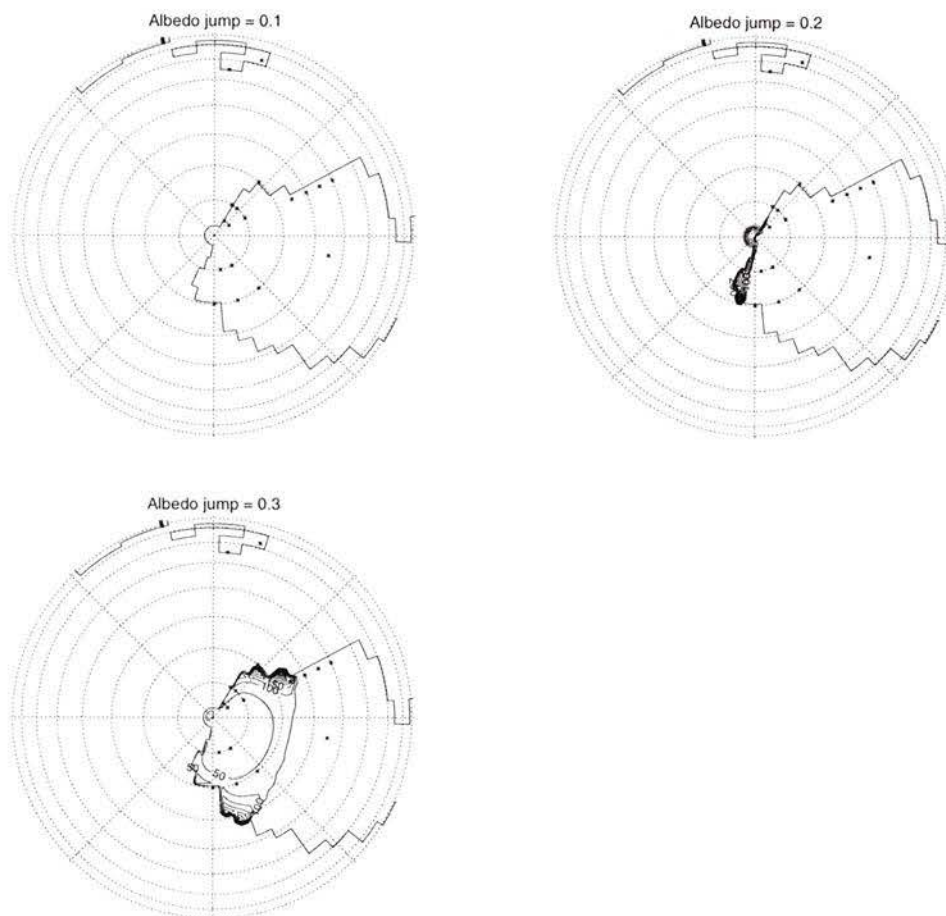


Figure 3.10 January averaged snow thicknesses (m) for albedo jumps of 0.1, 0.2 and 0.3. Contour intervals are 50 m and asterisks represent an approximate distribution of glacial deposits [*Paris et al.*, 1995].

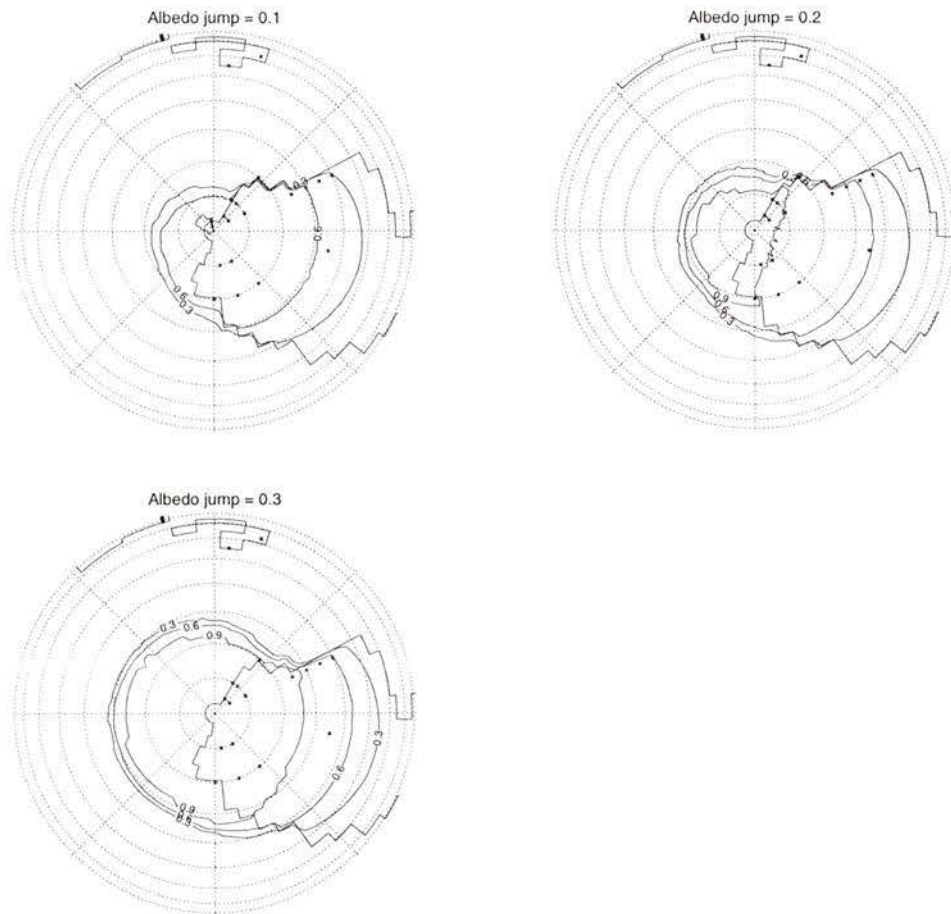


Figure 3.11 Annually averaged ice concentration for albedo jumps of 0.1, 0.2 and 0.3. Contour intervals are 0.3 and asterisks represent an approximate distribution of glacial deposits [Paris *et al.*, 1995].

3.3 Model sensitivity to orbital parameters

The sensitivity of the coupled model to changes in orbital parameters within the Late Ordovician context is assessed for the extreme set of orbital forcing: a “cold summer orbit” (CSO) vs. a “hot summer orbit” (HSO). Obliquity, longitude of perihelion and eccentricity values specific to each experiment are provided in Table 2.4. The two experiments (10x_cso_aj01, 10x_hso_aj01) are started from rest and integrated 3000 years to achieve equilibrium. All experiments have 10x CO₂, a decreased solar luminosity by -4.5%, albedo jump of 0.1 and a LOD of 21.5 hours and differed solely by their orbital configuration. The key findings are summarised in Table 3.2 and are analysed in further detail in the following sections.

3.3.1 Temperature response

The annual mean insolation receipt at the top of the atmosphere depends on the eccentricity and hence, does not vary between the CSO and the HSO experiments. However, the latitudinal profile of the zonally averaged annual insolation receipt, as depicted in Figure 3.12, shows some marked differences between the two configurations. While the polar latitudes receive an annual excess of solar insolation of as much as 16.5 Wm^{-2} for the HSO compared to CSO, which has a maximum obliquity of 24.5° , the equatorial and tropical latitudes receive less insolation in the HSO compared to the CSO (maximum deficit = 4 Wm^{-2} about the equator). This is because the astronomical control factor at high latitudes is obliquity whereas at low latitudes, the eccentricity-precession term dominates (Section 2.2.3).

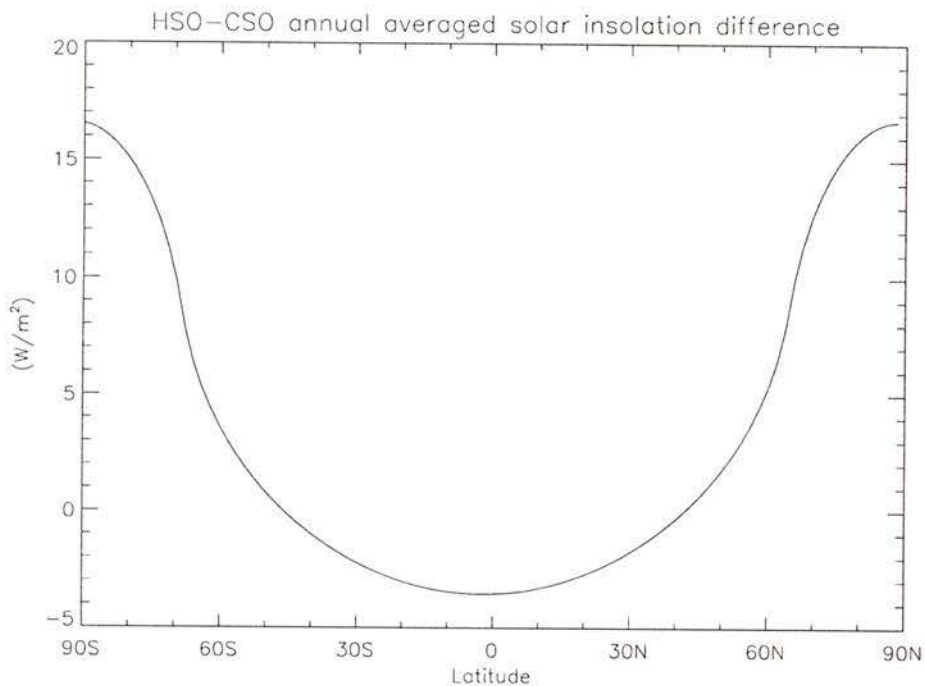


Figure 3.12 Annually averaged solar insolation difference (Wm^{-2}) at the top of the atmosphere between the HSO and CSO.

The climatic response to the spatial variations in insolation is mapped in Figure 3.13, which shows the annual mean SAT distribution for the HSO, CSO as well as the difference between the two extreme configurations. It is evident from the figure that the annual mean surface air temperature field strongly depends on the solar insolation

forcing. Equatorial and tropical SATs are $\sim 0.5^{\circ}\text{C}$ cooler whereas polar temperatures are $\sim 1^{\circ}\text{C}$ warmer for the HSO configuration. Maximum warming occurs in polar latitudes of both hemispheres where the difference in annual solar radiation is the largest.

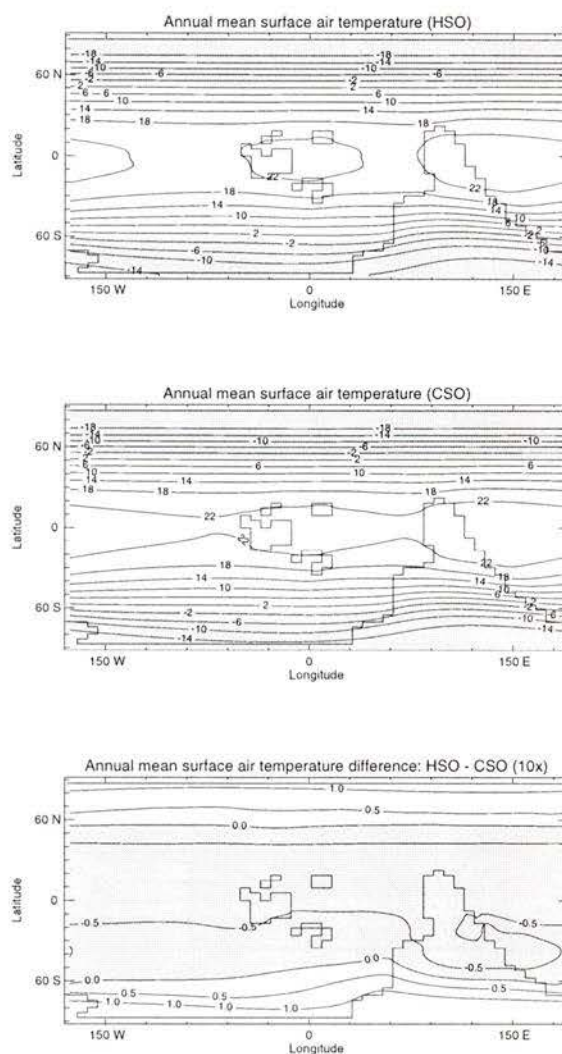


Figure 3.13 Annual mean surface air temperature ($^{\circ}\text{C}$) for HSO (top), CSO (middle) and difference (HSO – CSO) (bottom). Contour intervals are 4°C for the top two figures and 0.5°C for the bottom figure.

Although changes in the orbital forcing influence the spatial distribution of atmospheric temperatures, results show no major changes on annually averaged global ocean and atmospheric temperatures (Table 3.2). The absence of a global thermal response is explained by the fact that the annual insolation receipt is not altered significantly between the two configurations.

The intensity of the seasonal cycle is accentuated in the HSO experiment and diminished in the CSO experiment, as depicted in Figure 3.14, which shows the latitude vs. time distribution of the difference in zonal mean surface air temperature between the HSO and CSO experiments. These results are in accordance with the insolation graphs shown in Figure 2.2. An analysis of the seasonal cycle provides a means for determining the critical summer temperature for which glacial inception is still possible. When summer temperatures are too hot, the development of a permanent ice cap is not possible. Figure 3.14 shows that October polar SATs are $\sim 9.5^{\circ}$ cooler for the HSO experiment whereas February SATs are $\sim 7.5^{\circ}\text{C}$ warmer.

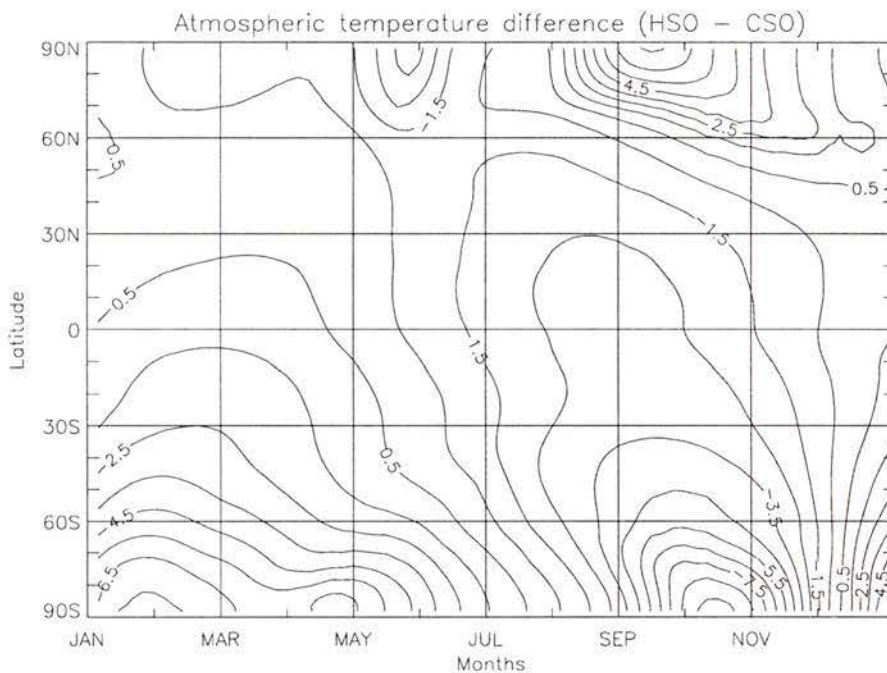


Figure 3.14 Latitude vs. time distribution of the difference in zonal mean surface air temperature ($^{\circ}\text{C}$) between the HSO and CSO experiments. Contour intervals are 1°C .

3.3.2 Meridional overturning response

The meridional overturning response to changes in orbital configuration is evident in Figure 3.15, which shows the annual mean global overturning streamfunction for the CSO, HSO as well as the difference between the two experiments.

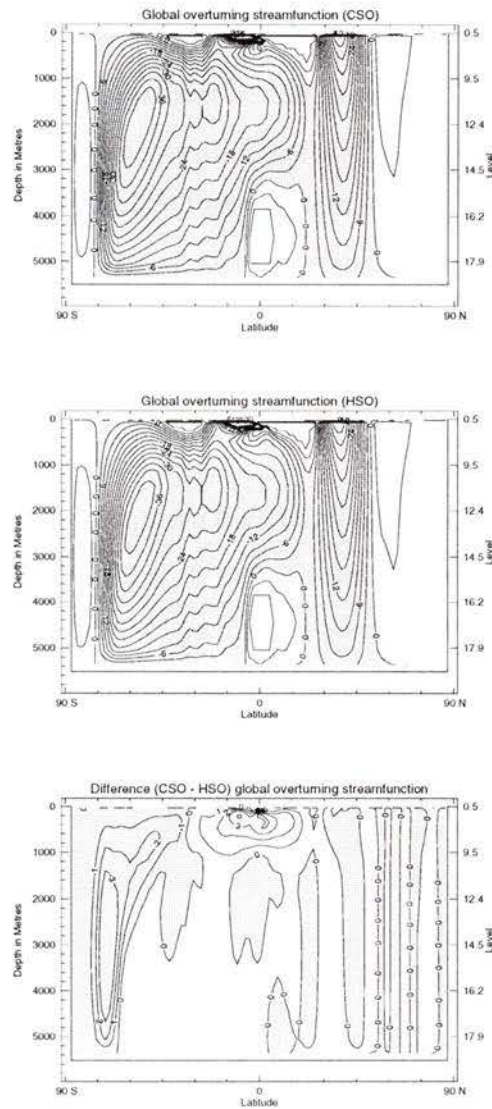


Figure 3.15 Global overturning streamfunction for CSO (top), HSO (middle) and difference between the two extreme configurations (Sv). Contour intervals represent 3 Sv for the top two figures and 1 Sv for bottom figure.

The overturning response to changes in orbital forcing corresponds to a ~ 3 Sv increase in the amount of deep water formed in the high southern latitudes for the CSO relative to the HSO configuration. The total amount of deep water transported back to equatorial latitudes (~ 19 Sv) did not change considerably between the two experiments.

3.3.3 Glacial response

This section presents an assessment of the modelled glacial response, relative to changes in orbital forcing. As shown in Figure 3.12, the decrease in incoming solar radiation at high latitudes for the CSO experiment, should result in an increase of the snow cover and sea ice extent. The spatial increase of highly reflective surfaces should produce a further decrease in incoming solar radiation, resulting in a further cooling. This explains why the thermal response is amplified at high latitudes through this positive feedback loop.

The extent of sea ice in the southern high latitudes (January average) increased from $0.65 \times 10^6 \text{ km}^2$ for the HSO to $2.90 \times 10^6 \text{ km}^2$ for the CSO configuration. There was no permanent snow cover for the HSO experiment whereas for the CSO, the modelled snow cover was $0.54 \times 10^6 \text{ km}^2$. The extent of the Northern Hemisphere sea ice cover was maximum for the HSO experiment ($21.4 \times 10^6 \text{ km}^2$) as the configuration corresponds to a CSO configuration for the Northern Hemisphere.

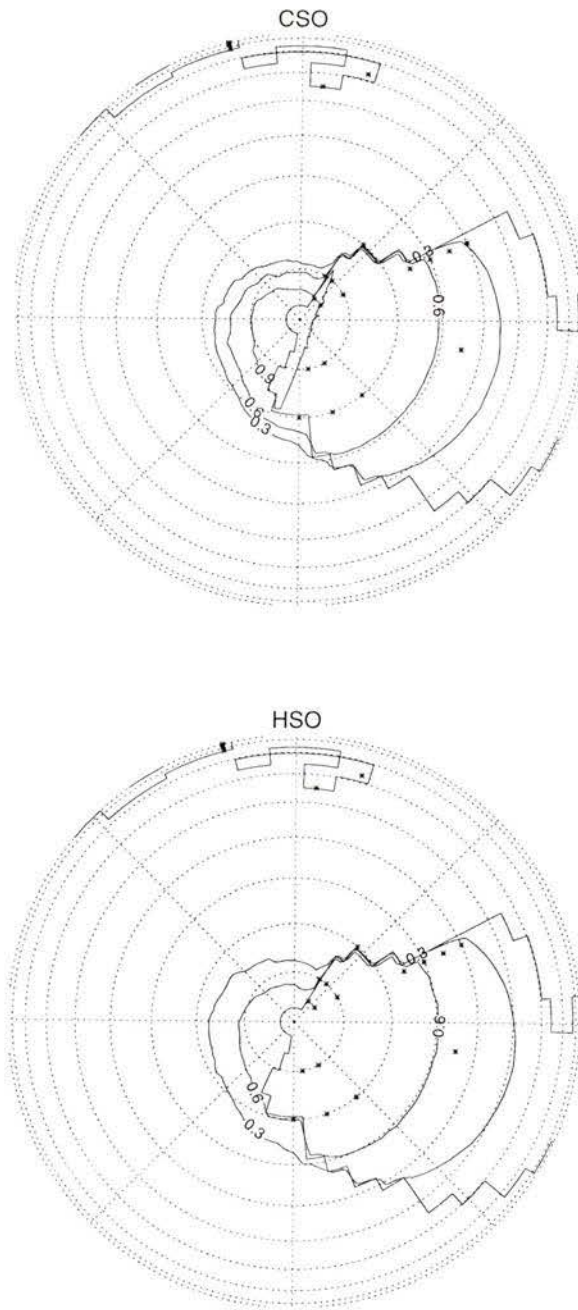


Figure 3.16 Annual mean ice concentration for CSO and HSO experiments. Contour intervals are 0.3 and asterisks represent an approximate distribution of glacial deposits [Paris *et al.*, 1995].

4. Discussion of results

4.1 Paleooceanography of the Ordovician

Previous attempts to describe wind-driven circulation patterns characteristic of the Ordovician Period have been based on principles of ocean-atmosphere dynamics as well as present-day analogues [Wilde, 1991; Wilde *et al.*, 1991]. The present study is the first attempt to investigate the paleooceanography of the Late Ordovician through coupled ocean-atmosphere modelling experiments. Sections 4.1.1 and 4.1.2 include a discussion of the general wind-driven and thermohaline circulation patterns produced in this study whereas Section 4.1.3 provides a review of global heat transport patterns.

4.1.1 Wind-driven circulation

The wind-driven circulation of the Ordovician Period was drastically different than that of present-day primarily because of the unique geographic positioning of the continents particular to that time. The atmospheric circulation prescribed in this model and responsible for the surface ocean circulation was derived from previous modelling experiments conducted with the atmosphere general circulation model GENESIS [Gibbs, 1996]. Monthly averaged wind stress fields were interpolated to fit the MOM2 grid resolution (from $\sim 4.5^\circ$ lat x 7.5° long to 1.855° lat x 3.75° long) and used as forcing for the initiation of currents at the sea surface (Figure 2.3). The Northern Hemisphere zonal wind flow distribution includes the northeasterly Trade Winds between 10°N and 30°N , the Westerlies between 30°N and 60°N and finally the Polar Easterlies north of 60°N . The Southern Hemisphere wind patterns mirror their counterpart in the North.

The modelled surface circulation patterns obtained in the present study are shown in Figure 4.1. These patterns compare well with the description provided by Wilde [1991]. Due to the absence of continental masses in the Northern Hemisphere, the wind stress field between 30°N and 60°N induces a strictly zonal west-to-east surface circulation. Panthalassic waters confined to this latitudinal belt travel at high velocities (average = 24

cm/s) as they circle the globe unimpeded (North Subpolar Circumpolar Current). These speeds are comparable with present-day values for the Antarctic Circumpolar Current. The east-to-west surface currents adjacent to the North Pole are weak as a low energy wind stress field drives the ocean's surface.

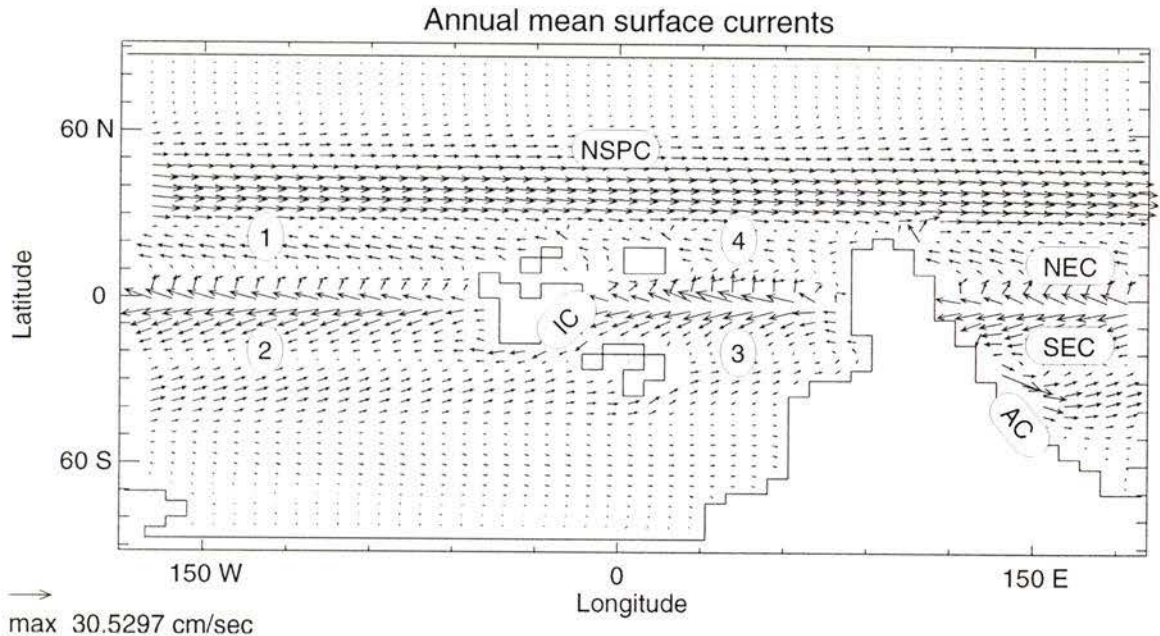


Figure 4.1 Annual mean surface velocities (cm/s) obtained from Ordovician control experiment. Ovals represent ocean gyres: (1) North Panthalassic convergence (2) South Panthalassic convergence (3) South Paleo-Tethys convergence (4) North Paleo-Tethys convergence. Rounded-rectangles represent surface currents: North sub-polar circumpolar current (NSPC), Iapetus current (IC), North and South equatorial currents (NEC, SEC) and Antarctica current (AC). Vectors are drawn every tracer grid point for legibility.

The presence of Laurentia, Baltica, Siberia and northern Gondwana results in the formation of meridional flows in equatorial latitudes. Strong westward flowing equatorial currents straddling the equator exist between Laurentia and northern Gondwana. Laurentia and Siberia act as meridional barriers as they divert the North Equatorial Current northwards and force the flow to join the North Paleo-Tethys ocean gyre. The South Equatorial Current travels freely across the Panthalassic Ocean until it reaches the Australian-Antarctic shield and becomes the vigorous western boundary Antarctica Current as it travels towards the South Pole. The second segment of the South Equatorial Current arises from the South China region and flows westward until the Avalonian-Baltica shield blocks it. Two major oceanic high pressure gyres are present in

the southern midlatitudes: the south Panthalassic gyre and the south Paleo-Tethys gyre. The two systems are linked through the Iapetus current.

As discussed by *Wilde* [1991], paleontological and geochemical evidence for sustained upwelling during the Ordovician is found along the equatorial divergence zone from the west coast of Laurentia to the east coast of Gondwana in coastal Australia. The austral hemisphere, although partially covered by sea ice at the time, also holds a record of past upwelling activity. Upwelling regions include South Central Europe and northwest Arabia [*Wilde*, 1991].

As shown in Figure 4.2, the modelled upwelling regions coincide with the paleontological evidence for increased productivity, particularly at equatorial latitudes. The magnitude of the vertical velocities at a depth of 50 m (maximum= 2.870×10^{-3} cm/s) is comparable with present-day Tropical Pacific upwelling velocities (5.787×10^{-3} cm/s) although slightly weaker.

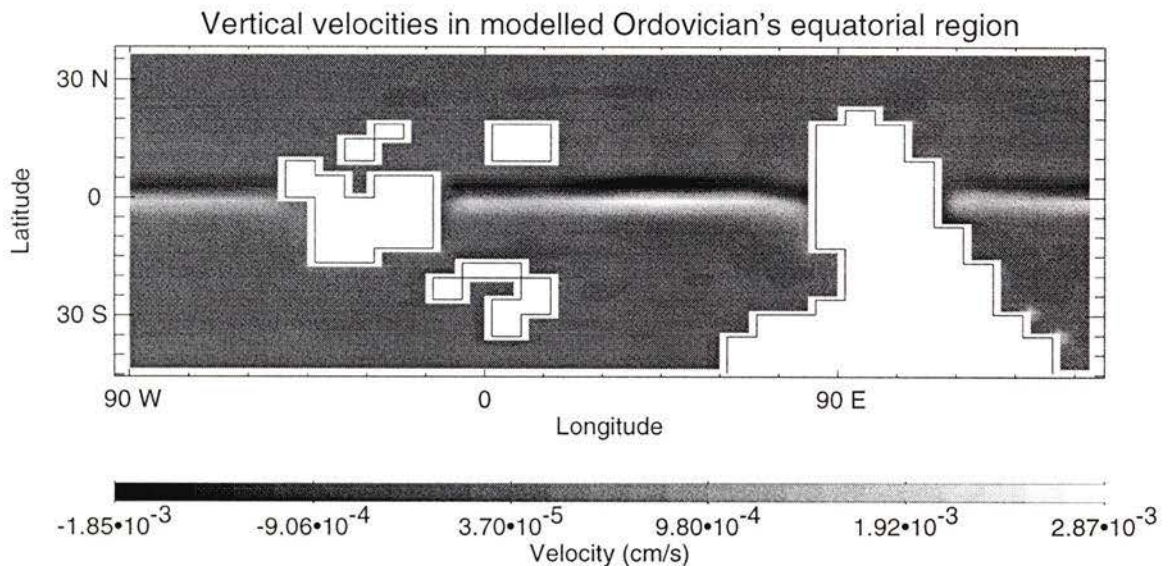


Figure 4.2 Equatorial vertical velocities (cm/s) in Ordovician control experiment at 50 m.

The heat flux at the ocean-atmosphere interface reveals a distinct band of oceanic heat gain along the equator (not shown). The easterly tradewinds (Figure 2.3) generate large Ekman transport on both sides of the equator. Upwelling takes place to compensate for the lateral removal of water by Ekman transport. Maximum heat flux in the

equatorial Panthalassic Ocean is displaced eastward relative to the region of strongest upwelling (not shown). The reason for the lateral displacement is that the coldest upwelled waters are located at the east of the basin. Maximum heat flux value for the Ordovician experiment is 152 W/m^2 whereas for present-day runs, maximum value is about 200 W/m^2 .

A cautionary note is now mentioned regarding the correlation between modelling results and the stratigraphic record. Although the width of the equatorial heating region stretches out to about 1000 km on both sides of the equator, the upwelling zonal band is much narrower. The reason for this is that once the cold water has been upwelled to the surface, it necessitates several months to attain thermal equilibrium with the overlying atmosphere during which time it can travel 1000 km towards the poles due to the Ekman drift [Tomczak and Godfrey, 1993]. It is clearly a challenge to precisely locate upwelling regions of the Ordovician Period. In addition, the climatic parameters (e.g. black shales, phosphate) used for determining past zones of upwelling may lead to several different interpretations. It is in light of these constraints that we have presented these results.

4.1.2 Thermohaline circulation

The zonally averaged depth profiles of temperature, salinity and potential density suggest that the main sources of deep water for the Ordovician experiments are located in the North and South Panthalassic Ocean (not shown). The presence of sills between Greenland and Scotland plays an important role in the present-day spatial distribution of the deep-water formed in the Norwegian Sea. The modelling experiments conducted in the present study cannot address the influence of bathymetry on deep-water circulation as a flat-bottom topography is prescribed. It is useful to note however, that the presence of mid-ocean ridges has been suggested in past studies [Wilde, 1991] as an explanation for the temporal changes in the nature of deep-sea sediments during the Ordovician Period.

It is likely that the Late Ordovician glaciation produced favourable conditions for an enhanced creation of deep water, particularly during the austral winter season. A change in deep-ocean circulation patterns would modify depositional environments in the

vicinity of the continental rise. This is in fact observed at the deep sea fan deposits of Dob's Linn, Scotland where for the pre-glacial period, deposits are anoxic black shales whereas upper Ordovician deposits are oxic mudstone. This change in the stratigraphy suggests a shift in the oceanic circulation; from sluggish or even fully inhibited to a well-ventilated state.

Wilde [1991] hypothesised that during the Ashgill glaciation, the deep water, which formed more vigorously as a result of the presence of an extensive sea ice cover around the South Pole may have reached the Iapetus Ocean, thereby producing well-ventilated waters. In addition, subpolar waters were probably cooler and better oxygenated. The sinking subpolar waters would have cooled central waters by vertical advection. *Wilde* [1991] argued that although Dob's Linn was then located in the proximity of Laurentia, which was in equatorial latitudes, the offshore fans might have been overlaid by cold and oxygen-rich central waters. This change in deep-water circulation would explain the shift from anoxic to oxic modes of deposition. The deep-sea fan deposits of South China exhibit anoxic conditions throughout the glaciation. It is possible that the cold and dense water formed in the proximity of the Gondwanan ice shelf was inhibited from entering the Paleo-Tethys ocean because of a mid-ocean ridge associated with the opening of the Rhaeic Ocean [*Wilde*, 1991].

As discussed in Section 1.4.5, the *gracilis* transgression must have brought about the flooding of extensive continental areas. Epicontinental seas or marginal seas located in critical regions of net evaporation would have been ideal sites for the production of warm and saline deep waters [*Brass et al.*, 1982]. Although the land-sea distribution used in the present study did not include shallow epicontinental seas, modelling results do point to two potential regions prone to the creation of warm saline bottom waters (not shown). The passage between Laurentia and Siberia and the gap between Avalonia and Baltica appear as regions where surface currents are slow, SSTs and SATs are high and evaporation rates far exceed precipitation rates, giving rise to surface salinities of 36.1 psu and 35.6 psu respectively.

4.1.3 Global heat transport patterns

The oceans and atmosphere play a critical role in the redistribution of the excess heat present in the tropics vs. the lack of heat in polar regions. The heat transport accomplished by these two components of the climate system allows for the global climate to be more equable than would be without this redistribution of heat. The energy balance requirements imply that at equilibrium, the time mean incoming short wave radiation balances with outgoing longwave radiation. The planetary heat transport, averaged across a line of latitude ϕ , is then calculated as follows:

$$T_{(pl)\phi} = \int_{\lambda_w}^{\lambda_e} \int_{\phi_s}^{\phi} [Q_{in} - Q_{out}] a^2 \cos\phi d\phi d\lambda,$$

where Q_{in} and Q_{out} are the zonally and annually averaged incoming shortwave and outgoing longwave radiation, a is the Earth's radius, ϕ_s is the latitude of the southern boundary and λ is longitude.

The comparison of heat transport curves obtained from Ordovician modelling experiments with experiments using present-day conditions reveals important spatial differences. These differences are primarily due to changes in the solar and atmospheric CO₂ forcings, and the significantly different geographic configuration of the major continental blocks. In this section, I discuss patterns of planetary heat transport and poleward ocean and atmosphere heat transports obtained for the Ordovician control experiment and compare these patterns with a 'present-day' run. In addition, I discuss the implications stemming from the use of prescribed present-day ocean heat transport values in modelling experiments of the Ordovician, such as was used by *Crowley and Baum* [1991; 1995] and *Gibbs* [1996].

The annual mean meridional planetary heat transport for the Ordovician control experiment at equilibrium is shown in Figure 4.3 and is divided into its atmospheric and oceanic components. The heat transport carried out by the atmosphere is estimated from subtracting the ocean heat transport from the planetary transport. In the Northern Hemisphere, the atmosphere dominates the transport at most latitudes, with a maximum

of ~ 4.5 PW near 30°N . The ocean is important in the planetary heat transport in the Southern Hemisphere and at mid-latitudes in the Northern Hemisphere. The sole region for which the oceans dominate the heat transport is located at tropical latitudes in the Southern Hemisphere. This region is characterised by the presence of the western boundary current flowing along eastern Gondwana, the Antarctica Current (Figure 4.1). The maximum poleward ocean heat transport is ~ 2.1 PW at 10°S .

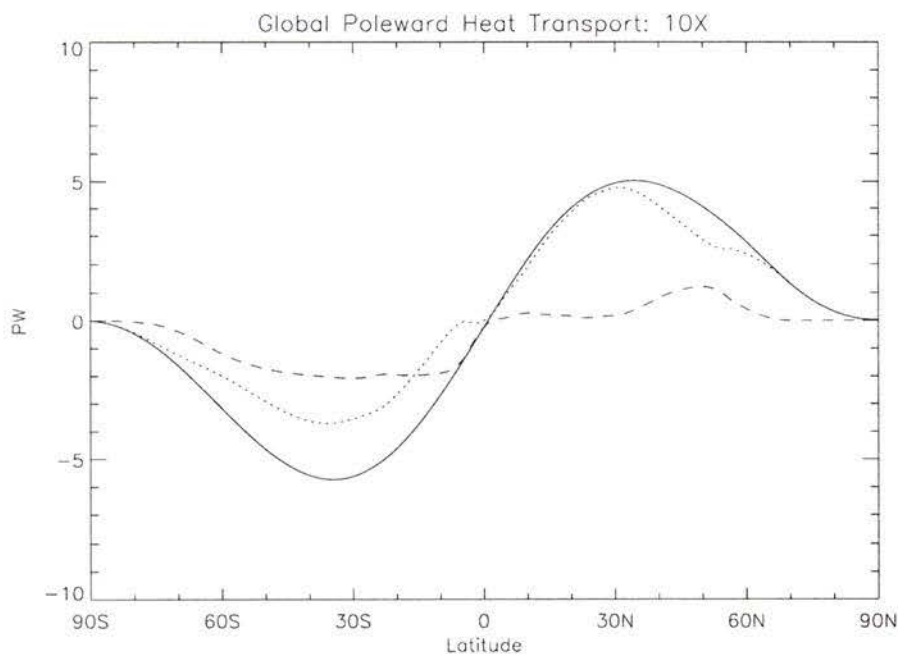


Figure 4.3 Annual mean poleward planetary heat transport in PW (1 PW= 10^{15} W) with ocean (dashed line) and atmosphere components (dotted) for Ordovician control experiment.

The global ocean poleward heat transport for the control experiment is depicted in Figure 4.4, with the dotted and the dashed curves showing the fraction of the transport done by advection and diffusion respectively. The asymmetry of the total ocean heat transport curve indicates a more significant transport in the Southern Hemisphere than in its northern counterpart. In addition, the bulk of the heat transport is done by advection (along the western boundary of the Panthalassic Ocean via the Antarctica Current). Between the equator and 25°N , the net poleward heat transport is small as the northward advective Ekman transport counters the southward subsurface diffusive transport. As one moves northward of 25°N , most poleward heat transport is done by diffusion whereas southward transport is done by advective Ekman transport.

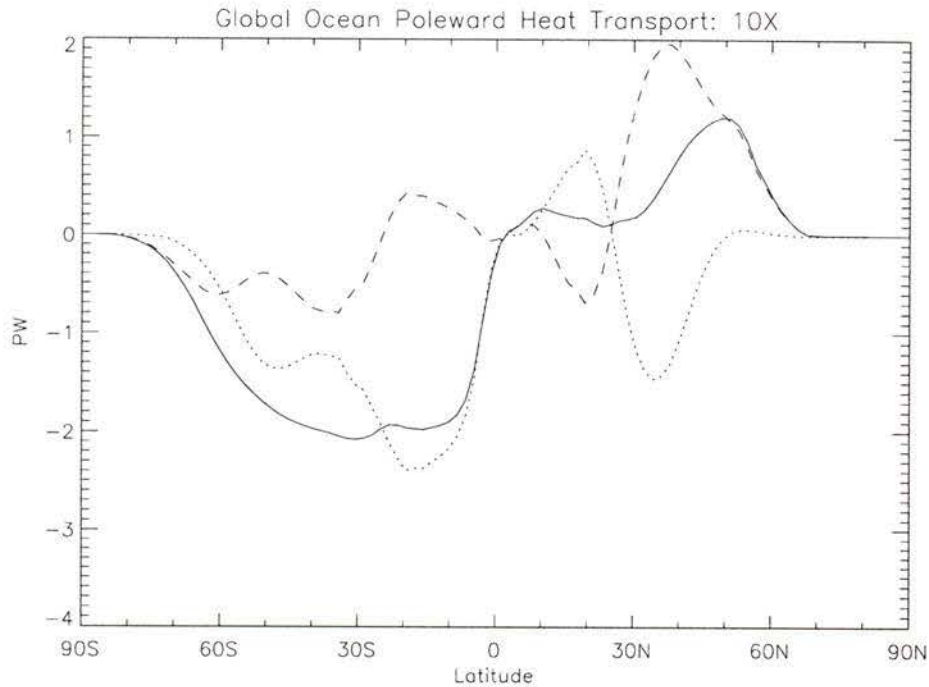


Figure 4.4 Global ocean poleward heat transport for Ordovician control experiment in PW (1 PW= 10^{15} W). The three curves represent: total transport (solid), advective transport (dotted line) and diffusive transport (dashed line).

A comparison of the planetary, atmosphere and ocean poleward heat transport between a ‘present-day’ run and the Ordovician control run is reproduced in Figure 4.5. The ‘present-day’ run has the following boundary conditions: present-day geography, CO_2 levels, orbital forcing, solar luminosity, albedo jump and LOD [Wiebe and Weaver, in press]. The two curves reveal marked latitudinal differences, which are discussed below.

The modelled planetary heat transport, which includes both atmospheric and oceanic contributions, peaks in middle latitudes with a maximum of ~ 5.0 PW in the Northern Hemisphere for both experiments and a maximum of ~ 5.5 and ~ 6.0 PW in the Southern Hemisphere for the present-day and Ordovician control experiment respectively (top graph in Figure 4.5). These values compare well with present-day estimates inferred from the Earth Radiation Budget Experiment (~ 6 PW at $\sim 45^\circ\text{N}$) although they are slightly smaller.

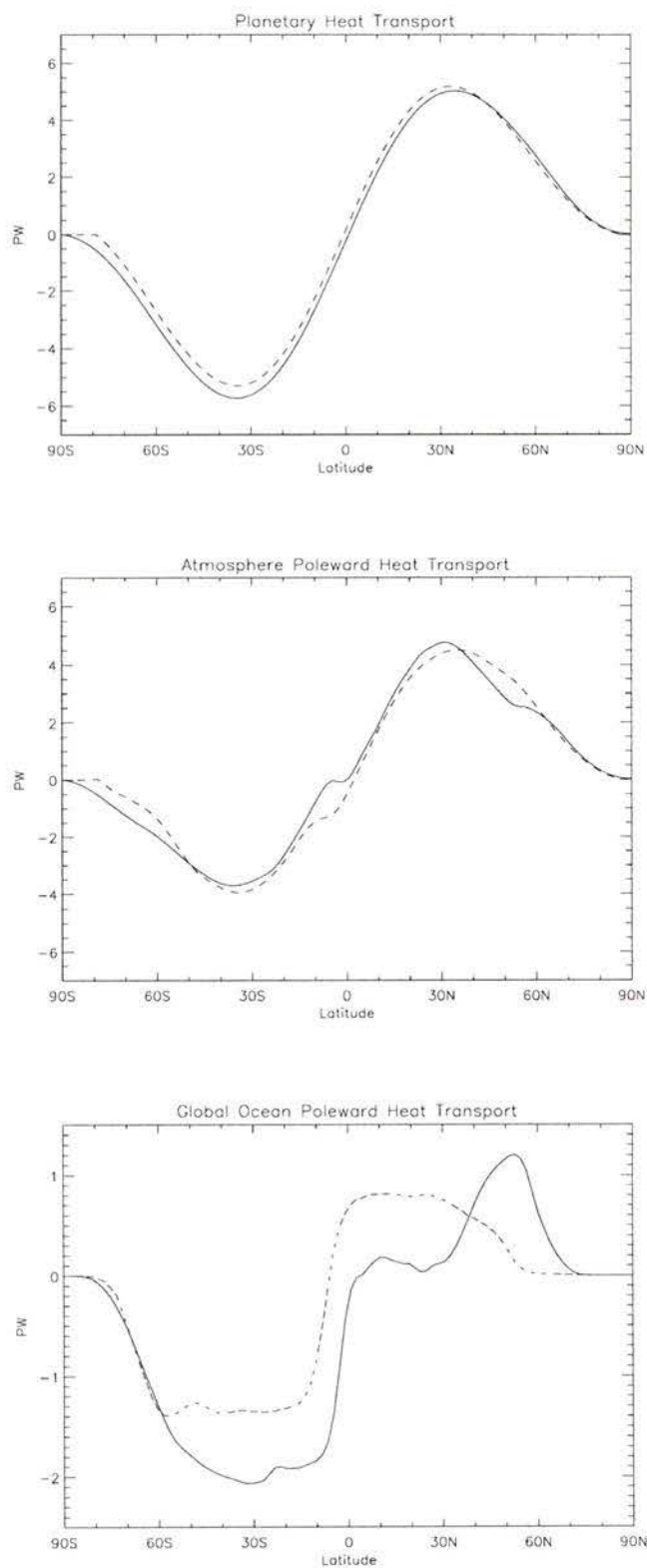


Figure 4.5 Heat transport comparison between present-day run (dashed line) and Ordovician control run (solid line) in PW (1 PW=10¹⁵W). Top) Planetary heat transport. Middle) Atmosphere poleward heat transport. Bottom) Global ocean poleward heat transport

The atmospheric and oceanic components of the planetary heat transport for the present-day run also compare well with observations [Hartmann, 1994] although small differences are apparent. Estimates derived from balloon and satellite observations of wind, temperature and humidity reveal that atmospheric transport reaches a broad maximum of about 4 PW between 30°N and 60°N [Hartmann, 1994]. Model results using present-day conditions (middle graph) agree well with this estimate (~4.5 PW). Because directly measuring the ocean heat transport is difficult and expensive one can estimate the transport by subtracting the atmosphere transport from the planetary transport. This estimate suggests that the ocean heat transport reaches a maximum of about 2.5 PW in the subtropics at ~20°N with an uncertainty of 30% or ~1 PW [Hartmann, 1994]. Estimates derived from observations suggest that the magnitude of the meridional heat transport accomplished by the Northern Hemisphere oceans is similar to that accomplished by the atmosphere although the ocean transport peaks at lower latitudes. However, due to the coarse resolution of the coupled model, the maximum ocean heat transports obtained from the present-day experiment (0.8 PW in Northern Hemisphere and 1.4 PW in Southern Hemisphere) are significantly smaller than that derived from observations [Fanning and Weaver, 1996]. This explains why the present-day modelled atmosphere heat transport is greater than observations as it needs to compensate for the underestimated ocean heat transport. Recent calculations of the planetary heat transport have included estimates of the sensible and latent heat fluxes as well as the energy storage capacity in the ocean [Hartmann, 1994]. The revised ocean heat transport estimates have decreased considerably relative to the estimates determined from the residual planetary energy balance thereby diminishing the gap between observations and modelling results.

The global ocean poleward heat transport increased by up to ~42% in the Southern Hemisphere between the present-day run and Ordovician control experiment and was shifted polewards in the Northern Hemisphere. Previous modelling experiments, which used the GENESIS AGCM with a specified mixed layer slab ocean, used a prescribed zonally symmetric ocean heat transport [Crowley and Baum, 1995; Gibbs, 1996]. The two ocean heat transport schemes used were based on estimated present-day values (with

a maximum transport of ~ 0.45 PW) and on a 50% increase (with a maximum transport of ~ 0.68 PW), to account for the potential effect of increased atmospheric CO_2 [Crowley, 1993].

There are several important implications stemming from the use of a prescribed present-day ocean heat transport in Ordovician modelling experiments. The heat transport values used by *Crowley and Baum* [1995] were significantly smaller than the values computed by the OGCM used in the present study (by ~ 1.4 PW). Their smaller ocean heat transport perhaps facilitated the inception of a permanent snow cover. In addition, the poleward heat transport averaged at each latitude used in the experiments conducted by *Crowley and Baum* [1995] was symmetrized and unchanged from the present-day run. As Figure 4.5 illustrates, the much different geographic configuration characteristic of the Late Ordovician resulted in a spatial redistribution of the heat transport and a significant asymmetry relative to the equator. Future Ordovician modelling studies using the GENESIS AGCM should include ocean heat transport values directly calculated by an OGCM, such as the ones obtained in the present study as they include the effects of the different geographic configuration of the Ordovician.

4.2 Potential for glaciation

4.2.1 Role of atmospheric CO_2 forcing

In this model, melting of snow over land is initiated when atmospheric temperatures rise above -10.0°C . The length of the melt season in the CFWS experiments substantially increases with higher CO_2 levels, as indicated in Figure 4.6. There are 145 melting days/year for the 10x experiment whereas for the 18x experiment, melting takes place for 170 days/year. Assuming a maximum melt rate of 5 cm/day, this implies that for an ice cap to develop on Gondwana, the minimum winter snow depth needs to be greater than 7.25 m for the 10x (rain equivalent = 2.2m) and 8.50 m for the 18x (rain equivalent = 2.6 m) in order to exceed the summer melt. In order to accumulate these amounts of snow during the winter months, precipitation rates should near 3.65 m/yr

(10x) and 4.87 m/yr (18x). Present-day precipitation rates rarely exceed ~5 m/yr and so these estimates appear realistic for regions where high precipitation would be expected such as along mountain ranges or coastal areas. However, it is unlikely that precipitation rates would be this high in the interior of Gondwana.

Another notable feature of Figure 4.6 is the timing of the relative maxima of cooling between the two experiments. The maximum difference in atmospheric temperatures occurs during the austral winter when sea ice and snow cover are at their maximum extent. The annual mean polar temperature for the 10x is -14.69°C and is -9.95°C for the 18x experiment (Table 4.1).

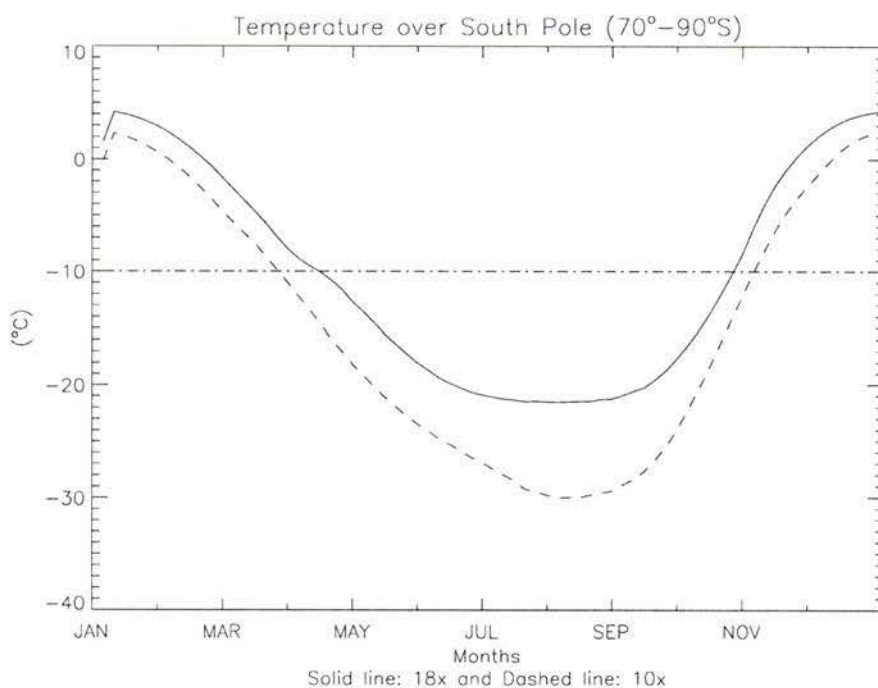


Figure 4.6 Annual spatially averaged temperature ($^{\circ}\text{C}$) over the South Pole ($70^{\circ}\text{-}90^{\circ}\text{S}$), as a function of time of year. Solid line represents the 18x sensitivity and the dashed line represents the 10x sensitivity (CFWS). Dashed-dotted line represents the critical temperature above which melting of the snow cover on land is initiated.

The 14x and 18x CO_2 sensitivity experiments performed in this study did not lead to the significant development of a permanent Southern Hemisphere ice sheet. However, the 10x_wfcs_aj01 experiment yielded a snow and sea ice area equivalent to 25% of the estimated ice sheet extent of the Late Ordovician [Crowley and Baum, 1991].

Geochemical isotopic excursions (Section 1.6.2) derived from the Ordovician geologic record suggest an array of possible time frames for the glaciation, the shortest one being ~1 m.y. Clearly, if the glaciation was indeed brief, several orbital configurations could still have been involved during the length of the event. Hence, our use of an intermediate configuration to examine the average climate produced under the specified boundary conditions is justified. It is also possible that an extreme orbital configuration could have played a conditioning role for the creation of a glacial climate nearing the end of the Ordovician. One could carry on a second series of CO₂ sensitivity experiments (with 14x and 18x CO₂) with a CSO configuration in order to test the potential for glacial inception given ideal orbital forcing for the triggering of an ice age.

4.2.2 Role of the change in albedo jump

The nature of the earth's surface (vegetation cover, snow-ice cover, etc.) strongly influences the amount of solar radiation absorbed or reflected at the surface. Hence, the albedo, defined as the ratio of the reflected over the incoming solar radiation, plays an important role in the energy balance. The model partially accounts for this mechanism by allowing the planetary albedo to decrease whenever snow/ice surfaces are present. No parameterisation is included for changes in albedo over land due to variations in vegetation cover and soil types or to the presence of epicontinental seas. This approach is adequate since the Ordovician Period took place prior to the development of land plants and precise knowledge of the geographic location of lakes is limited.

The albedo sensitivity experiments conducted in this study were aimed at evaluating the climatic effects of prescribing high albedo values of snow and ice covered surfaces. As expected, results show the strongest thermal and oceanic responses at high polar latitudes (Figure 3.7 and 3.8 respectively).

The surface atmospheric temperature over the South Pole vs. time of year is mapped in Figure 4.7. The change in the albedo jump from 0.1 to 0.3 resulted in a significant cooling apparent throughout the four seasons. SATs remain below -10.0°C (the

temperature above which melting occurs in the model) throughout the year for the aj03 experiment whereas the aj01 experiment has a melting season of 135 days (Table 4.1).

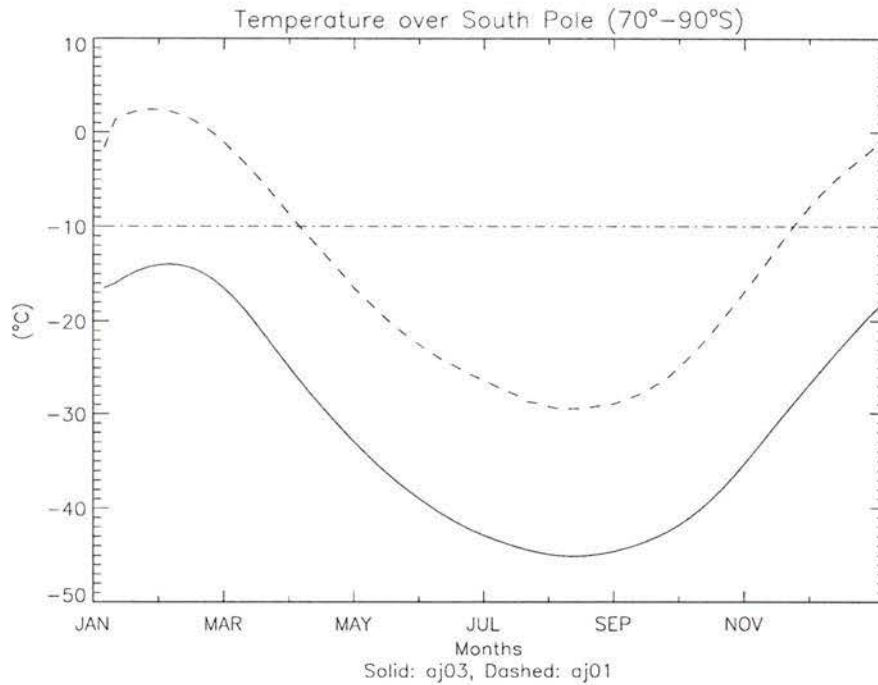


Figure 4.7 Annual spatially averaged temperature (°C) over the South Pole (70°-90°S), as a function of time of year. Solid line represents the aj03 sensitivity and the dashed line represents the aj01 sensitivity (WFCS). Dashed-dotted line represents the critical temperature above which melting of the snow cover on land is initiated.

Maximum snow cover on land was achieved in the 10x_wfcs_aj03 experiment ($14.5 \times 10^6 \text{ km}^2$). This value alone, excluding the sea ice area, represents 123% of the estimated ice sheet. Clearly, these results support the notion of sustained glaciated conditions in the southern high latitudes of Gondwana given 10x atmospheric CO_2 concentrations, a -4.5% in solar luminosity and an intermediate orbital configuration. One could conduct a series of complementary sensitivity experiments with an albedo jump of 0.3, a CSO configuration and higher levels of atmospheric CO_2 (14x, 18x) to investigate the potential for a glaciation given these extreme boundary conditions.

4.2.3 Role of orbital parameters

4.2.3.1 HSO vs. CSO

The top graph of Figure 4.8 shows a comparison of the annual solar insolation received at the top of the atmosphere over the South Pole between the HSO and the CSO experiments. The insolation curves reveal the two major characteristic influences related to the nature of orbital forcing: a latitudinal variation in insolation receipt and a change in the timing of seasons. As shown in Figure 4.8, the summer insolation received at the poles is ~30% stronger for the HSO relative to the CSO experiment (by ~180 W/m²). This increase is mostly a result of the higher obliquity in the HSO. This figure also reveals the insolation influence due to changes in the longitude of perihelion. This parameter affects the timing of the summer and winter solstices. For $\Lambda = 90^\circ$ (CSO), the Southern Hemisphere winter solstice occurs on June 13th whereas the summer solstice takes place on December 13th. For $\Lambda = 270^\circ$ (HSO), the Southern Hemisphere winter solstice occurs on June 27th and the summer solstice on December 27th. In addition, the insolation curves reveal that the lengths of the summer and winter seasons are significantly affected by the change in the longitude of perihelion (Figure 2.2). The solar insolation remains equal to zero for an additional month in the HSO configuration because the winter season coincides with the aphelion, which is where the earth is the furthest from the sun (Figure 2.2a).

As shown in Figure 3.13, annually averaged tropical and subtropical SATs are warmer by ~0.5°C in the CSO configuration. A similar pattern is true for the SST distribution (not shown). As suggested by *Peixoto* [1970], subtropical temperatures need to be sufficiently warm so as to foster enough evaporation which, through atmospheric poleward transport, contributes to the necessary moisture input for the growing of ice sheets on high latitude continental masses. The annual average precipitation rates produced in the present study show a small increase at polar latitudes for the HSO relative to the CSO configuration (not shown). However, during the months where precipitation mostly falls as snow (June-July-August), high latitude precipitation is largest for the CSO setting.

The annual cycle of the surface air temperature averaged over a 20° latitudinal band north of the South Pole varies in accordance with changes in solar insolation, as shown in the bottom graph of Figure 4.8. HSO SATs are ~8°C warmer at the beginning of February than CSO SATs whereas minimum winter temperatures differ by ~2°C. The reasoning behind the theory of the ice ages relies on the idea that summer temperatures play the critical role in glacial inception. Whereas high latitude winter temperatures are always cold enough to ensure precipitation to fall as snow, summer temperatures can be warm enough so as to prevent the development of a permanent snow cover. In fact, *Crowell* [1978] argued that summer temperatures play a more significant role in glacial inception than the supply of moisture.

Figure 4.8 shows that although temperature extremes are greater for the HSO configuration, the annually averaged polar temperature is ~1°C cooler for the CSO due to the presence of a permanent snow cover (Table 4.1). In addition, summer temperatures never rise above freezing for the CSO experiment. Following the argument presented by *Crowley et al.* [1987], with annual precipitation rates as low as 10 cm and below freezing summer temperatures, a 1,000 m thick ice sheet could be produced within a relatively short time of 10,000 years. On the other hand, extremely high snow precipitation during the winter season would not survive through a long and intense melt season.

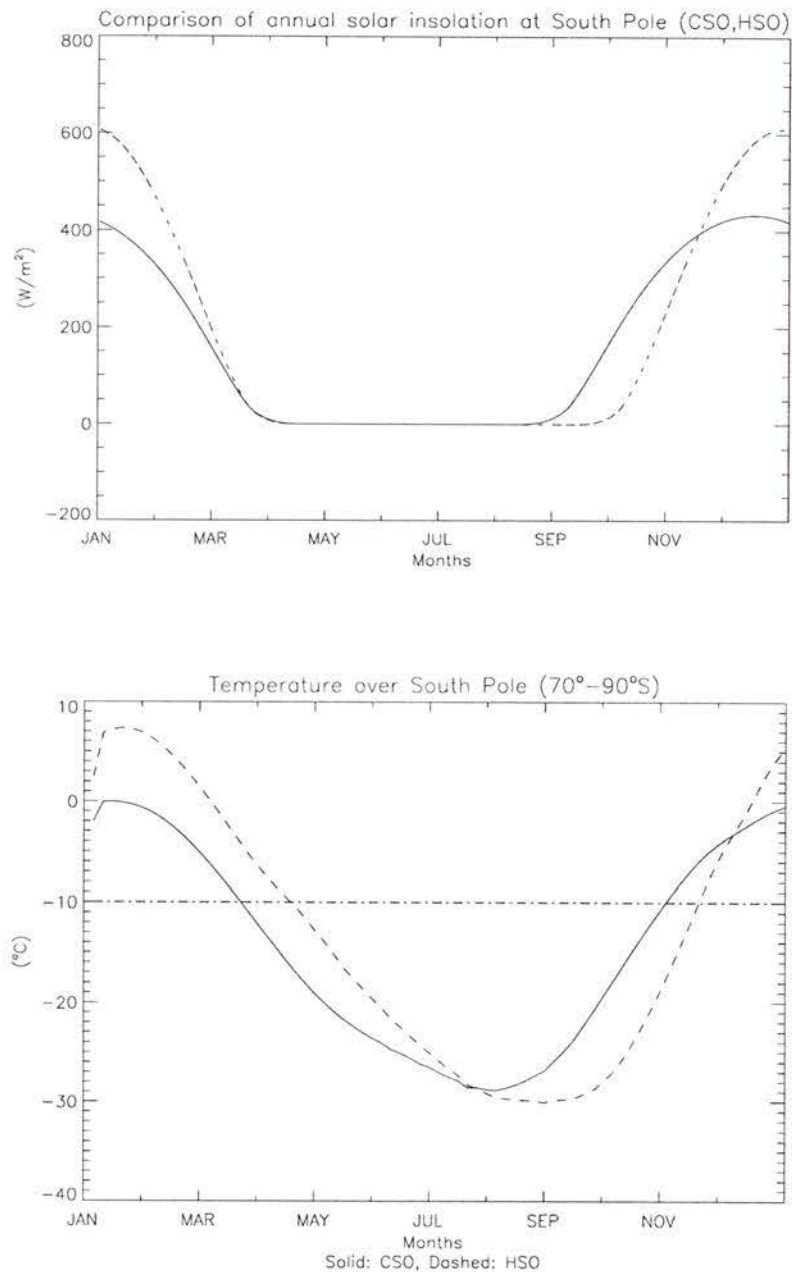


Figure 4.8 Top) Comparison of annual solar insolation (Wm^{-2}) at the top of the atmosphere over the South Pole ($70^{\circ}-90^{\circ}S$) between the CSO and HSO experiments. **Bottom)** Surface air temperature ($^{\circ}C$) vs. time of year over the South Pole ($70^{\circ}-90^{\circ}S$) for CSO and HSO. CSO (solid line), HSO (dashed line) and horizontal dashed-dotted line represents temperature above which melting occurs.

4.2.3.2 WFCS vs. CFWS

January snow cover on Gondwana survives in the WFCS and not in the CFWS experiment. However, the snow-covered area is $0.17 \times 10^6 km^2$, which is still a large

underestimate of the extent of the ice sheet as predicted from glacial deposits. Sea ice extent is maximal for the WFCS experiment ($2.83 \times 10^6 \text{km}^2$).

The CFWS and the WFCS configurations differ only by a 180° shift of the longitude of perihelion. As shown by the top graph of Figure 4.9, the overall solar insolation receipt at the top of the atmosphere is the same for the two configurations. However, the spring and fall sections of the insolation curves show marked differences, which appear to play a critical role in the snow and sea ice survival. The spring and fall sections are affected as follows. During the fall season, the insolation received at the South Pole is greater for the WFCS than for the CFWS. However, the WFCS has a shorter fall season than the CFWS. Both experiments undergo a winter season of approximately the same duration. The insolation increase associated with the onset of spring is more abrupt for the CFWS than it is for the WFCS. This, at least in part, explains the survival of a more extensive sea ice cover for the WFCS experiment, whose annual melt season is ~ 10 days shorter than for the CFWS orbit (Table 4.1). The premature onset of the melting of snow/sea ice covered surfaces in the CFWS experiment, is accompanied by a positive feedback. The feedback consists of a decrease in extent of sea ice and snow cover resulting in a decreased albedo, an increased absorption of solar radiation and an increased atmospheric temperature and melting.

The bottom graph of Figure 4.9 depicts the sensitivity of atmospheric surface temperatures over the South Pole relative to the CFWS and WFCS orbital configurations. The overall shape of the curves reveals the nature of the orbital forcing. The CFWS temperature curve shows a mild summer, a cool fall, a cold winter and warm spring season. In contrast, the polar temperature curve for the WFCS orbit shows a warm summer and fall, a cold winter and cool spring.

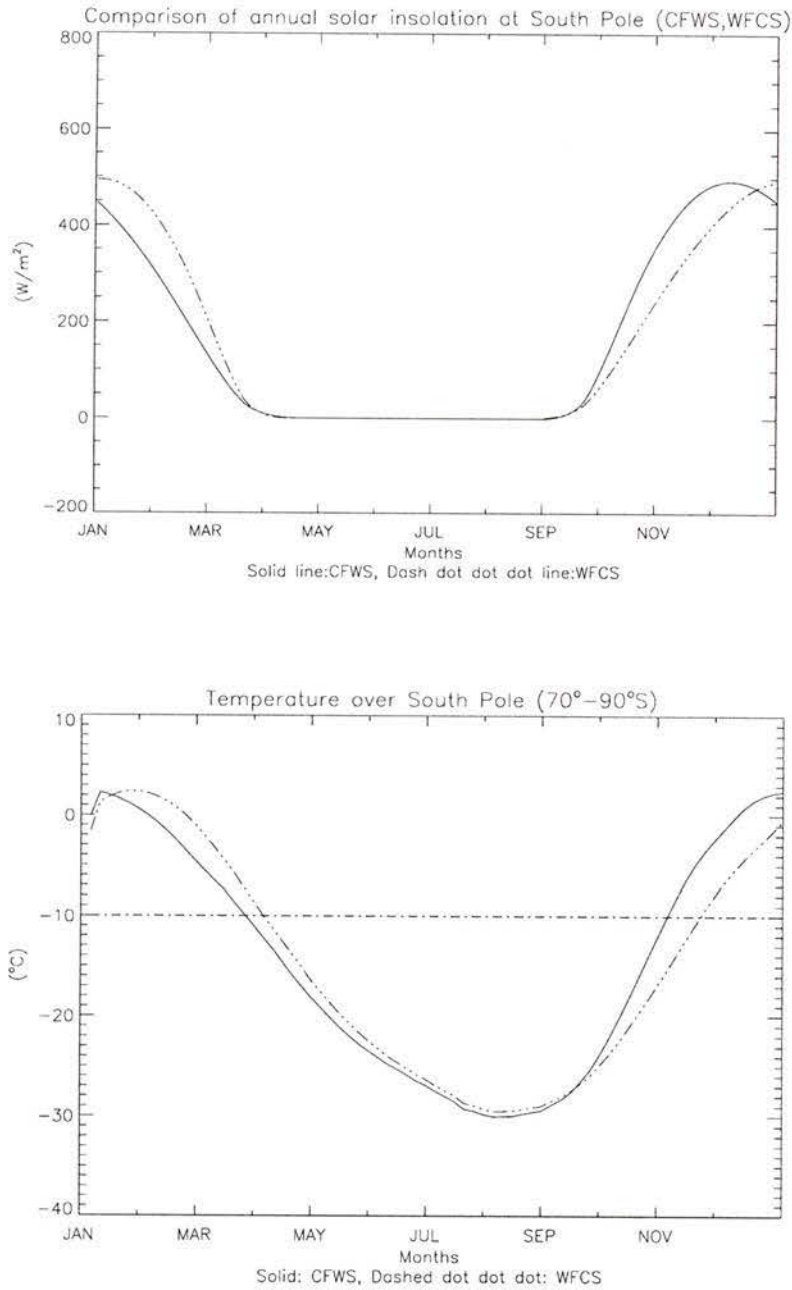


Figure 4.9 Comparison between the CFWS (solid line) and WFCS (dashed dot dot dot line) orbital configurations over the South Pole ($70^\circ-90^\circ\text{S}$). Top) Annual solar insolation incident at the top of the atmosphere (W/m^2). Bottom) Atmospheric temperatures ($^\circ\text{C}$) as a function of time of year. Dashed dot line represents the critical temperature above which melting occurs.

The length of the melt season, defined as the number of days for which the atmospheric surface temperature rises above -10.0°C , is highly sensitive to orbital forcing (Table 4.1).

Table 4.1 Climatic indicators for glacial inception on South Pole

| <i>Experiment</i> | Annually averaged polar temperature (°C) | Length of melt season (days) |
|-------------------|--|------------------------------|
| <i>10x</i> | -14.69 | 145 |
| <i>18x</i> | -9.95 | 170 |
| <i>Aj01</i> | -14.95 | 135 |
| <i>Aj03</i> | -31.64 | 0 |
| <i>H50</i> | -13.39 | 150 |
| <i>CSO</i> | -14.66 | 145 |

Experiment names represent the following runs: 10x (control), 18x (18x_cfws_aj01), Aj01 (10x_wfcs_aj01), Aj03 (10x_wfcs_aj03), H50 (10x_hso_aj01), CSO (10x_cso_aj01).

4.2.4 Northern Hemisphere glaciation

As noted in Section 1.7, there is no direct evidence for a Northern Hemisphere ice cap contemporary to the Late Ordovician glaciation [Brenchley, 1988], partly since no cratonic areas were located in the northern high latitudes. However, due to the absence of land masses in the Northern Hemisphere, the modelled meridional circulation is very weak thereby enhancing the isolation of the northern high latitudes from the equatorial source of heat. Consequently, results from all sensitivity experiments conducted in this study consistently reveal the presence of permanent sea ice cover extending from the pole to 60-70°N. A minimum end of boreal summer sea ice extent is achieved in the 18x_wfcs_aj01 experiment with a value of $12.3 \times 10^6 \text{ km}^2$ whereas a maximum is achieved in the 10x_wfcs_aj03 experiment with a value of $59.4 \times 10^6 \text{ km}^2$. For comparison, present-day Southern Ocean maximum sea ice area is $\sim 15 \times 10^6 \text{ km}^2$ [Hartmann, 1994].

Note that the thermodynamic sea ice model used in this study did not allow for the advection of sea ice by the surface winds and ocean currents and its deformation. The annually averaged sea ice thickness in the Northern Hemisphere is ~2-3 m.

4.2.5 Comparison of glacial response with other modelling experiments

Recent modelling experiments have partially succeeded in resolving the Late Ordovician glaciation – high CO₂ paradox [*Crowley and Baum, 1991; Crowley and Baum, 1995; Gibbs et al., 1995*]. In particular, *Crowley and Baum [1995]* needed to specify an elevated topography (500 m) and an 1.5x increased heat transport (relative to present-day) in order to obtain a significant permanent snow cover on Gondwana. The extent of their modelled snow cover was $12.9 \times 10^6 \text{ km}^2$, which is in the same range as the estimate derived from glacial deposits.

In the present study, the most extensive permanent snow cover was obtained using an intermediate orbital configuration (WFCS) and an albedo jump of 0.3. The extent of this permanent snow cover was $14.5 \times 10^6 \text{ km}^2$. In addition, a permanent sea ice cover bordered the southern high latitudes of Gondwana with an extent of $17.7 \times 10^6 \text{ km}^2$. These results no longer point to a unique setting ideal for glacial inception but rather, a range of several potential configurations.

4.2.6 Glacial chronology

The present thesis was an attempt to further our understanding of the equilibrium climate response to the significantly different boundary conditions of the Late Ordovician. The transient climate response to altered boundary conditions such as encountered through glacial inception and termination was beyond the scope of this thesis. In this section, I discuss several issues pertaining to the timing and chronology of the Late Ordovician glaciation based on glacial-interglacial patterns detected during the last 1 m.y.

The present, Late Cenozoic Glacial Age was initiated about 10 Ma [*Crowley and North, 1991*]. Since that time, the Pleistocene ice sheets have experienced several periods of growth and decay as the earth's climate has fluctuated between ice ages and interglacial ice ages. However, significant portions of the polar ice sheets have persisted through the warm, interglacial ages and are part of a permanent ice sheet, characteristic of a Glacial Age.

The driving mechanism responsible for these extended periods of recurrent continental glaciations is unclear but appears to be linked to continental drift. The leading theory argues that geologic periods which had a significant fraction of the earth's continents located in the vicinity of polar regions, coincided with the accumulation of unstable mass of ice in high latitudes [*Crowley and North, 1991*]. For example, the Cenozoic climate decline began ~55 Ma, and coincided with the ongoing breakup of Pangea and the detachment of Antarctica from Australia. Following this separation was a gradual southward shift of Antarctica (which is now centred on the South Pole). During the Ordovician Period, parts of the Gondwana supercontinent were located in high latitudes and this may have played a conditioning role for the setting of an unstable climate, susceptible to the onset of a glaciation.

An analysis of the time evolution of the three major orbital parameters during the last 1 m.y. provides valuable insights about their cumulative influence on the temporal variation of the solar insolation reaching the earth's surface. Figure 4.10 shows the variations of the obliquity, eccentricity, longitude of perihelion and of the precession parameter over the past 1 m.y. These time series are derived after the work of *Berger* [1978]. In addition, Figure 4.10 indicates the timing and chronology of the four orbital configurations investigated in the present study (CSO, HSO, WFCS, CFWS). In the past 1 m.y., there is evidence for at least seven major ice ages which apparently lasted for ~100 KY [*Crowley and North, 1991*]. The timing of these ice ages corresponds closely to the occurrences of the CSO configurations. It is also apparent from the figure that an HSO configuration can occur shortly after (~40 KY) a CSO configuration (ex. see at ~200 KY).

According to calculations conducted by *Berger* [1989], orbital periods may have been ~10-20% shorter in the Paleozoic. This suggests that glacial and interglacial ages might also have occurred on shorter timescales. Evidence derived from event stratigraphy done in Northwest Africa points to three or four major growth phases of the continental ice cap from the late Caradoc through the Ashgill [*Barnes*, 1986]. These pulses correlate well with the four regressive sequences observed in Anticosti Island, Québec [*Barnes et al.*, 1995]. It appears that the frequency and timing of these pulses may be linked to Milankovitch's theory of ice ages. However, as discussed in Section 1.5, dating glacial deposits is particularly difficult because they are generally devoid of fossils [*Flint*, 1971]. A better resolution of the stratigraphic record is still necessary in order to constrain the occurrence of glacial deposits within a narrower time frame.

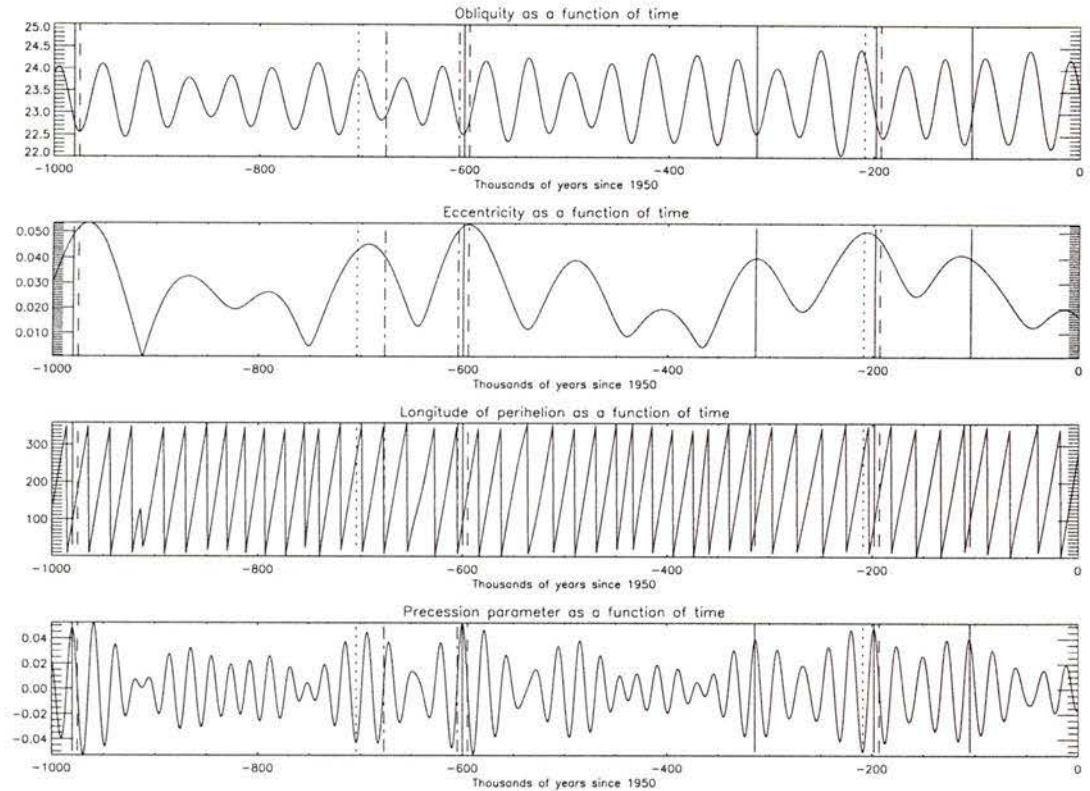


Figure 4.10 Variations of the obliquity, eccentricity, longitude of the perihelion and precession parameter over the past 1 m.y. Time series derived from *Berger* [1978]. The timing of the four orbital configurations investigated in the present study are shown as vertical lines: CSO (solid), HSO (dotted), WFCS (dashed-dot) and CFWS (dashed). The dominant periods are ~41 KY (obliquity), ~100 and ~400 KY (eccentricity), ~22 KY (longitude of perihelion) and ~19 and ~23 KY for precession parameter ($e \sin \lambda$).

The sensitivity experiments conducted in this thesis suggest that a permanent snow cover could be initiated during a WFCS orbital configuration and a high albedo jump or during a CSO configuration. The question remains whether a sufficiently large ice sheet initiated during these times could survive through an HSO configuration. If so, this would allow for the possibility of an extended glaciation of a few million years.

4.3 Future studies

4.3.1 Effects of changes in cloud cover

Cloud cover plays a critical role in the radiation balance and climate. The presence of clouds influences the albedo, absorptivity and transmissivity of the incoming solar radiation. The EMBM used for this study does not include a direct cloud parameterisation but roughly accounts for their presence by reducing the incoming solar radiation by 30% (this also includes the reflection and scattering done by water vapour, dust and ozone; Section 2.1.2.1).

Bishop et al. [1997] recently noted important differences between the Atlantic and the Pacific Oceans surface solar irradiance fields ($\sim 50 \text{ W/m}^2$ greater over the Atlantic at 45°N). They argued that the greater irradiance received by the Atlantic Ocean in the Northern Hemisphere during the month of July could be linked to an enhanced continental influence [*Bishop and Rossow*, 1991; *Bishop et al.*, 1997].

Given the unique continental configuration of the Ordovician Period, which was confined to the Southern Hemisphere, and the Panthalassic Ocean, which covered most of the Northern Hemisphere, it is almost certain that cloud cover was notably different from that of the present-day. One could conduct a set of sensitivity experiments with an altered planetary albedo in order to assess the potential climatic implications resulting from a changed distribution of cloud cover.

4.3.2 Effects of extensive equatorial epicontinental seas

Brass et al. [1982] suggested that changes in the size and configuration of marginal seas in net evaporation zones due to lithospheric plate motions and eustatic sea level change may have caused these areas to become sources of warm and saline bottom waters. As discussed in Section 1.4.5.2, the transition between a warm to a glaciated climate, such as the one observed during the Ordovician Period, could have induced an oceanic overturn of potentially toxic warm and saline bottom waters to the surface, inducing mass mortality.

Due to the lack of geological evidence, a flat-bottom topography was prescribed (constant depth of ~5 km) in all experiments conducted in this study. Future modelling studies could investigate the potential climatic influence of these epicontinental seas by artificially prescribing distinct equatorial regions with high salinities, such as the ones discussed in Section 4.1.2.

4.3.3 Effects of oceanic gateways

The closing and opening of oceanic gateways (or barriers) have resulted in important changes in paleocirculation and paleoclimate throughout the Phanerozoic. These gateways either allow or restrict the transport of heat from one region of the earth to another. As discussed in Section 1.2, the presence of several micro-continents in the middle of the Iapetus Ocean may have contributed in the redistribution of heat from equatorial to polar latitudes during the Ordovician Period [*Scotese and McKerrow*, 1990]. However, their precise identification, geometry and respective time of inception remain unclear. Additional paleogeographic research is required prior to the incorporation of these features into modelling experiments and is essential for describing past modes of oceanic circulation.

5. Conclusions

The analysis of the geological, chemical and paleontological records of the Ordovician System has unearthed an apparent paradox, which consists of the occurrence of the Late Ordovician glaciation centred on the South Pole, simultaneous with high atmospheric CO₂ concentrations (10 to 18x pil). The purpose of this thesis is to investigate this paradox through a series of modelling sensitivity experiments and to combine results with analytical data provided by the paleontological and geological records. Particular emphasis is given to questioning the ocean's influence in the Late Ordovician climate, through an analysis of poleward heat transport patterns.

The timing of the glacial maxima, during the Hirnantian Stage, coincides with the second greatest mass extinction event in all of the Phanerozoic. Given the paleontological evidence available thus far, the scenario that holds the glaciation as the unique cause for the mass extinction appears too simplistic. It seems that prior to the glaciation, the Ordovician biota was already undergoing considerable environmental pressures due to changes in sea level, ocean temperature and circulation. However, the climate change, which resulted from the growth and decay of the Gondwana ice sheets, may have provided a critical forcing for extinction. The determination of sea surface temperatures for the Ordovician based on $\delta^{18}\text{O}$ measurements is susceptible to diagenetic effects. Particularly for this reason, and also because $\delta^{18}\text{O}$ measurements only reflect local conditions, this approach has been under strict scrutiny [Veizer *et al.*, 1997b]. At this point in time, there exists a limited global coverage of high quality $\delta^{18}\text{O}$ data. Only when better-constrained paleotemperature estimates become available will the attempt to compare these estimates with modelling results be justified.

The duration of the glaciation remains an unresolved issue. While the age of glacial deposits spans ~30 m.y., oxygen and carbon isotopic data limited to the Ordovician-Silurian boundary interval have provided support for a short-lived glaciation [Brenchley *et al.*, 1995]. In the event that the glaciation was less than 1 m.y. (i.e. restricted to the Hirnantian; 0.5 m.y.) [Harland *et al.*, 1989], Berner's geochemical modelling estimates

for atmospheric CO₂ levels (8x – 20x pil) could not be applied to the glaciation as the model has a timestep of 10 m.y. [Berner, 1991; Berner, 1994]. In addition, the 16x pdl estimate of CO₂ based on the analysis of goethite may not coincide with the Late Ordovician glaciation [Yapp and Poths, 1992] (Section 1.8.1). Hence, the existence of the paradox investigated in this thesis is in itself debatable. If the glaciation was of short duration, CO₂ levels may have been low during that time. Based on the isotopic and eustatic evidence reviewed here, I choose to assume that the glaciation, although it may have peaked during the Hirnantian, was initiated during the late Caradoc and persisted through the Llandovery. Hence, even if CO₂ levels were indeed especially low for a short period of time simultaneous to the glacial maxima, the climatic conditions, which led to the glacial inception, may have included CO₂ concentrations 10 to 18x pil.

Results from the modelling experiments show that it is possible to maintain a significant permanent snow cover in the southern high latitudes of Gondwana given 10x CO₂ concentrations, WFCS forcing, -4.5% solar luminosity, a length of day of 21.5 hours and an albedo jump of 0.3. In addition, the CSO experiment with 10x CO₂, a decreased solar luminosity and shortened length of day and an albedo jump of 0.1 also sustained a permanent snow cover, although less extensive than for the WFCS experiment with the higher albedo. Further experiments with a CSO configuration and higher albedo jumps are needed in order to determine the lower boundary of the parameter space for which permanent snow cover corresponds to the estimated area of the Late Ordovician ice sheet.

It is apparent from the experiments that the low precipitation over the Gondwanan landmass is likely an underestimate, and may in fact, act to prevent the initiation of a continental glaciation. To bypass this problem, one could conduct a series of complementary experiments with a prescribed snow cover encompassing all glacial deposits and test whether the ice sheet could survive through an HSO. As previously argued by Crowley *et al.* [1987], summer temperatures may be a more critical parameter for glacial inception than the supply of moisture. Model results showed that whereas high latitude winter temperatures were always cold enough to ensure precipitation to fall as snow, summer temperatures were in some instances, such as for the HSO, warm

enough so as to prevent the development of a permanent snow cover. Perhaps sustained ice-albedo feedbacks concurrent with the existence of an ice sheet would be sufficient to inhibit the termination of the glaciation when orbital forcing would enter an HSO configuration.

Results from all sensitivity experiments consistently reveal the presence of a permanent sea ice cover extending from the North Pole to 60°-70°N. The presence of this extensive sea ice cover appears to have played a critical role in the dramatic cooling of the globally averaged ocean temperature.

The modelling experiments conducted in this study do not allow for the critical assessment of the ocean's role in the two phases of mass extinctions apparent at the end of the Ordovician Period. Results do show a shift in the location of the deep-water formation site in the Southern Hemisphere due to changes in CO₂ and albedo jump.

The climate obtained after varying CO₂ levels from 10x to 18x pil concentrations (with a decreased solar luminosity, a CFWS and an albedo jump of 0.1) reveals a strong thermal response of the coupled model. The global-mean SAT increased by ~2.74°C and ocean temperature by ~0.35°C between the 10x and 18x experiments. January snow cover does not survive for any of the CO₂ sensitivity experiments as the hot summer temperatures at the South Pole promotes a vigorous melt season. The hydrological cycle increases by 3.4% between the 10x and 18x experiments. The increase in precipitation with increased CO₂ levels is accentuated in polar regions and is associated with the contraction of the sea ice cover. The strength of the meridional overturning is not significantly affected by the increase in CO₂ but the location of the Southern Hemisphere deep-water formation site shifts poleward with the increase.

The coupled model reveals a strong sensitivity to changes in the albedo jump. The global-mean SAT and ocean temperature cooled by ~5.9°C and ~0.8°C respectively between the aj01 and aj03 experiments. The strength of the meridional overturning above 2,000 m decreases and the location of the Southern Hemisphere deep-water formation site shifts equatorward with the increased albedo jump. Concurrent to the

weakening of the thermohaline circulation is a decrease in the Southern Hemisphere heat transport with the increased albedo jump.

There are no significant changes in global-mean atmosphere and ocean temperatures between the two extreme orbital configurations. A marked increase in the intensity of the seasonal cycle is apparent in the HSO experiment relative to the CSO experiment, as one would expect from the influence of the higher obliquity. In addition, the CSO configuration has a slightly more vigorous meridional overturning. The annual average precipitation rates produced in the present study show a small increase at polar latitudes for the HSO relative to the CSO configuration. However, during the months where precipitation mostly falls as snow (June-July-August), high latitude precipitation is largest for the CSO scenario.

The geographic configuration of the Late Ordovician, which was drastically different than that of present-day, resulted in an up to ~42% increase in the global ocean poleward heat transport in the Southern Hemisphere, a latitudinal redistribution of the ocean heat transport and a significant asymmetry relative to the equator. These findings question the validity of the use of symmetric (about the equator) prescribed ocean heat transports in previous uncoupled atmosphere/mixed layer ocean modelling studies.

Modelled wind-driven and thermohaline circulation patterns are also strongly affected by the Ordovician continental configuration. The modelled wind-driven circulation closely corresponds to previous descriptions based on ocean-atmosphere dynamic principles and present-day analogues [Wilde, 1991].

As the aim of this study was to evaluate the potential for a Gondwanan glaciation given the set of boundary conditions revealed from the geologic record, the experiments were conducted separately and each integrated to equilibrium. An alternative approach would consist in conducting a series of perturbation experiments stemming from one control run in order to look at the ocean's transient response to certain critical climatic parameters such as a sudden drop or increase in CO₂. However, the turnover timescale of the ocean (~2000 years) remains much shorter than the estimated length of the glaciation

(minimum ~0.5 m.y.). Hence, this approach would also have its obvious limitations. Perhaps the future incorporation of the carbon cycle into general circulation models will allow for a closer look at the timing and duration of the glaciation.

In light of these restraints, the coupled model was able to produce a permanent snow cover on Gondwana, which included 60% of all the glacial deposits found on the supercontinent. Hence, within the context of the coupled model, no paradox exists.

References

- Algeo, T.J., and B.H. Wilkinson, Modern and ancient continental hypsometries, *Journal of the Geological Society*, 148, 643-653, 1991.
- Alvarez, L.W., W. Alvarez, F. Asaro, and H.V. Asaro, Extraterrestrial cause for the Cretaceous-Tertiary extinction: Experimental results and theoretical interpretations, *Science*, 208, 1095-1108, 1980.
- Armstrong, R.L., Glacial erosion and the variable isotopic composition of strontium in sea water, *Natural Physical Science*, 230, 132-133, 1971.
- Bahcall, J.N., Solar models, neutrino experiments, and helioseismology, *Reviews of Modern Physics*, 60 (2), 297-372, 1988.
- Bambach, R.K., C.R. Scotese, and A.M. Ziegler, Before Pangea: The geographies of the Paleozoic world, *American Scientist*, 68, 26-38, 1980.
- Barnes, C.R., The faunal extinction event near the Ordovician-Silurian boundary: A climatically induced crisis, in *Global Bio-Events*, edited by O. Walliser, pp. 121-126, Springer-Verlag, Berlin, 1986.
- Barnes, C.R., The proposed Cambrian-Ordovician global boundary stratotype and point (GSSP) in Western Newfoundland, Canada, *Geological Magazine*, 125, 381-414, 1988a.
- Barnes, C.R., Stratigraphy and palaeontology of the Ordovician-Silurian boundary interval, Anticosti Island, Québec, Canada, in *A global analysis of the Ordovician-Silurian boundary*, edited by L.R.M. Cocks, and R.B. Rickards, pp. 195-219, Bulletin of the British Museum (Natural History), London, 1988b.
- Barnes, C.R., The uppermost series of the Ordovician System, in *Global perspectives on Ordovician geology*, edited by B.D. Webby, and J.R. Laurie, pp. 185-192, Balkema, Rotterdam, 1992.
- Barnes, C.R., and S.M. Bergstrom, Conodont biostratigraphy of the Uppermost Ordovician and Lowermost Silurian, in *A global analysis of the Ordovician-Silurian boundary*, edited by L.R.M. Cocks, and R.B. Rickards, pp. 325-343, Bulletin of the British Museum (Natural History), London, 1988.
- Barnes, C.R., R.A. Fortey, and S.H. Williams, The pattern of global bio-events during the Ordovician Period, in *Global events and event stratigraphy in the Phanerozoic*, edited by O.H. Walliser, pp. 139-172, Springer-Verlag, New York, 1995.
- Benedetto, J.L., The first typical Hirnantia Fauna from South America (San Juan Province, Argentine Precordillera), in *Les brachiopodes fossiles et actuels*, edited by P.R. Racheboeuf, and C. Emig, pp. 439-447, Université de Bretagne Occidentale, Brest, 1986.

Berger, A., The spectral characteristics of Pre-Quaternary climatic records, an example of the relationship between the astronomical theory and geosciences, in *Climate and Geosciences*, edited by B. A., and et al., pp. 47-76, Kluwer Academic, 1989.

Berger, A.L., Obliquity and precession for the last 5,000,000 years, *Astronomy and Astrophysics*, 51, 127-135, 1976.

Berger, A.L., Long-term variation of caloric insolation resulting from the Earth's orbital elements, *Quaternary Research*, 9, 139-167, 1978.

Berger, A.L., M.F. Loutre, and V. Dehant, Influence of the changing lunar orbit on the astronomical frequencies of Pre-Quaternary insolation patterns, *Paleoceanography*, 4 (5), 555-564, 1989.

Berger, W.H., and H.R. Thierstein, Phanerozoic mass extinctions, *Naturwissenschaften*, 66 (1), 46-47, 1979.

Berner, R.A., Atmospheric carbon dioxide levels over Phanerozoic time, *Science*, 249, 1382-1386, 1990.

Berner, R.A., A model for atmospheric CO₂ over Phanerozoic time, *American Journal of Science*, 291, 339-376, 1991.

Berner, R.A., 3GEOCARB II: A revised model of atmospheric CO₂ over Phanerozoic time, *American Journal of Science*, 294, 56-91, 1994.

Berner, R.A., and A.C. Lasaga, Modeling the geochemical carbon cycle, *Scientific American*, 74-81, 1989.

Berry, W.B.N., and A.J. Boucot, Glacio-eustatic control of Late Ordovician-Early Silurian platform sedimentation and faunal changes, *Geological Society of America Bulletin*, 84, 275-284, 1973.

Berry, W.B.N., and P. Wilde, Graptolite biogeography: Implications for palaeogeography and palaeoceanography, in *Palaeozoic Palaeogeography and Biogeography*, edited by W.S. McKerrow, and C.R. Scotese, pp. 129-137, Geological Society, London, 1990.

Beuf, S., B. Biju-Duval, O. de Carpal, P. Rognon, O. Gariel, and A. Bennacef, Les grès du Paléozoïque inférieur au Sahara. Sédimentation et discontinuités, évolution structurale d'un craton, *Publications de l'Institut français du Pétrole Technip*, 18, 1-464, 1971.

Bishop, J.K.B., and W.B. Rossow, Spatial and temporal variability of global surface solar irradiance, *Journal of Geophysical Research*, 96 (C9), 16839-16858, 1991.

Bishop, J.K.B., W.B. Rossow, and E.G. Dutton, Surface solar irradiance from the International Satellite Cloud Climatology Project 1983-1991, *Journal of Geophysical Research*, 102 (D6), 6883-6910, 1997.

- Bolton, D., The computation of equivalent potential temperature, *Monthly Weather Review*, 108, 1046-1053, 1980.
- Bond, G.C., P.A. Nickeson, and M.A. Kominz, Breakup of a supercontinent between 625 Ma and 555 Ma: New evidence and implications for continental histories, *Earth and Planetary Science Letters*, 70, 325-45, 1984.
- Boucot, A.J., Phanerozoic extinctions: How similar are they to each other?, in *Extinction events in earth history*, edited by E.G. Kauffman, and O.H. Walliser, pp. 5-30, Springer-Verlag, New York, 1990.
- Boucot, A.J., C. Xu, and C.R. Scotese, Ibexian and Post-Ibexian paleogeography based on climatically sensitive sediments and biogeographic data, in *Ordovician Odyssey: Short papers for the seventh international symposium on the Ordovician system*, edited by J.D. Cooper, M.L. Droser, and S.C. Finney, pp. 291-295, The Pacific Section Society for Sedimentary Geology, Fullerton, 1995.
- Brass, G.W., J.R. Southam, and W.H. Peterson, Warm saline bottom water in the ancient ocean, *Nature*, 296, 620-623, 1982.
- Brenchley, P.J., Environmental changes close to the Ordovician-Silurian boundary, *Bulletin of British Museum (Natural History)*, 43, 377-385, 1988.
- Brenchley, P.J., The Late Ordovician extinction, in *Mass extinctions: Processes and evidence*, edited by S.K. Donovan, pp. 104-132, Belhaven Press, London, 1989.
- Brenchley, P.J., G.A.F. Carden, and J.D. Marshall, Environmental changes associated with the "first strike" of the Late Ordovician mass extinction, *Modern Geology*, 20, 69-82, 1995.
- Brenchley, P.J., and L.R.M. Cocks, Ecological associations in a regressive sequence: The latest Ordovician of the Oslo-Asker district, Norway, *Palaeontology*, 25 (4), 783-815, 1982.
- Brenchley, P.J., J.D. Marshall, G.A.F. Carden, D.B.R. Robertson, D.G.F. Long, T. Meidla, L. Hints, and T.F. Anderson, Bathymetric and isotopic evidence for a short-lived Late Ordovician glaciation in a greenhouse period, *Geology*, 22, 295-298, 1994.
- Brenchley, P.J., and G. Newall, A facies analysis of Upper Ordovician regressive sequences in the Oslo region, Norway - A record of glacio-eustatic changes, *Palaeogeography, Palaeoclimatology, Palaeoecology*, 31, 1-38, 1980.
- Brenchley, P.J., and G. Newall, Late Ordovician environmental changes and their effect on faunas, in *Aspects of the Ordovician System*, edited by D.L. Bruton, pp. 65-79, Paleontological Contributions from the University of Oslo, 1984.
- Brenchley, P.J., M. Romano, T.P. Young, and P. Storch, Hirnantian glaciomarine diamictites - Evidence for the spread of glaciation and its effect on Upper Ordovician

- faunas, in *Advances in Ordovician Geology*, edited by C.R. Barnes, and S.H. Williams, pp. 325-336, Geological Survey of Canada, Paper 90-9, 1991.
- Broccoli, A.J., and S. Manabe, The influence of continental ice, atmospheric CO₂, and land albedo on the climate of the last glacial maximum, *Climate Dynamics*, 1, 87-99, 1987.
- Bryan, K., A numerical method for the study of the circulation of the world ocean, *Journal of Computational Physics*, 4, 347-376, 1969.
- Budyko, M.I., The effect of solar radiation variations on the climate of the earth, *Tellus*, 21, 611-619, 1969.
- Caputo, M.V., Ordovician-Silurian glaciations and global sea-level changes, in *Silurian cycles: Linkages of dynamic stratigraphy with atmospheric, oceanic, and tectonic changes*, edited by E. Landing, and M.E. Johnson, pp. 15-26, New York State Education Department, New York, 1998.
- Caputo, M.V., and J.C. Crowell, Migration of glacial centers across Gondwana during Paleozoic Era, *Geological Society of America Bulletin*, 96, 1020-1036, 1985.
- Cawood, P.A., G.R. Dunning, D. Lux, and J.A.M. van Gool, Timing of peak metamorphism and deformation along the Appalachian margin of Laurentia in Newfoundland: Silurian, not Ordovician, *Geology*, 22, 399-402, 1994.
- Chatterton, B.D.E., and S.E. Speyer, Larval ecology, life history strategies, and patterns of extinction and survivorship among Ordovician trilobites, *Paleobiology*, 15 (2), 118-132, 1989.
- Cocks, L.R.M., Brachiopods across the Ordovician-Silurian boundary, in *A global synthesis of the Ordovician-Silurian boundary*, edited by L.R.M. Cocks, and R.B. Rickards, pp. 311-315, Bulletin of the British Museum (Natural History), London, 1988.
- Cocks, L.R.M., and R.A. Fortey, Biogeography of Ordovician and Silurian faunas, in *Palaeozoic Palaeogeography and Biogeography*, edited by W.S. McKerrow, and C.R. Scotese, pp. 97-104, Geological Society, London, 1990.
- Cooke, D.W., and J.D. Hays, Estimates of Antarctic Ocean seasonal sea-ice cover during glacial intervals, in *Antarctic Geoscience*, edited by C. Craddock, pp. 1017-1025, University of Wisconsin Press, Madison, 1982.
- Crowell, J.C., Gondwana glaciations, cyclotherms, continental positioning and climatic change, *American Journal of Science*, 278, 1345-1372, 1978.
- Crowley, T.J., Geological assessment of the greenhouse effect, *Bulletin of the American Meteorological Society*, 74, 2363-2373, 1993.

Crowley, T.J., and S.K. Baum, Toward reconciliation of Late Ordovician (~440 Ma) glaciation with very high CO₂ levels, *Journal of Geophysical Research*, 96 (D12), 22597-22610, 1991.

Crowley, T.J., and S.K. Baum, Reconciling Late Ordovician (440 Ma) glaciation with very high (14X) CO₂ levels, *Journal of Geophysical Research*, 100 (D1), 1093-1101, 1995.

Crowley, T.J., S.K. Baum, and K. Kim, General circulation model sensitivity experiments with pole-centered supercontinents, *Journal of Geophysical Research*, 98 (D5), 8793-8800, 1993a.

Crowley, T.J., J.G. Mengel, and D.A. Short, Gondwanaland's seasonal cycle, *Nature*, 329, 803-807, 1987.

Crowley, T.J., and G.R. North, *Paleoclimatology*, 339 pp., Oxford University Press, New York, 1991.

Crowley, T.J., K.J. Yip, and S.K. Baum, Milankovitch cycles and Carboniferous climate, *Geophysical Research Letters*, 20 (12), 1175-1178, 1993b.

Dalziel, I.W.D., L.H.D. Salda, and L.H. Gahajan, Paleozoic Laurentia-Gondwana interaction and the origin of the Appalachian-Andean mountain system, *Geological Society of America Bulletin*, 106, 243-252, 1994.

Denton, G.H., R.L. Armstrong, and M. Stuiver, The Late Cenozoic glacial history of Antarctica, in *The Late Cenozoic glacial ages*, edited by K.K. Turekians, pp. 267-306, Yale University Press, New Haven, 1971.

Destombes, J., and S. Willefert, The Ordovician-Silurian boundary in Morocco, in *A global synthesis of the Ordovician-Silurian boundary*, edited by L.R.M. Cocks, and R.B. Rickards, pp. 165-170, Bulletin of the British Museum (Natural History), London, 1988.

Endal, A.S., and S. Sofia, Rotation in solar-type stars. I. Evolutionary models for the spin-down of the sun, *The Astrophysical Journal*, 243, 625-640, 1981.

Fanning, A.F., and A.J. Weaver, An atmospheric energy-moisture balance model: Climatology, interpentadal climate change, and coupling to an ocean general circulation model, *Journal of Geophysical Research*, 101 (D10), 15111-15128, 1996.

Finney, S.C., and C. Xu, The relationship of Ordovician graptolite provincialism to palaeogeography, in *Palaeozoic Palaeogeography and Biogeography*, edited by W.S. McKerrow, and C.R. Scotese, pp. 123-128, Geological Society, London, 1990.

Fischer, A.G., Climatic oscillations in the biosphere, in *Biotic crises in ecological and evolutionary time*, edited by M.H. Nitecki, pp. 103-131, Academic Press, Chicago, 1981.

- Fischer, A.G., Long-term climatic oscillations recorded in stratigraphy, in *Climate in Earth History*, edited by W.H. Berger, and J.C. Crowell, pp. 97-104, National Academic Press, Washington, 1982.
- Fischer, A.G., Climatic rhythms recorded in strata, *Annual Review of Earth and Planetary Sciences*, 14, 351-376, 1986.
- Flint, R.F., *Glacial and quaternary geology*, 892 pp., John Wiley and Sons, New York, 1971.
- Fortey, R.A., Global earlier Ordovician transgressions and regressions and their biological implications, in *Aspects of the Ordovician System*, edited by D.L. Bruton, pp. 37-50, Oslo, 1984.
- Fortey, R.A., and L.R.M. Cocks, Marginal faunal belts and their structural implications, with examples from the Lower Palaeozoic, *Journal of the Geological Society of London*, 143, 151-160, 1986.
- Frakes, L.A., *Climates throughout geologic time*, 310 pp., Elsevier, New York, 1979.
- Frakes, L.A., J.E. Francis, and J.I. Sykkes, *Climate modes of the Phanerozoic*, 274 pp., Cambridge University Press, Cambridge, 1992.
- Gibbs, M.T., Glaciation, chemical weathering, and the carbon cycle, Doctor of Philosophy thesis, Pennsylvania State University, 1996.
- Gibbs, M.T., E.J. Barron, T.J. Crowley, and L.R. Kump, Model sensitivity of the Late Ordovician climate to atmospheric $p\text{CO}_2$, in *Ordovician Odyssey: Short papers for the seventh international symposium on the Ordovician system*, edited by M.L.D. J.D. Cooper, S.C. Finney, pp. 297-298, The Pacific Section Society for Sedimentary Geology, Fullerton, 1995.
- Goodfellow, W.D., G.S. Nowlan, A.D. McCracken, A.C. Lenz, and D.C. Gregoire, Geochemical anomalies near the Ordovician-Silurian boundary, Northern Yukon Territory, Canada, *Historical Biology*, 6, 1-23, 1992.
- Grahn, Y.G., and M.V. Caputo, Early Silurian glaciation in Brazil, *Palaeogeography, Palaeoclimatology, Palaeoecology*, 99, 9-15, 1992.
- Graves, C.E., W. Lee, and G.R. North, New parameterizations and sensitivities for simple climate models, *Journal of Geophysical Research*, 98 (D3), 5025-5036, 1993.
- Hambrey, M.J., The Late Ordovician-Early Silurian Glacial Period, *Palaeogeography, Palaeoclimatology, Palaeoecology*, 51, 273-289, 1985.
- Hambrey, M.J., and W.B. Harland, *Earth's Pre-Pleistocene glacial record*, 1004 pp., Cambridge University Press, Cambridge, 1981.

- Hardie, L.A., Secular variation in seawater chemistry: An explanation for the coupled secular variation in the mineralogies of marine limestones and potash evaporites over the past 600 m.y., *Geology*, 24 (3), 279-283, 1996.
- Harland, W.B., R.L. Armstrong, A.V. Cox, L.E. Craig, A.G. Smith, and D.G. Smith, *A revised geological time-scale*, Cambridge university press, Cambridge, 1989.
- Hartmann, D.L., *Global Physical Climatology*, 411 pp., Academic Press, San Diego, 1994.
- Hays, J.D., J. Imbrie, and N.J. Shackleton, Variations in the earth's orbit: pacemaker of the ice ages, *Science*, 194, 1121-1132, 1976.
- Hibler, W.D., A dynamic thermodynamic sea ice model, *Journal of Physical Oceanography*, 9, 815-846, 1979.
- Hibler, W.D., and G.M. Flato, Sea ice models, in *Climate system modeling*, edited by K.E. Trenberth, pp. 413-436, Cambridge University Press, Cambridge, 1992.
- Hoffman, P.F., Did the breakout of Laurentia turn Gondwanaland inside out?, *Science*, 252 (5011), 1409, 1991.
- Holmden, C., R.A. Creaser, K. Muehlenbachs, S.A. Leslie, and S.M. Bergström, Isotopic evidence for geochemical decoupling between ancient epeiric seas and bordering oceans: Implications for secular curves, *Geology*, 26 (6), 567-570, 1998.
- Holser, W.T., M. Magaritz, and R.L. Ripperdan, Global isotopic events, in *Global events and event stratigraphy in the Phanerozoic*, edited by O.H. Walliser, pp. 63-81, Springer-Verlag, New York, 1995.
- Hyde, W.T., K. Kim, and T.J. Crowley, On the relation between polar continentality and climate: Studies with a nonlinear seasonal energy balance model, *Journal of Geophysical Research*, 95 (D11), 18653-18668, 1990.
- Imbrie, J., and K.P. Imbrie, *Ice ages: Solving the mystery*, 224 pp., Harvard University Press, Cambridge, 1979.
- IPCC, *Climate change 1995: The science of climate change*, 572 pp., Cambridge University Press, Cambridge, 1996.
- Jenkins, G.S., H.G. Marshall, and W.R. Kuhn, Precambrian climate: The effects of land area and earth's rotation rate, *Journal of Geophysical Research*, 98, 8785-8791, 1993.
- Jeppsson, L., An oceanic model for lithological and faunal changes tested on the Silurian record, *Journal of the Geophysical Society London*, 147, 663-674, 1990.
- Johnson, M.E., L.R.M. Cocks, and P. Copper, Late Ordovician-Early Silurian fluctuations in sea level from eastern Anticosti Island, Québec, *Lethaia*, 81, 73-82, 1981.

- Kobluk, D.R., Coastal paleokarst near the Ordovician-Silurian boundary, Manitoulin Island, Ontario, *Bulletin of Canadian Petroleum Geology*, 32 (4), 398-407, 1984.
- Köppen, W., and A. Wegener, *Die klimare der geologischen vorzeit*, Gebrüder Borntraeger, Berlin, 1924.
- Koren, T.N., Evolutionary crisis of the Ashgill graptolites, in *Advances in Ordovician Geology*, edited by C.R. Barnes, and S.H. Williams, pp. 157-164, Geological Survey of Canada, Paper 90-9, 1991.
- Leggett, J.K., W.S. McKerrow, L.R.M. Cocks, and R.B. Rickards, Periodicity in the early Palaeozoic marine realm, *Journal of the Geological Society of London*, 138, 167-176, 1981.
- Legrand, P., Evidence and concerns with regard to the Late Ordovician glaciation in North Africa, in *Ordovician Odyssey: Short papers for the seventh international symposium on the Ordovician system*, edited by J.D. Cooper, M.L. Droser, and S.C. Finney, pp. 165-169, The Pacific Section Society for Sedimentary Geology, Fullerton, 1995.
- Levitus, S., and T.P. Boyer, *World Ocean Atlas 1994: Temperature*, 117 pp., Washington, 1994.
- Lewin, R., A thermal filter to extinction, *Science*, 223, 383-385, 1984.
- Long, D.G.F., Oxygen and carbon isotopes and event stratigraphy near the Ordovician-Silurian boundary, Anticosti Island, Québec, *Palaeogeography, Palaeoclimatology, Palaeoecology*, 104, 49-59, 1993.
- Lorenz, E.N., Forced and free variations of weather and climate, *Journal of Atmospheric Sciences*, 36, 1367-1376, 1979.
- Mac Niocaill, C., B.A. Van der Pluijm, and R. Van der Voo, Ordovician paleogeography and the evolution of the Iapetus ocean, *Geology*, 25 (2), 159-162, 1997.
- Marshall, J.D., and P.D. Middleton, Changes in marine isotopic composition and the late Ordovician glaciation, *Journal of the Geological Society, London*, 147, 1-4, 1990.
- McCracken, A.D., and C.R. Barnes, Conodont biostratigraphy and paleoecology of the Ellis Bay Formation, Anticosti Island, Québec, with special reference to Late Ordovician-Early Silurian chronostratigraphy of the systemic boundary: Part 2, *Geological Survey of Canada, Bulletin 329*, 51-134, 1981.
- McKerrow, W.S., Ordovician and Silurian changes in sea level, *Journal of the Geological Society London*, 136, 137-145, 1979.
- McKerrow, W.S., and C.R. Scotese, *Palaeozoic palaeogeography and biogeography*, 435 pp., London, 1990.

- McLaren, D.J., and W.D. Goodfellow, Geological and biological consequences of giant impacts, *Annual Review of Earth and Planetary Sciences*, 18, 123-171, 1990.
- Melchin, M.J., and C.E. Mitchell, Late Ordovician extinction in the Graptoloidea, in *Advances in Ordovician Geology*, edited by C.R. Barnes, S.H. Williams, pp. 143-156, Geological Survey of Canada, Paper 90-9, 1991.
- Middleton, P.D., J.D. Marshall, and P.J. Brenchley, Evidence for isotopic change associated with Late Ordovician glaciation, from brachiopods and marine cements of central Sweden, in *Advances in Ordovician Geology*, edited by C.R. Barnes, and S.H. Williams, pp. 313-323, Geological Survey of Canada, Paper 90-9, 1991.
- Milankovitch, M., *Astronomische Mittel zur Erforschung der erdgeschichtlichen Klimate*, *Handbuch der Geophysik*, 9, 593-698, 1938.
- Newman, M.J., and R.T. Rood, Implications of solar evolution for the earth's early atmosphere, *Science*, 198, 1035-1037, 1977.
- North, G.R., Theory of energy balance climate models, *Journal of Atmospheric Sciences*, 32, 2033-2043, 1975.
- North, G.R., J.G. Mengel, and D.A. Short, Simple energy balance model resolving the seasons and the continents: Application to the astronomical theory of the ice ages, *Journal of Geophysical Research*, 88, 6576-6586, 1983.
- Orth, C.J., J.S. Gilmore, L.R. Quintana, and P.M. Sheehan, Terminal Ordovician extinction: Geochemical analysis of the Ordovician/Silurian boundary, Anticosti Island, Québec, *Geology*, 14, 433-436, 1986.
- Owen, A.W., D.A.T. Harper, and R. Jia-yu, Hirnantian trilobites and brachiopods in space and time, in *Advances in Ordovician Geology*, edited by C.R. Barnes, and S.H. Williams, pp. 179-190, Geological Survey of Canada, Paper 90-9, 1991.
- Owen, A.W., and D.B.R. Robertson, Ecological changes during the End-Ordovician extinction, *Modern Geology*, 20, 21-39, 1995.
- Pacanowski, R., *MOM 2 Documentation user's guide and reference manual*, 232 pp., Princeton, 1995.
- Paris, F., Z. Elaouad-Debbaj, J.C. Jaglin, D. Massa, and L. Oulebsir, Chitinozoans and Late Ordovician glacial events on Gondwana, in *Ordovician Odyssey: Short papers for the 7th international symposium on the Ordovician system*, edited by J.D. Cooper, M.L. Droser, and S.L. Finney, pp. 171-176, Fullerton, 1995.
- Paterson, W.S.B., Laurentide ice sheets: Estimated volumes during late Wisconsin, *Review in Geophysics*, 10, 885-917, 1972.

- Peixoto, J.P., Water vapor balance of the atmosphere from 5 years of hemispheric data, *Nordic hydrology*, 2, 120-138, 1970.
- Petryk, A.A., Upper Ordovician glaciation: Effects of eustatic fluctuations on the Anticosti platform succession, Québec. Stratigraphy and paleontology, in *Field meeting, Anticosti, Gaspé, Québec*, edited by P.J. Lespérance, pp. 81-85, Montréal, 1981.
- Piper, J.D.A., *Paleomagnetism and the continental crust*, Open University Press: Milton Press, 1987.
- Qing, H., C.R. Barnes, D. Buhl, and J. Veizer, The Sr isotopic composition of Ordovician and Silurian brachiopods and conodonts: Relationships to geological events and implications for coeval seawater, *Geochimica et Cosmochimica Acta*, 62 (10), 1721-1733, 1998.
- Railsback, L.B., S.C. Ackerly, T.F. Anderson, and J.L. Cisne, Paleontological and isotope evidence for warm saline deep waters in Ordovician oceans, *Nature*, 343, 156-159, 1990.
- Ramanathan, V., The role of Earth radiation budget studies in climate and general circulation research, *Journal of Geophysical Research*, 92, 4075-4095, 1987.
- Ramanathan, V., L. Callis, R. Cess, J. Hansen, I. Isaksen, W. Kuhn, A. Lacis, F. Luther, J. Jahlman, R. Reck, and M. Schlesinger, Climate-chemical interactions and effects of changing atmospheric trace gases, *Review of Geophysics*, 25, 1441-1482, 1987.
- Raup, D.M., and J.J. Sepkoski, Mass extinctions in the marine fossil record, *Science*, 215, 1501-1503, 1982.
- Rong, J.Y., Distribution of the Hirnantia fauna and its meaning, in *Aspects of the Ordovician System*, edited by D.L. Bruton, pp. 101-112, Oslo, 1984.
- Rong, J.Y., and D.A.T. Harper, A global synthesis of the latest Ordovician Hirnantian brachiopod faunas, *Transactions of the Royal Society of Edinburgh: Earth Sciences*, 79, 383-402, 1988.
- Ronov, A., V. Khain, and K. Seslavinsky, *Atlas of lithological-paleogeographical maps of the world: Late Precambrian and Paleozoic of continents*, 70 pp., G. Kalionova, Leningrad, 1984.
- Ronov, A.B., V.Y. Khain, and A.N. Balukhovskiy, A comparative estimate of volcanism intensity on continents, *International Geology Review*, 22 (12), 1383-1389, 1980.
- Ross, J.R.P., and C.A. Ross, Ordovician sea-level fluctuations, in *Global perspectives on Ordovician geology*, edited by B.D. Webby, J.R. Laurie, pp. 327-335, Balkema, Rotterdam, 1992.
- Ruppel, S.C., E.W. James, J.E. Barrick, G.S. Nowlan, and T.T. Uyeno, High-resolution Silurian $^{87}\text{Sr}/^{86}\text{Sr}$ record: Evidence of eustatic control of seawater chemistry, in *Silurian*

- cycles: Linkages of dynamic stratigraphy with atmospheric, oceanic, and tectonic changes*, pp. 285-296, The New York State Education Department, New York, 1998.
- Scotese, C.R., *Paleogeographic Atlas*, PALEOMAP Project, Arlington, 1997.
- Scotese, C.R., R.K. Bambach, C. Barton, R. Van der Voo, and A.M. Ziegler, Paleozoic base maps, *Journal of Geology*, 87, 217-277, 1979.
- Scotese, C.R., and J. Golonka, *Paleogeographic Atlas*, University of Texas-Arlington, Arlington, 1992.
- Scotese, C.R., and W.S. McKerrow, Revised world maps and introduction, in *Palaeozoic Palaeogeography and Biogeography*, edited by W.S. McKerrow, and C.R. Scotese, pp. 1-21, Geological Society, London, 1990.
- Scotese, C.R., and W.S. McKerrow, Ordovician plate tectonic reconstructions, *Geological Survey of Canada*, 90 (9), 271-282, 1991.
- Scrutton, C.T., Periodic growth features in fossil organisms and the length of the day and the month, in *Tidal Friction and the Earth's Rotation*, edited by J.S. P. Brosche, pp. 154-196, Springer-Verlag, New York, 1978.
- Sellers, W.D., A global climatic model based on the energy balance of the Earth-atmosphere system, *Journal of Applied Meteorology*, 8, 392-400, 1969.
- Semtner, A.J., A model for the thermodynamic growth of sea ice in numerical investigations of climate, *Journal of Physical Oceanography*, 6, 379-389, 1976.
- Sepkoski, J., Jr., Patterns of Phanerozoic extinction: A perspective from global data bases, in *Global events and event stratigraphy in the Phanerozoic*, edited by O.H. Walliser, pp. 35-51, Springer-Verlag, New York, 1995a.
- Sepkoski, J.J., Jr., A factor analytic description of the Phanerozoic marine fossil record, *Paleobiology*, 7 (1), 36-53, 1981.
- Sepkoski, J.J., Jr., The Ordovician radiations: Diversification and extinction shown by global genus-level taxonomic data, in *Ordovician Odyssey: Short papers for the seventh international symposium on the Ordovician system*, edited by J.D. Cooper, M.L. Droser, and S.C. Finney, pp. 393-396, The Pacific Section Society for Sedimentary Geology, Fullerton, 1995b.
- Sheehan, P.M., Late Ordovician events and the terminal Ordovician extinction, in *Contributions to Paleozoic paleontology and stratigraphy in honor of Rousseau H. Flower*, pp. 405-415, New Mexico Bureau of Mines and Mineral Resources, 1988.
- Sheehan, P.M., and P.J. Coorough, Brachiopod zoogeography across the Ordovician-Silurian extinction event, in *Palaeozoic Palaeogeography and Biogeography*, edited by W.S. McKerrow, and C.R. Scotese, pp. 181-187, Geological Society, London, 1990.

- Sheehan, P.M., P.J. Coorough, and D.E. Fastovsky, Biotic selectivity during the K/T and Late Ordovician extinction events, in *The Cretaceous-Tertiary event and other catastrophes in earth history*, edited by G. Ryder, D. Fastovsky, and S. Gartner, pp. 477-489, Geological Society of America Special Paper 307, Boulder, 1996.
- Smith, A.G., A.M. Hurley, and J.C. Briden, *Phanerozoic paleocontinental world maps*, 102 pp., Cambridge University Press, New York, 1981.
- Sonett, C.P., S.A. Finney, and C.R. Williams, The lunar orbit in the late Precambrian and the Elatina sandstone laminae, *Nature*, 335, 806-808, 1988.
- Sonett, C.P., E.P. Kvale, A. Zakharian, M.A. Chan, and T.M. Demko, Late Proterozoic and Paleozoic tides, retreat of the moon, and rotation of the earth, *Science*, 273, 100-104, 1996.
- Spjeldnaes, N., Lower Palaeozoic palaeoclimatology, in *Lower Palaeozoic of the Middle East, Eastern and Southern Africa and Antarctica*, edited by C.H. Holland, pp. 199-256, Wiley, New York, 1981.
- Stanley, S.M., Temperature and biotic crises in the marine realm, *Geology*, 12, 205-208, 1984.
- Stanley, S.M., *Earth and Life through Time*, 690 pp., Freeman, W.H., New York, 1986.
- Sweet, W.C., *The Conodonta: Morphology, taxonomy, paleoecology and evolutionary history of a long extinct animal phylum*, 212 pp., Oxford University Press, 1988.
- Swisher, C.C., J.M. Grajales-Nishimura, A. Montanari, S.V. Margolis, P. Claeys, W. Alvarez, P. Renne, E. Cedillo-Pardo, F.J. Maurrasse, G.M. Curtis, J. Smit, and M.O. McWilliams, Coeval $^{40}\text{Ar}/^{39}\text{Ar}$ ages of 65.0 million years ago from Chicxulub crater melt rock and Cretaceous-Tertiary boundary tektites, *Science*, 257, 954-958, 1992.
- Thompson, S.J., and S.G. Warren, Parameterization of outgoing infrared radiation derived from detailed radiative calculations, *Journal of Atmospheric Sciences*, 39, 2667-2680, 1982.
- Thompson, S.L., and D. Pollard, A global climate model (GENESIS) with a Land-Surface Transfer Scheme (LSX). Part I: Present climate simulation, *Journal of Climate*, 8, 732-761, 1994.
- Tomczak, M., and J.S. Godfrey, *Regional oceanography: An introduction*, 422 pp., Pergamon, London, 1993.
- UNESCO, 10th report of the joint panel on oceanographic tables and standards, *UNESCO Technical Papers in Marine Sciences*, 36, 1981.
- UNESCO, Algorithms for computation of fundamental properties of seawater, *UNESCO Technical Papers in Marine Sciences*, 44, 1983.

- Vail, P.R., R.M. Mitchum, Jr., and S. Thompson, Seismic stratigraphy and global changes of sea level, Part 4: Global cycles of relative changes of sea level, in *Seismic stratigraphy: Application to hydrocarbon exploration*, pp. 83-97, American Association of Petrological Geology, Tulsa, 1977.
- Van Houten, F.B., Oolitic ironstones and contrasting Ordovician and Jurassic paleogeography, *Geology*, *13*, 722-724, 1985.
- Van Houten, F.B., and H. Hong-Fei, Stratigraphic and palaeogeographic distribution of Palaeozoic oolitic ironstones, in *Palaeozoic Palaeogeography and Biogeography*, edited by W.S. McKerrow, and C.R. Scotese, pp. 87-93, Geological Society, London, 1990.
- Vaslet, D., Upper Ordovician glacial deposits in Saudi Arabia, *Episodes*, *13*, 147-161, 1990.
- Veizer, J., D. Ala, K. Azmy, P. Bruckschen, D. Buhl, F. Bruhn, G.A.F. Carden, A. Diener, S. Ebneith, Y. Godderis, T. Jasper, C. Korte, F. Pawellek, O.G. Podlaha, and H. Strauss, $^{87}\text{SR}/^{86}\text{SR}$, $\delta^{18}\text{O}$ evolution of Phanerozoic seawater, *Chemical Geology*, in press.
- Veizer, J., D. Buhl, A. Diener, S. Ebneith, O.G. Podlaha, P. Burckschen, T. Jasper, C. Korte, M. Schaaf, D. Ala, and K. Azmy, Strontium isotope stratigraphy: Potential resolution and event correlation, *Palaeogeography, Palaeoclimatology, Palaeoecology*, *132*, 65-77, 1997a.
- Veizer, J., P. Burckschen, F. Pawellek, A. Diener, O.G. Podlaha, G.A.F. Carden, T. Jasper, C. Korte, H. Strauss, K. Azmy, and D. Ala, Oxygen isotope evolution of Phanerozoic seawater, *Palaeogeography, Palaeoclimatology, Palaeoecology*, *132*, 159-172, 1997b.
- Wang, K., B.D.E. Chatterton, M. Attrep, and C.J. Orth, Late Ordovician mass extinction in the Selwyn Basin, northwestern Canada: geochemical, sedimentological, and paleontological evidence, *Canadian Journal of Earth Sciences*, *30*, 1870-1880, 1993a.
- Wang, K., B.D.E. Chatterton, and Y. Wang, An organic carbon isotope record of Late Ordovician to Early Silurian marine sedimentary rocks, Yangtze Sea, South China: Implications for CO_2 changes during the Hirnantian glaciation, *Palaeogeography, Palaeoclimatology, Palaeoecology*, *132*, 147-158, 1997.
- Wang, K., C.J. Orth, J. M. Attrep, B.D.E. Chatterton, X. Wang, and J. Li, The great latest Ordovician extinction on the South China Plate: Chemostratigraphic studies of the Ordovician-Silurian boundary interval on the Yangtze platform, *Palaeogeography, Palaeoclimatology, Palaeoecology*, *104*, 61-79, 1993b.
- Weaver, A.J., M. Eby, A.F. Fanning, and E.C. Wiebe, Simulated influence of carbon dioxide, orbital forcing and ice sheets on the climate of the Last Glacial Maximum, *Nature*, *394*, 847-853, 1998.

- Weaver, A.J., and T.M.C. Hughes, On the incompatibility of ocean and atmosphere models and the need for flux adjustments, *Climate Dynamics*, 12, 141-170, 1996.
- Webby, B.D., Ordovician reefs and climate: A review, in *Aspects of the Ordovician system*, edited by D.L. Bruton, pp. 89-100, Paleontological contributions from the University of Oslo, Oslo, 1984.
- Wiebe, E.C., and A.J. Weaver, On the sensitivity of global warming experiments to the parameterisation of sub-grid scale ocean mixing, *Climate Dynamics*, in press.
- Wilde, P., Oceanography in the Ordovician, in *Advances in Ordovician Geology*, edited by C.R. Barnes, and S.H. Williams, pp. 283-298, Geological Survey of Canada, Paper 90-9, 1991.
- Wilde, P., and W.B.N. Berry, Destabilization of the oceanic density structure and its significance to marine "extinction" events, *Palaeogeography, Palaeoclimatology, Palaeoecology*, 48, 143-162, 1984.
- Wilde, P., W.B.N. Berry, and M.S. Quinby-Hunt, Silurian oceanic and atmospheric circulation and chemistry, *Special Papers in Palaeontology*, 44, 123-143, 1991.
- Wilde, P., W.B.N. Berry, M.S. Quinby-Hunt, C.J. Orth, L.R. Quintana, and J.S. Gilmore, Iridium abundances across the Ordovician-Silurian stratotype, *Science*, 233, 339-341, 1986.
- Williams, D.M., J. Harkin, and A.H.N. Rice, Umbers, ocean crust and the Irish Caledonides: terrane transpression and the morphology of the Laurentian margin, *Journal of the Geological Society of London*, 154, 829-838, 1997.
- Xu, C., Influence of the late Ordovician glaciation on basin configuration of the Yangtze Platform in China, *Lethaia*, 17, 51-59, 1984.
- Yapp, C.J., and H. Poths, Ancient atmospheric CO₂ pressures inferred from natural goethites, *Nature*, 355, 342-344, 1992.
- Young, G.M., Early Palaeozoic tillites of the northern Arabian Peninsula, in *Earth's pre-Pleistocene glacial record*, edited by M.J. Hambrey, and W.B. Harland, pp. 338-340, Cambridge University Press, Cambridge, 1981.
- Young, T.P., Ordovician sedimentary facies and faunas of Southwest Europe: Palaeogeographic and tectonic implications, in *Palaeozoic Palaeogeography and Biogeography*, edited by W.S. McKerrow, and C.R. Scotese, pp. 421-430, Geological Society, London, 1990.
- Zharkov, M.A., *History of Paleozoic salt accumulation*, 308 pp., Springer-Verlag, New York, 1981.

Ziegler, A.M., C.R. Scotese, W.S. McKerrow, M.E. Johnson, and R.K. Bambach, Paleozoic paleogeography, *Annual Review of Earth and Planetary Sciences*, 7, 473-502, 1979.

Zimmer, C., Location, location, location, *Discover* (December), 30-32, 1994.

Appendix A

Glossary

AC = Antarctica Current

AGCM = Atmosphere General Circulation Model

BP = Before Present

CSO = Cold Summer Orbit

CSWF = Cool Spring – Warm Fall orbit

EMBM = Energy Moisture Balance Model

GFDL = Geophysical Fluid Dynamics Laboratory

GENESIS = Global Environmental and Ecological Simulation of Interactive Systems

HSO = Hot Summer Orbit

IC = Iapetus Current

ITCZ = Inter-Tropical Convergence Zone

KY = Thousands of years

LOD = Length of Day (hours)

Ma = Million years ago (refers to the specific timing of an event)

MOM= Modular Ocean Model

m.y. = Million years (refers to duration of an event)

NEC = North Equatorial Current

NSPC = North Sub-Polar Current

OGCM = Ocean General Circulation Model

pil = Pre-industrial CO₂ levels

pdl = Present-day CO₂ levels

ppm = parts per million

psu = practical salinity unit

SEC = South Equatorial Current

WFCS = Warm Fall – Cool Spring orbit

VITA

Surname: Poussart

Given Names: Pascale Francine

Place of Birth: Québec, Québec, Canada

Educational Institutions Attended:

University of Victoria

1996 to 1998

McGill University

1993 to 1996

Degrees Awarded:

B.Sc. (with distinction)

McGill University

1996

Honours and Awards:

FCAR Scholarship

1996 to 1998

PARTIAL COPYRIGHT LICENSE

I hereby grant the right to lend my thesis to users of the University of Victoria Library, and to make single copies only for such users or in response to a request from the Library of any other university, or similar institution, on its behalf or for one of its users. I further agree that permission for extensive copying of this thesis for scholarly purposes may be granted by me or a member of the University designated by me. It is understood that copying or publication of this thesis for financial gain shall not be allowed without my written permission.

Late Ordovician Glaciation: Modelling Experiments of a Paradox

Author



Pascale Francine Poussart

December 15, 1998